



UNICAMP

UNIVERSIDADE ESTADUAL DE CAMPINAS  
Instituto de Física Gleb Wataghin

JOEL ANDERSON FERREIRA PINHEIRO

**Sondando Perovskitas de Haleto de Metal com Espectroscopia de  
Fotoelétrons por Microjato utilizando Raios X**

**Probing Metal-Halide Perovskites with X-ray Microjet Photo-electron  
Spectroscopy**

CAMPINAS

2023

JOEL ANDERSON FERREIRA PINHEIRO

**Probing Metal-Halide Perovskites with X-ray Microjet Photo-electron Spectroscopy**

**Sondando Perovskitas de Haleto de Metal com Espectroscopia de Fotoelétrons por Microjato utilizando Raios X**

Tese apresentada ao Instituto de Física Gleb Wataghin da Universidade Estadual de Campinas como parte dos requisitos exigidos para a obtenção do título de Doutor em Ciências, na Área de Física Aplicada.

Thesis presented to the Instituto de Física Gleb Wataghin of the Universidade Estadual de Campinas in partial fulfillment of the requirements for the degree of Doctor in science, in the area of Applied Physics.

Supervisor: ARNALDO NAVES DE BRITO

ESTE TRABALHO CORRESPONDE À VERSÃO FINAL DA TESE DEFENDIDA PELO ALUNO JOEL ANDERSON FERREIRA PINHEIRO E ORIENTADA PELO PROF. DR. ARNALDO NAVES DE BRITO.

CAMPINAS

2023

Ficha catalográfica  
Universidade Estadual de Campinas  
Biblioteca do Instituto de Física Gleb Wataghin  
Lucimeire de Oliveira Silva da Rocha - CRB 8/9174

P655p Pinheiro, Joel Anderson Ferreira, 1993-  
Probing metal-halide perovskite with X-ray microjet photo-electron spectroscopy / Joel Anderson Ferreira Pinheiro. – Campinas, SP : [s.n.], 2023.

Orientador: Arnaldo Naves de Brito.  
Tese (doutorado) – Universidade Estadual de Campinas, Instituto de Física Gleb Wataghin.

1. Perovskita. 2. Espectroscopia de raio X. 3. Nanomateriais. 4. Nanocristais. I. Brito, Arnaldo Naves de, 1962-. II. Universidade Estadual de Campinas. Instituto de Física Gleb Wataghin. III. Título.

Informações Complementares

**Título em outro idioma:** Sondando perovskitas de haleto de metal com espectroscopia de fotoelétrons por microjato utilizando raio X

**Palavras-chave em inglês:**

Perovskite

X-ray spectroscopy

Nanomaterials

Nanocrystals

**Área de concentração:** Física Aplicada

**Titulação:** Doutor em Ciências

**Banca examinadora:**

Arnaldo Naves de Brito [Orientador]

Túlio Costa Rizuti da Rocha

Rogério Magalhães Paniago

Abner de Siervo

Antônio Carlos Fontes dos Santos

**Data de defesa:** 18-12-2023

**Programa de Pós-Graduação:** Física

**Identificação e informações acadêmicas do(a) aluno(a)**

- ORCID do autor: <https://orcid.org/0000-0001-9762-0692>

- Currículo Lattes do autor: <http://lattes.cnpq.br/6129479015240361>



INSTITUTO DE FÍSICA  
GLEB WATAGHIN

MEMBROS DA COMISSÃO EXAMINADORA DA DISSERTAÇÃO DE DOUTORADO DO ALUNO JOEL ANDERSON FERREIRA PINHEIRO - RA 262756 APRESENTADA E APROVADA AO INSTITUTO DE FÍSICA GLEB WATAGHIN, DA UNIVERSIDADE ESTADUAL DE CAMPINAS, EM 18/12/2023.

COMISSÃO JULGADORA:

- Prof. Dr. Arnaldo Naves de Brito – Presidente e orientador (IFGW/UNICAMP)
- Prof. Dr. Tulio Costa Rizuti da Rocha (Centro Nacional de Pesquisa em Energia e Materiais/Laboratório Nacional de Luz Síncrotron)
- Prof. Dr. Rogério Magalhães Paniago (Departamento de Física da Universidade Federal de Minas Gerais)
- Prof. Dr. Abner de Siervo (IFGW/ UNICAMP)
- Prof. Dr. Antônio Carlos Fontes dos Santos (Instituto de Física da Universidade Federal do Rio de Janeiro)

**OBS.:** Ata da defesa com as respectivas assinaturas dos membros encontra-se no SIGA/Sistema de Fluxo de Dissertação/Tese e na Secretaria do Programa da Unidade.

CAMPINAS

2023

## ACKNOWLEDGMENTS

I am immensely grateful to my family for their unwavering support throughout my journey. My mother, Ana, has always shown me, unconditional love, while my father's, João, encouraging words have kept me motivated. My sister, Jordânia, has been my trusted friend, providing unwavering support. A special thanks to Kayman, who has been a friend accompanying me since my undergraduate studies, with whom I have shared joys, sorrows, and dreams throughout my academic journey. I would also like to mention some more recent but equally important friendships from the PhD pathway who have been my advisors and the reason for funny moments during tough times: Paulo Henrique, Jamile Feitosa, Mariano Chaves, Andreas, Vitor Sena, Barbara Peluzo, Murilo, Bruno Felipe, Pedro Dedinho. Finally, a special gratitude to my dedicated supervisor, Arnaldo, who guided me in taking significant steps in my career and life. Also, I want to express my gratefulness to Olle Bjornholm for welcoming me to Sweden and hosting me during my first international experience. I want to say thanks to the institution that funded my Ph.D. This study was financed in part by the Coordenação de Aperfeiçoamento de Pessoal de Nível Superior - Brasil (CAPES) - Finance Code 001 and Funcamp by "convênio nº 5333.3 Rubrica: 1700 Item: 7. I want to acknowledge the São Paulo State Foundation - FAPESP, processes numbers 2020/04822-9, 2021/06893- 3, 2021/06893-3 and 2017/11986- 5 as well as the computing resources and assistance of the John David Rogers Computing Center (CCJDR) in the Institute of Physics Gleb Wataghin, University of Campinas. I also acknowledge MAX IV Laboratory for time on the beamline FlexPES under Proposal 20190817. Research conducted at MAX IV, a Swedish national user facility, is supported by the Swedish Research Council under contract 2018-07152, the Swedish Governmental Agency for Innovation Systems under contract 2018-04969, and Formas under contract 2019-02496. I am also grateful to LNNano/CNPEM for the use of the TEM FEG facility. And yet, I also acknowledge the other support from Shell and the strategic importance of the support given by ANP (Brazil's National Oil, Natural Gas, and Biofuels Agency) through the R and D levy regulation. Likewise, I would like to acknowledge FAEPEX-UNICAMP for funding me during my PhD final months with the "Auxilio Ponte" request Number: 2014/24 as well as funding my participation in beamtime experiments at French synchrotron facility Solei as well as my visit to the Angstrom X-ray physics group at Uppsala University.

*We are like butterflies who flutter for a day and think it is forever[...] For small creatures such as us, the vastness is bearable only through love.*

*(Carl Sagan)*

# RESUMO

Nanocristais (NCs) de Perovskitas de Halogeneto Metálico (PHM),  $\text{PbCsX}_3$  ( $X = \text{Br}, \text{Cl}, \text{I}$ ), são fundamentais para a próxima geração de células fotovoltaicas de baixo custo. No entanto, a estabilidade de longo prazo dessas Perovskitas nos dispositivos é crucial para sua adoção generalizada. A compreensão da superfície dos NCs de PHM a nível atômico é essencial para melhorar sua estabilidade. A espectroscopia eletrônica de raios-X (XPS) é considerada o melhor método para estudar interfaces devido a ser elemento específico e sensível a interface. No entanto, estudos anteriores usando XPS em amostras sólidas foram comprometidos por fatores como carregamento, dano por radiação e, conseqüentemente, falta de informação sobre a distribuição do sinal de fotoelétrons em diferentes profundidades dos NCs.

Para abordar essas limitações, investigamos NCs de  $\text{PbCsBr}_3$  preparados por dois métodos de síntese: um com Oleamina, resultando em baixa estabilidade coloidal (OLA), e outro com ácido oleico, produzindo NCs mais estáveis (Método livre de amina, LA). Inicialmente, examinamos as amostras usando o método convencional, revestindo uma superfície condutora com a solução coloidal dos NCs de PHM e analisando o sinal de XPS dos níveis de  $\text{Pb } 4f$  e  $\text{Br } 3d$ . No entanto, encontramos danos por radiação em segundos, especialmente nas amostras LA. Portanto, introduzimos um novo método de sondagem das NCs de PHM usando XPS com microjato líquido em um síncrotron, reduzindo a dose de radiação na amostra em cerca de um milhão de vezes em relação ao método de estado sólido.

Usando esse novo método, determinamos a fração de fotoelétrons originários da superfície e das camadas subjacentes e correlacionamos os resultados experimentais de XPS com cálculos de Dinâmica Molecular (DM). Desenvolvemos novas fórmulas para determinar precisamente a quantidade de substituição atômica na superfície dos NCs a partir dos novos dados de XPS nas amostras líquidas. Determinamos que até  $65 \pm 5\%$  dos átomos de Cs na superfície foram substituídos nas PHM feitas com o método OLA, por outro lado não houve substituição de Br na superfície em ambos os métodos de síntese. Nosso resultados indicam que não há substituição atômica nas amostras LA. Essa substituição de Cs na superfície é um fator crucial para a estabilidade das NCs de PHM.

Além disso, registramos espectros de valência de  $\text{CsPbBr}_3$  e  $\text{CsPbI}_3$  em um microjato líquido, fornecendo valores de energia para os orbitais de valência ocupados e comparando os resultados com simulações.

# ABSTRACT

Metal-halide Perovskites (MHP) nanocrystals (NCs),  $\text{PbCsX}_3$  ( $X = \text{Br, Cl, I}$ ), is considered a promising core element for the next generation of low-cost photovoltaic solar cells. However, their long-term stability needs to be improved for commercial adoption. A better atomic-scale understanding of the MHP NC surface is crucial to improving this property. X-ray photoelectron spectroscopy (XPS) provides the best information about this interface since it is element and interface-specific. Unfortunately, previous results from solid-state have been compromised due to charging, radiation damage, contamination, and lack of information about the photoelectron signal's probing depth.

To address these issues, we studied  $\text{PbCsBr}_3$  MHP NCs prepared by two synthesis methods: one involving Oleylamine, resulting in poor colloidal stability (OLA), and the other using Acid Oleic, yielding more stable NCs (AF). Initially, the samples were examined using the method employed in the literature. However, the XPS signal revealed radiation damage induced within seconds on both samples, posing significant limitations to the technique's effectiveness. To prevent the limitations of the solid-state approach, we introduced a novel method — probing MHP NCs via XPS on a liquid micro-jet at a synchrotron. This method reduced radiation dose approximately a million times, and continuous sample replacement minimized contamination concerns. Using this new insertion method, we determined the amount of photoelectrons originating from the surface and underlying layers based on their kinetic energy.

The new core-level study revealed that NCs exhibit all six facets of CsBr terminations, and the synthesis method can influence this atomic surface structure. The elemental ratios Pb/Cs and Br/Cs, derived from XPS measurements along with Molecular Dynamics (MD) calculations, contributed to creating a model of the more stable Perovskite NCs. We also developed a novel formula to quantify surface atom substitution based on the experimental elemental ratios. Data analysis indicated that up to  $65 \pm 5\%$  of Cs, surface atoms were substituted in the OLA<sup>+</sup> method, with no surface Br substitution in either synthesis method. Our results show no surface Cs substitution in the amine-free method. We conclude that Cs substitution is a crucial factor in the stability of MHP NCs.

Previous and current results on solid samples align with radiation-induced oxidation on Br atoms, prompting scrutiny of result accuracy. Additionally, we recorded valence spectra of  $\text{CsPbBr}_3$  and  $\text{CsPbI}_3$  NCs in a liquid micro-jet, reporting energy values for the highest occupied orbitals and comparing the results with simulations.

# LIST OF FIGURES

2.1	In an Undulator, the short oscillations produce sharp peaks. The wiggler acts like a combination of several bending magnets; the spectra distribution is similar to the bending magnet but differs in the overall intensity. The Undulator differs from the two later in that the Undulator shows off narrow spectra distribution due to the overlapping and interference. . . . .	22
2.2	Above, we have the four parameters defining a beam's emittance x and y. The brilliance is inversely proportional to both the source size and the x-ray beam divergence . . . . .	23
2.3	Radiation coherence refers to wave properties' statistical similarity and correlation. Above, one can see an incoherent signal turning into a temporal and spatial coherent. Temporal coherence relates to time correlation along the wavefront propagation, and spatial coherence reflects correlation in transverse spatial points. Temporal coherence determines monochromaticity, while spatial coherence indicates wavefront phase uniformity. . . . .	24
2.4	Diagram of Matter and Radiation interaction where an initial radiation beam (it may be electrons, photons, neutrons, ions) hits the matter, resulting in additional or secondary radiation (Photoelectric Effects, Scattering Fluorescence Emission). The radiation can either not cause any change or alter the material structure (bulk, surface). . . . .	25
2.5	A electromagnetic spectrum diagram showing the non-ionizing and ionizing regions. The energy and frequency increase from the right to the left. The lowest frequency, radio waves, are transparent to the human body. Microwaves induce molecular rotation and torsion, while infrared induces molecular vibration. The visible light produces electron excitation to upper quantum levels. Ultraviolet light contains enough energy to ionize its target. X-rays hold enough energy to eject core electrons or scatter them. Besides the photoelectric effect and scattering, gamma rays can generate pair production. . . . .	26
2.6	An overview of Characterization Techniques utilized in scientific research and analysis branches. Each technique offers unique capabilities for investigating the properties and structures of materials, enabling in-depth analysis and understanding of various scientific phenomena." . . . . .	27

2.7	X-ray Photoelectron Spectroscopy (XPS) consists of ionizing the sample with a photon beam of energy $h\nu$ . The process involves a photon-in electron-out scheme, which generates typical spectra. A nozzle or capillary system generates a liquid jet for nano-crystal analysis in colloidal dispersion. Gas-phase samples or aerosol particles require an inert carrier gas aerosol beam that suspends the crystals. A sample holder or stage is utilized for solid samples, where the sample is typically a thin film (the blue part on the surface) with a solid substrate as a reference, such as a metal (the bottom part in red). [1] . . . . .	28
2.8	XPS Photoemission Peaks: 1s orbitals of C, O, and N elements. Notice how distinct peaks emerge from the same orbital, enabling precise elemental identification in the samples. . . . .	29
2.9	The figure shows a Python simulation of the core level and its satellite peaks. The O 1s core level is positioned at 534 eV. A valence electron is promoted to a higher energy state upon photoionization, resulting in two peaks between 540 and 550 eV for high binding energies. This interaction causes the energy in the core electron to reduce, leading to a satellite structure positioned a few eV below the core level on the kinetic energy (KE) scale. The Shake-off satellite effect is observed with its maximum at 550 eV and shows a tail that exponentially decays. This effect involves the complete ejection of a valence electron from the ion into the continuum, broadening the core level peak observed in XPS spectra or contributing to the inelastic background due to the wider range of energies associated with valence electrons compared to core electrons. . . .	30
2.10	The oxidation state of carbon affects the C1s binding energy in XPS. As oxidation increases, the C1s peak shifts to higher binding energies where on the x-axis is the element bound to C and on the y-axis is the value for the respective binding energy. Chemical bonds with hydrogen, nitrogen, or chlorine induce higher binding energy than Carbon alone (in response to the increasing electronegativity: Cl > N > H). Oxidation increases the electron density of carbon, resulting in higher binding energies. . . . .	31
2.11	Above, one sees the depiction of Spin-orbit splitting and electron transitions in photoelectron spectra for Mg 2p transitions generated in Python, including noises in the signal features. The binding energies of 2p <sub>1/2</sub> and 2p <sub>3/2</sub> in Mg are nearly identical, 49.6 eV and 49.2 eV), respectively. The energy separation between adjacent peaks within the same orbit increases with atomic number and decreases for higher l values within the same n. . . . .	33

2.12	The curve above was plotted in Python, which illustrates the relationship between electron kinetic energy and the inelastic mean free path (IMFP) in condensed matter (Adapted from [2] where a fitting was produced based on [3]). The curve is described by the equation $\Lambda_e = 1450/(\varepsilon_e^2) + 0.54\sqrt{\varepsilon_e}$ , where $\Lambda_e$ represents the IMFP in angstrom units and $\varepsilon_e$ represents the electron kinetic energy in electron volts (eV). The graph shows a logarithmic scale on both the x-axis (ranging from 0.1 to 10,000 eV) and the y-axis (ranging from 0.1 to 1000 Å).	34
3.1	The spectra for Cs and Br ionized by a 1253 V photon beam. On the top, one can see the Cs 4d (from 82 to 90 eV ) and Br 3d (from 76 to 81 eV ). The Cs 4d (from 76 to 83.5 eV ) and Br 3d (from 67 to 74 eV ) are seen on the bottom. For both NCs, it is possible to identify oxidated Br species in pale blue). The experimental data is in pink circles, and the fitted curve containing all the Cs and Br feature contributions is in black. . . . .	38
3.2	In both Nc synthesis methods, Pb oxidation is observed. A normalization procedure was implemented, and we obtained a signal difference of 0.8 between the red and black curves. In the Pb region, the degradation of OLA over time was registered in the black curve at the bottom, indicating no oxidation, and 17 minutes later, recorded from the same spot, a shoulder was present related to a Pb-oxidated state. . . . .	40
3.3	A normalization through the area under both curves was employed, and we found a signal difference of 0.86 between dark blue and light blue curves. It is demonstrated that oxidation of Pb in the AF Ncs has a distinguished behavior from the OLA case. Two Pb species are visible - one at a lower binding energy (Pb I) and another at a higher binding energy (Pb II), which is smaller due to an oxidized state. After 10 minutes, the oxidized species increases in size and becomes more prominent than the first species, leading to an inversion of proportion between the two species over time. Additionally, the late picture may depict the emergence of a third species with another oxidation state, Pb III. . .	41
3.4	We present the Pb/Cs and Br/Cs ratios for two different methods of synthesizing MHPs. These ratios are shown as a function of Photon Energy and are corrected by the photonionization cross-section. The results are displayed in two plots, with green-filled circles representing the OLA method on the left and blue-filled lozenge dots representing the AF method on the right. The red lines show the Pb/Cs ratios, while the black lines depict the Br/Cs ratios. The yellow dotted line represents the Br/Cs trend in the Ravi et al. study. The change in the ratio from around 5 to 3 indicates the expected composition of NCs from surface to bulk due to the photoelectron mean free path as a function of its excitation energy. The purplish dashed lines (3 for Br/Cs and 1 for Pb/Cs) represent the expected values for bulk. . . . .	42

4.1	a) Studies have observed that the absorption coefficients of Quantum Dots (QDs) obey a power law. This is because as the size of the QD decreases, there is a higher degree of quantum confinement, which produces an exciton of higher energy. As a result, the band gap energy increases. By using models and spectroscopic measurements of the emitted photon energy, it is possible to measure the band gap of QDs. b) Due to quantum confinement, QDs have discrete "atomic-like" states in the conduction and valence regions compared to semiconductors of macroscopic sizes. This confinement occurs when the size of the nanoparticle is smaller than the exciton Bohr radius, which is led by the size shrinking that collapses the bulk material's continuous energy bands into discrete ones. . . . .	45
4.2	A depiction of the XPS technique applied at the liquid-solid interface. A well-tuned X-ray beam ( $h\nu$ ) interacts with the nanocrystal surface immersed in a solvent mixture, emitting photoelectrons. The analyzer then captures these emitted electrons, providing valuable information about the chemical environment surrounding the nanocrystal. . . . .	47
4.3	The cMJPES setup description follows from the bottom-left to up-right. The solution the colloidal-phased MPH NCs are inserted through an HPLC pump straight into the vacuum chamber, where a cylindrical nozzle with a 15-25 $\nu$ m opening pushes the sample to form a jet. First, this micro-jet comes across with the X-ray beam. Second, the micro-jet strikes the liquid nitrogen trap, which condenses the vapor as well as the liquid, avoiding contamination getting into the pumps. After passing through the differential pumping nozzle, the photo-electrons are spatially separated according to their Kinetic Energy. . . . .	49
4.4	The calibrated spectra of Perovskite core level using the process described in Appendix A.1. In the first two spectra, the experimental data of Pb 4f electron peaks (split due to spin-orbit coupling) are depicted with red dots. The upper spectrum corresponds to the Amine-Free (AF) case, and the second spectrum represents the Oleylamine-capped (OLA <sup>+</sup> ) case, with the binding energy axis placed at the top. The last two spectra display the Cs 4d (on the left) and Br 3d (on the right) electron peaks, once more for the Amine-Free sample, shown as green dots, with the binding energy axis at the bottom. . . . .	51

4.5	The spectra are normalized according to the Pb 4f <sub>7/2</sub> peak, and the error bars were obtained from the process described in Appendix A.2. In b) the Br 3d peaks show no change in the intensity between the two methods. This constancy agrees with what is observed for the Pb 4f peaks in a). In contrast, the Cs 4d peak is substantially reduced in the OLA <sup>+</sup> synthesis spectrum. We propose the substitution of Cs atoms by OLA <sup>+</sup> as a mechanism for the OLA <sup>+</sup> bonding to the NCs. The NCs are diluted in toluene + hexane 1:1 volume. 5% per weight. d) Br/Cs (black) and Pb/Cs (red) ratios for both amine-free (blue points - indicate results from this work) and OLA <sup>+</sup> samples (green points - indicate results from this work), with photon energy 600 eV. The measurements linked by the continuous lines (without error bars) were reported by Ravi <i>et al</i> [4]. . . . .	53
4.6	Visible-Ultra-violet absorption spectra, the sample size influences intensity and shape. As seen in the spectra above, thick samples deliver absorption spectra in the visible-ultraviolet range, tending to have well-defined peaks corresponding to electronic transitions. However, in thin samples, such as thin films or nanoplates, quantum confinement effects can cause the absorption bands to broaden and shift to higher energy (shorter wavelength). This shift is due to the limited number of available energy states and the confinement of charge carriers within the reduced dimensions of the thin sample. . . . .	55
4.7	Transmission electron microscopy (TEM) images illustrating the morphology and size distribution of the CsPbBr <sub>3</sub> nanocubes in the AF and OLA samples. (a) The nanocube morphology with an average size of 12.0 ± 3.5 nm is observed for AF (b) The nanocube, along with nanoplate morphology, where these nanoplates were found to be monolayers (ML). . . . .	56
4.8	Lateral size distribution for the AF CsPbBr <sub>3</sub> NCs, a histogram showing an average size distribution of 12.0 ± 3.5 nm, with intervals of 1 nm ranging from 4 to 28 nm. In addition, the thickness distribution for the OLA-capped CsPbBr <sub>3</sub> NC nanoplates was found centered in 6 monolayers corresponding to a 3.54 nm. . . . .	58
4.9	X-ray Diffraction spectra of AF and OLA-capped CsPbBr <sub>3</sub> PNCs. . . . .	59
4.10	a. Unit cell of the orthorhombic phase of the CsPbBr <sub>3</sub> Perovskites. The atoms are Cs (green), Pb (gray), and Br (brown). The optimized tilting angles of the Pb-Br octahedra and the [001] interlayer distance are indicated. b. Scheme of all CsBr and PbBr <sub>2</sub> terminations considered. c. TEM image of an NC, obtained within the Amine-free method. d. NC model. . . . .	60
5.1	The green spectrum shows the toluene gas phase, while the red spectrum shows the toluene plus liquid. It is notable to identify the liquid and gas phase contributions and the upper feature is placed below 7 eV. . . . .	63
5.2	The black solid line represents the valence band spectra of the Hexane + Toluene mixture in liquid + gas phase. The red curve represents Toluene liquid + gas features. The lowest contribution in the valence band ranges from 9.6 to 7.3 eV. . . . .	64

5.3	The upper figure shows calibration spectra of CsPbBr <sub>3</sub> and CsPbI <sub>3</sub> aligned with Toluene and Hexane features. The liquid Toluene's lowest contribution in the VB ranges from 9.6 to 7.3 eV, as reiterated in red in Fig.5.1. These findings demonstrate the important role of XPS spectra in studying the electronic structure of materials. . . . .	65
5.4	The toluene shake-up C1s spectra. This effect provides valuable insights into the electronic structure of the analyzed material. See text for more details . . .	66
5.5	Valence region. The CsPbI <sub>3</sub> NCs spectrum is shifted upwards according to the right scale . . . . .	67
A.1	The two sets of curves on the top refer to the Pb 4f for AF and OLA from the left to the right. Both exhibit oxidation species (in light red and green) in particular AF has an extra Pb oxidate species in gray. On the bottom OLA and AF spectra for Cs 4f and Br 3d. Cs region reveals only one type of Cs however the Br 3d has 2 types which were widely discussed in the main text. . . . .	80
A.2	Following the colors initially defined in the 600 eV spectra, we once again observe the same color scheme for both OLA and AF records: Pb 4f ions in light red and Pb oxide species in green and gray. Cs 4f and Br 3d 2 are indicated in purple for ionic Cs and in blue for the oxidized state." . . . . .	81
A.3	Fitting for both 850 eV (in orange circle dots) and 1500 eV (in blue circle dots) from AF records (as it was not possible to acquire signal from Cs and Br for OLA NCs). The color scheme follows the same pattern as at 600 eV: Pb 4f ions are represented in light red, Pb oxide species in shades of green and gray, ionic Cs 4f in purple, and oxidized Br 3d 2 in blue. Exceptionally, the 1500 eV spectra only exhibited two types of Pb species among AF spectra. . . . .	82
A.4	The first figure is from the first scan where we have two types of Pb in red and green. For the bottom figure we have three Pb features the same two types from the first (the red and green features) but now followed by a third one in gray. . .	83
A.5	Spectra for Toluene C1s region for a beamline slit increasing at 10, 25, 50, 60, 75, 100 and 150 $\mu\text{m}$ , respectively, from below to upward. The C1s has two features: the gas phase on the right (the most protuberant contribution) and liquid phase on the left . . . . .	84
A.6	The values of the distance between the gas and liquid peaks (at the ordinates) as a function of the photon flux aperture from the beamline (at the abscissas) are illustrated above. The points gave us two possible functions: exponential and quadratic. Since as much closer the photon flux approaches zero on the exponential curve, the distance goes to infinity, so we used the quadratic one. . .	85

A.7	Cs and Br fitting. The circles in pink are experimental points, and the solid black curve is the sum of all peaks. Black straight lines are the background, solid red is Voigts, and blue residue. In the top spectra, we added two extra peaks: around 84 to 82 eV and another 70 to 68 eV. In the bottom fitting also were added two extra peaks, but now one of them was an arc-tangent shape covering from 84 to 68 and the other from 71 to 69 eV. The objective was to get a fitted line as close as possible to the experimental data. See text for more details. . . . .	89
A.8	Blue dots refer to the Cs and Br OLA spectrum residue. We produced a histogram from the scattered blue points (the top image in green). From the histogram, we could get the respective Gaussian Distribution which has a $\sigma = 32.08$ . . . . .	90
B.1	Scheme of the one-dimensional model sample composed by the solvent (blue) and the CsPbBr <sub>3</sub> NC. The black, purple, and green balls represent the Cs, Pb and Br atoms, respectively. . . . .	95

# LIST OF TABLES

2.1	The nominal binding energy ranges for selected elements in their elemental forms as observed in X-ray Photoelectron Spectroscopy. . . . .	31
A.1	Values for the photoionization cross-section as a function of photon energy [eV]. . . .	80
A.2	The binding energy distance between elements peaks from all Amine-Free spectra. . .	82
A.3	The binding energy distance between elements peaks. . . . .	83
A.4	Here we present the BE for AF and OLA of the Toluene C1s as well as Pb and Cs-Br with their spin-orbit contributions. The last values show us the AF-OLA shift, which might give us a hint about the Ionization potential for the two different methods. . . . .	86
A.5	The $\sigma$ for each spectrum measuring the spread in the distribution about the mean value (zero). . . . .	87
A.6	The values for the area uncertainty, which is related to the element amount in the sample. It was considered the maximum uncertainty between the $+\sigma$ and $-\sigma$ . . . . .	88
B.1	Relaxation energies $E_{rel}$ , in meV/f.u., and surface energies, in meV/Å <sup>2</sup> , for all considered terminations. . . . .	93

# CONTENTS

<b>1. INTRODUCTION</b>	<b>18</b>
<b>2. BASIC CONCEPTS IN X RAYS PHYSICS</b>	<b>21</b>
2.1 Why Use Synchrotron Light . . . . .	21
2.2 What Do We Need from Synchrotron? . . . . .	25
2.2.1 X-ray Photoelectron Spectroscopy . . . . .	26
2.2.2 The Electron Mean Free Path . . . . .	32
2.3 Complementary Techniques . . . . .	33
2.3.1 X-ray Diffraction . . . . .	33
2.3.2 Transmission Electron Microscopy . . . . .	34
<b>3. CSPBBR<sub>3</sub> PEROVSKITES IN A SOLID-STATE PERSPECTIVE</b>	<b>36</b>
3.1 XPS Solid-State Approach for MHP . . . . .	37
3.2 Evidence of oxidation induced by radiation using solid-state samples . . . . .	37
<b>4. MHP CORE-LEVEL XPS APPLYING MICROJET APPROACH</b>	<b>43</b>
4.1 The MHP Scenario . . . . .	43
4.2 The Perovskite NPs under Micro-jet Operation . . . . .	46
4.3 The MHPs Nanocrystals Core-Level Analysis . . . . .	50
4.4 Complementary Characterization . . . . .	54
<b>5. MHP'S VALANCE BAND APPLYING MICROJET APPROACH</b>	<b>61</b>
5.1 The Valence Band in Solid/Aqueous Interface . . . . .	62
5.2 Solvent Features: Valence Band Spectra and Satellite Effects . . . . .	63
5.3 The Environment's Influence on Perovskite Electronic Properties . . . . .	66
<b>6. CONCLUSION</b>	<b>68</b>
<b>BIBLIOGRAPHY</b>	<b>71</b>
<b>APPENDIX A. XPS FITTING/CALIBRATION AND UNCERTAINTY DETERMINATION</b>	<b>79</b>
A.1 XPS Fitting . . . . .	79
A.2 XPS Calibration . . . . .	82
A.3 Uncertainty: Residual Analysis . . . . .	85
<b>APPENDIX B. NANOCRYSTAL THEORETICAL MODEL</b>	<b>91</b>
B.1 Nanoparticles Model . . . . .	91
B.1.1 b) Relation between XPS signal and surface stoichiometry . . . . .	94

# 1 INTRODUCTION

---

Energy sources have become a matter of great importance in our society and from where we acquire them. Furthermore, we demand a renewable and efficient energy supply, bringing us to the Solar cell semiconductor's next generation: Metal-halide Perovskites (MHP). They have attracted attention for their optoelectronic, electronic, and photovoltaic applications and remarkable properties such as high absorption coefficients in the visible region, long free charge carrier diffusion lengths, defect tolerance, high performance, low cost, and abundance. Despite all these qualities, their long-term stability in environmental conditions remains a problem to solve, e.g., the effect of insulating organic ligands at the MHP' surface [5]. Apart from the use as a deposited absorber layer in solar cells, [6–8], the MHP may be employed as a gain media for laser [9–11] and light-emitting diodes (LED) [12–14]. In this thesis, we focus on CsPbBr<sub>3</sub> MPH NCs to critically evaluate the sources of their long-term instability on an atomic scale. These NCs belong to the Cesium Lead Halide Perovskite family (CsPbX<sub>3</sub>, X = Cl, Br, and I or mixed halide systems Cl/Br and Br/I). One of its many interesting properties is that by changing its halide or halide mixture, the band gap, its visible emission, and absorption wavelength can be tuned through the entire visible spectra. To compare, silicon has a band gap of 1.1 eV, thus absorbing photons in the near-infrared part of the spectrum and missing all the visible solar spectrum. Consequently, an ideal silicon conventional solar cell efficiency is always smaller than 29 % [15]. Placing this efficiency in the context; recently a tandem Si/perovskite device reached 33.7 % while a single perovskite cell reached 26.1 % efficiency [16].

Protesescu et al. develop a chemical synthesis route for CsPbX<sub>3</sub>MPH NCs resulting in perovskite nanocrystals with bright colloidal dispersions [17]. Unfortunately, the produced MHP presented low colloidal and phase stability. This stability is related to the fact that poor colloidal stability means that Perovskite tends to clump together or stop being uniformly spread out in the solvent, which can cause its optical and electronic properties to decrease. The surface chemistry of CsPbBr<sub>3</sub> NCs presents issues and problems because they use oleylamine to dissolve the lead halides, which are key ingredients. Oleylamine is a big molecule that can sometimes make the material less stable, causing it to break down over time. To solve the stability problems, Yassitepe et al. (2021) developed an amine-free synthesis strategy that used only OA as a surface ligand and tetraoctylammonium halide as a halide source. This resulted in more stable colloidal dispersions of CsPbX<sub>3</sub> NCs compared to Protesescu's method. The new synthesis method using oleic acid as the single stabilizing ligand has improved the stability of MHPs, remaining stable in solution for a more extended period. Although the improvement in the colloidal stability of amine-free CsPbX<sub>3</sub> NCs seems

to be related to the absence of OLA<sup>+</sup> species in the NCs manufacturing, there is still a lack of knowledge about the surface chemistry for the material obtained at this condition. Questions to be answered: What are surface properties on an atomic scale? How might the organic ligand affect the photostability of AF PNCs under continuous UV light [18]?

X-ray Photoelectron Spectroscopy (XPS) is element-specific and can probe the surface or interface characteristics by adjusting photoelectron kinetic energy. In this way, XPS can help elucidate the surface structure of the CsPbX<sub>3</sub> NCs. So far, only NCs produced by Protesescu's method have been studied by XPS in the literature. Until now, the experiments have used solid samples susceptible to contamination, radiation damage, radiation oxidation induced by radiation, and charging [4]. Nonetheless, Ravi et al. [4] conclude that NCs produced by Protesescu's method contained part of its Cs replaced by OLA<sup>+</sup> species. It is unclear whether the XPS signal comes only from the surface or if some originate from the layer beneath the surface at a specific photon energy. What is the surface composition of the NCs based on energetics and the XPS core line cross-section corrected branching ratios? The Ravi et al. study also observed a Br species chemically inequivalent to the Br in bulk. They claim that Br atoms are surface atoms. In this thesis, we plan to critically evaluate whether these Br atoms are not radiation-induced oxidized atoms. We bring a comparison between the solid sample and the micro-jets strategy.

In the micro-jet technique, the colloidal NCs suspension is injected in a 25-micrometer jet inside the vacuum chamber at about 50 meters per second. The micro-jet crosses with the synchrotron X-ray beam, and the photoelectron is collected by an electron analysis containing several differential pumping stages. For an X-ray beam of about 65 micrometers (FlexPES horizontal beam size), The NCs are exposed to radiation during  $1.3 \times 10^{-6}$ . This means that compared to a solid-state XPS measurement taking only one second, we have reduced the radiation dose by a million times. We applied this new technique to probe CsPbX<sub>3</sub> NCs made with both synthesis and search for changes in the NCs' atomic surface based on the Pb 4f, Cs 4d, and Br 3d corrected for photoionization crosssections at 600 eV energy photons. Also, based on the core levels, branching ratios, and DFT calculation on the orthorhombic geometry (most accurate than many previous studies using cubic geometry), we determine the surface composition of the 6-12 nano-meter NCs. We propose an alternative surface termination for NCs smaller than 1 nm, which may improve stability.

We compare dried samples and the micro-jet strategy applied to MHPs for XPS analysis. The liquid micro-jet shows no chemically shifted Br or Pb atoms on the surface. This may point out that previous studies may indeed suffer from radiation-induced oxidation. To prove the plausibility of this finding, we recorded solid samples made from both samples and observed oxidation-induced Pb lines as well as Br. Previous radiation damage studies on solid samples support our assignments [19].

MHP Ncs suspended in vacuum were previously studied in the literature [20]. Previous studies have not quantitatively determined the relative intensity of the XPS signal

from the surface to the bulk layer by layer. MHP turned out to be an excellent nanomaterial for this type of study. The first layer consists of Br Cs atoms, while the next layer comprises  $\text{PbBr}_2$ . The heterogeneity, our theoretical simulations, and high-resolution microscopy images showed us that about 1/4 of the signal comes from the second layer compared to the first at 600 eV photons. This finding holds for any NCs independent of their position from the liquid vacuum surface and is valid for solid samples. We enhanced the prediction of the amount of Cs substitution in one of the synthesis methods. Substitution of the Br atoms was also analyzed.

Some of the remarkable properties of these NCs seem to come from the fact that the highest occupied molecular orbital HOMO or valance band maximum (VBM) lies above levels formed when contaminants are eventually attached to the NCs. They are considered “defect tolerant” [21] [22], another unique characteristic of these materials, unlike other semiconductors that are intolerant to defects. Defects derive from interruptions in the original crystal lattice or impurities. Such defects can be electronically inert or induce electronic states close (i.e., smaller or equal  $k_B T$ ) to the edge of conduction or valence band, the so-called shallow traps. These traps do not harm the device’s performance, mainly affecting the charge carrier’s adequate mobility. On the other hand, when defects introduce electronic states located within the bandgap of the semiconductor, so-called deep trap states, charge carriers have no null probability of being captured and wasted. These trapped charge carriers bring about additional non-radiative recombination phenomena, deteriorating the overall device efficiency. To contribute to this electronic structure of the NCs, we have performed valence spectroscopy studies on MHP made of  $\text{CsPbBr}_3$  and  $\text{CsPbI}_3$  using 120 eV photons. These experimental results were also compared with quantum mechanical calculations.

The sensitivity of XPS to the detection of atomistic/intermolecular interplay and electronic structure chemical dynamics on liquid surfaces has been carried out since Hans and K. Siegbahn [23] in which it was first proposed a method to study liquid samples back when the XPS studies were limited to liquids with vapor pressures considerably lower than 1 Torr. This limitation excluded measurements involving water and most aqueous solutions. The breakthrough in using aqueous samples took place with the advent of the liquid microjet setup by Faubel et al. [24]work, which developed a previously unavailable field. Then, this technique was applied in most synchrotron facilities worldwide.

## 2 BASIC CONCEPTS IN X RAYS PHYSICS

---

The study of X-rays began with Wilhelm Röntgen discovery (also called Röntgen rays), who first produced and detected radiation at a wavelength range of 0.01–10 nm [25]. Rontgen also showed that these X-rays could be used to make images by picturing finger bones and a ring surrounded by shadowed flesh. Since then, X-ray physics has offered new possibilities for investigating the structure of matter at its fundamental level.

When X-rays interact with matter, the photoelectric effect is one of the resulting processes. By analyzing the kinetic energy of the emitted photoelectrons, we can examine the surface chemical properties of materials, including Perovskites. We plan to demonstrate this in this thesis. Photoelectron Emission (PE) spectroscopy is a versatile and highly effective method for surface analysis, especially within the semiconductor domain [26]. Over the last few decades, substantial progress has been made in enhancing XPS instrumentation and refining data analysis techniques. These advancements have improved spatial resolution and reduced data acquisition times, amplifying the technique's capabilities. X-ray emitted from synchrotron sources is a key for micro-jet-based spectroscopy. Synchrotron radiation offers tunable photon energy and high flux and intensity, enabling sensitive and precise XPS data collection.

### 2.1 Why Use Synchrotron Light

There are different particle accelerators, and their use differs in what you want to investigate. Cyclotrons are meant to accelerate charged atomic or subatomic particles in a spiral track; Betatrons, in turn, accelerate electrons in a circular geometry; nonetheless, we will focus on Synchrotrons. X-rays produced in these facilities possess properties such as brightness, high collimation, coherence, and polarization [27]. Synchrotron is a term that refers to accelerating electrons at speed close to the speed of light ( $c$ ). At the same time, magnetic fields change their direction, giving them a radial acceleration (circular motion) and emitting light in the radial direction, as one can conclude from electromagnetism. A crucial part of this investigation involves the utilization of XPS at Synchrotron facilities.

#### **An Overview of the Source**

Synchrotron facilities hold cutting-edge X-ray sources for material probing, relying on radiation produced in a Storage Ring (SR). An electron gun initially generates electrons, then accelerated by a linear accelerator (Linac) to energies traveling millions to Giga electronvolts (eV). Radiofrequency electric fields propel these particles to higher energies, compensating

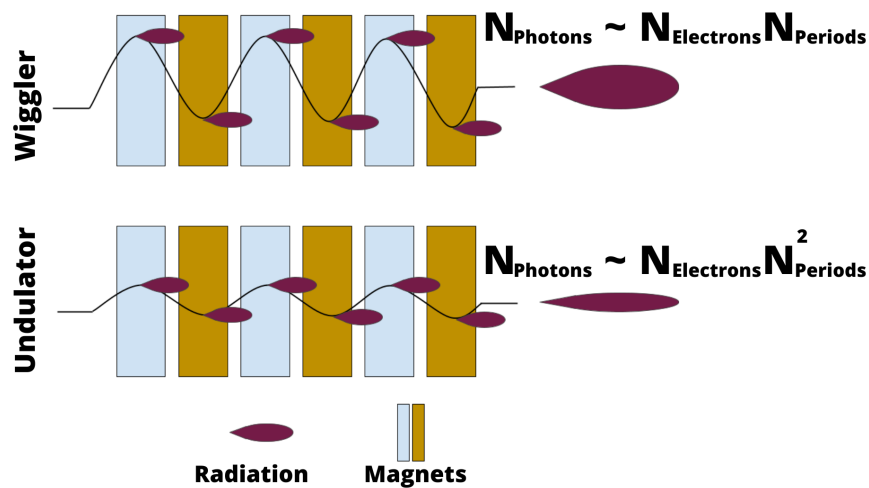


Figure 2.1: In an Undulator, the short oscillations produce sharp peaks. The wiggler acts like a combination of several bending magnets; the spectra distribution is similar to the bending magnet but differs in the overall intensity. The Undulator differs from the two later in that the Undulator shows off narrow spectra distribution due to the overlapping and interference.

for energy loss during each orbit within the SR. Once electrons are within the SR, synchrotron light is generated when the path of electrons is bent using magnets or insertion devices (IDs) such as undulators or wigglers (see Fig.2.1). These devices allow more efficient production of X-ray beams than by retaining the electrons orbiting in a purely circular path. Wigglers are constituted of periodic magnet arrays placed in storage ring straight sections, emitting light in short pulses. On the other hand, undulators optimize beam quality and polarization by producing narrow, uniformly spaced radiation bands due to the overlap and interference of radiation fields. Synchrotron sources evolved in four generations, characterized by advancements in beam brilliance, spatial coherence, and beam size. These improvements are essential for applications like micro-jet-based spectroscopy, which requires smaller X-ray beam diameters, resulting in reduced beam waste and enhanced resolution and detection capabilities in analytical experiments. The beamlines used in this project were from SIRIUS-Brazil and MAX-IV/Sweden.

### Synchrotron Main Parameters

The remarkable properties of synchrotron radiation are defined by classical electromagnetism and special relativity (such as the Lorentz contraction and the Doppler shift). We plan to discuss significant aspects of the Synchrotron beam. First, charged particles release electromagnetic radiation as soon as they are accelerated. The radiation emission occurs according to the electron velocity: the emission for velocities well below  $c$  differs from when it gets close to the speed of light. For particles traveling well below  $c$ , its radiation emission pattern is  $\cos(2\theta)$ , spreading to large angles along the movement axis. Once the particle acquires relativistic movement, it emits radiation in a collimated beam in the direction they are traveling. The consequence of the beam emission is the “loss” of energy by the accel-

erated electrons. After the third-generation Synchrotrons, the undulator insertion devices optimized the radiation emission intensity by photon constructive interference at specific emission energies. The energy of the constructive interference can be changed by changing the gap between the undulator magnetic structure. Below, we will discuss some fundamental concepts essential to describing a beam.

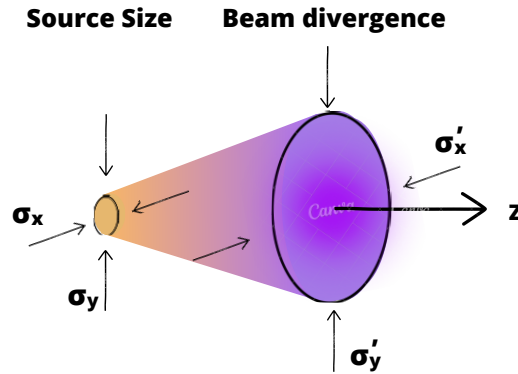


Figure 2.2: Above, we have the four parameters defining a beam's emittance x and y. The brilliance is inversely proportional to both the source size and the x-ray beam divergence

**a) Flux and Intensity** The spectral flux,  $\Phi$ , is defined as the average number of photons per second,  $n_{ph}$ , per unit bandwidth (where only photons in 0.1% bandwidth contribute to the flux at a certain photon energy) going through a specific area, e.g., at a nominal photon energy of 1000 eV, only photons/second within the 999.5 - 1000.5 eV band contribute to the Flux.

$$\Phi = \frac{n_{ph}}{\Delta t} (\Delta\omega/\omega). \quad (2.1)$$

Intensity is the average energy per unit of time flowing through the cross-section area  $A$ . In quantum mechanics, we deal with the number of photons per time and area. The energy density is related to the number of photons and their frequency,  $\nu$ :

$$\Phi = \frac{n_{ph} h\nu}{A\Delta t}. \quad (2.2)$$

**b) Brilliance and Emittance** Brilliance is how the flux is dispersed in space and angular direction and determines the smallest spot onto which an X-ray beam can, in principle, be focused. It is defined as

$$Brilliance = \frac{\text{photons/second}}{(\text{mrad})^2 (\text{mm}^2 \text{ source area}) (0.1\% \text{ bandwidth})}. \quad (2.3)$$

The Brilliance of a source depends on its size and the angular divergence of the

emitted radiation being considered as a distribution (Fig. 2.2). Emittance is connected to an area or volume in the phase space of the particles. There are two phase space variables for each spatial direction. The spatial extensions are often given as the standard deviation of this distribution,  $\sigma_x$  and  $\sigma_y$ , in the horizontal and vertical direction, respectively. Likewise, the angular distribution of the beam is described by the standard deviation of the intensity around a nominal direction,  $\sigma'_x$  and  $\sigma'_y$ , again the horizontal and vertical plane, respectively. The product of the linear source size and the beam divergence in the same plane is known as the emittance:  $\epsilon_x = \sigma_x \sigma'_x$  and  $\epsilon_y = \sigma_y \sigma'_y$ .

**c) Coherence** Coherence refers to the statistical similarity between one wave or multiple waves or wave packets, as depicted in Figure 2.3. When referring to coherent light, the photons oscillate at a consistent frequency and have wavelengths that are in phase. Conversely, incoherent light has photons that oscillate at different frequencies and are not in phase with one another. There are two types of coherence in synchrotron radiation: temporal and spatial. Temporal coherence relates to the time correlation between different points along the wavefront propagation direction. This means that temporal coherence describes how a monochromatic wave can propagate. Spatial coherence, on the other hand, correlates with points in space along the transverse direction. Spatial coherence fundamentally describes how uniform the phase of the wavefront is. We are unaware of how coherence could benefit the technique in electron spectroscopy.

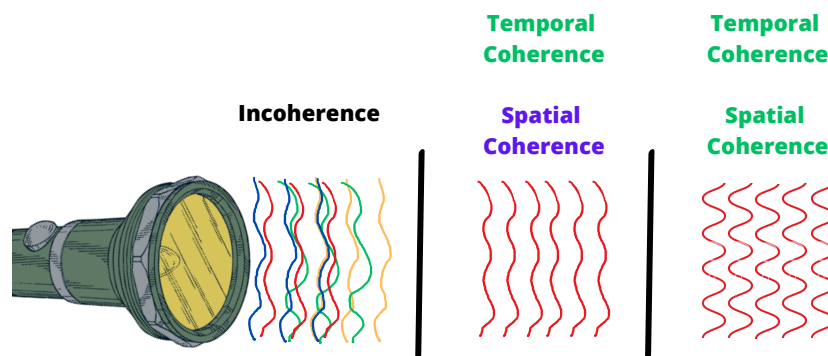


Figure 2.3: Radiation coherence refers to wave properties' statistical similarity and correlation. Above, one can see an incoherent signal turning into a temporal and spatial coherent. Temporal coherence relates to time correlation along the wavefront propagation, and spatial coherence reflects correlation in transverse spatial points. Temporal coherence determines monochromaticity, while spatial coherence indicates wavefront phase uniformity.

## Radiation and Matter

Radiation is the emission of energy as waves or particles. It can either be ionizing or non-ionizing. Ionizing radiation has enough energy to break molecular bonds or remove elec-

trons from atoms, while non-ionizing radiation only has energy for excitation.

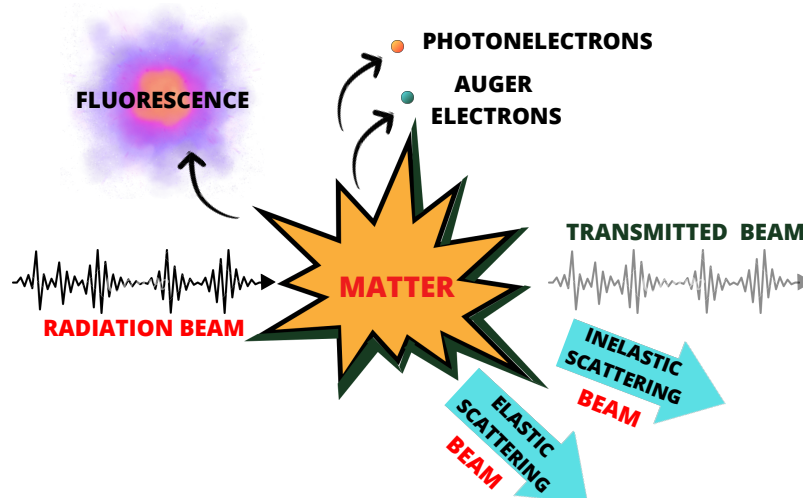


Figure 2.4: Diagram of Matter and Radiation interaction where an initial radiation beam (it may be electrons, photons, neutrons, ions) hits the matter, resulting in additional or secondary radiation (Photoelectric Effects, Scattering Fluorescence Emission). The radiation can either not cause any change or alter the material structure (bulk, surface).

When radiation interacts with matter, two main phenomena can occur: absorption and scattering. The interaction between matter and radiation is fundamental in Synchrotron light research. In the energy range of interest for synchrotron radiation, two processes are mainly the absorption and the scattering (Fig.2.4). Absorption estimates the ability of a sample to attenuate a photon flux going through it, providing details on the distribution of the energy levels of a sample and giving a picture of the sample's electronic and vibrational properties. Looking up the absorption of a photon may display the excited state; when the excited state is above the vacuum level, one or more Photoelectrons can be emitted; the study of the properties of these Photoelectrons gives rise to photoemission spectroscopy. Looking up the electromagnetic Spectrum (see Fig.2.5) in the ultraviolet and X-ray range, the system may also undergo decay processes with the emission of fluorescence photons or Auger electrons or the fragmentation into neutral/ionized fragments.

From the scattering interaction, we come across a series of probabilities that incoming photons are diffused by the matter, changing their direction of propagation. The scattered beam can be classified as elastic (no energy exchange between the photons and matter resulting). It may also be inelastic (resulting in outgoing photons whose energy differs from the incoming ones).

## 2.2 What Do We Need from Synchrotron?

The branch of science that deals with measuring and determining physical, chemical, mechanical, and structural properties of materials is called Material Characterization. Various

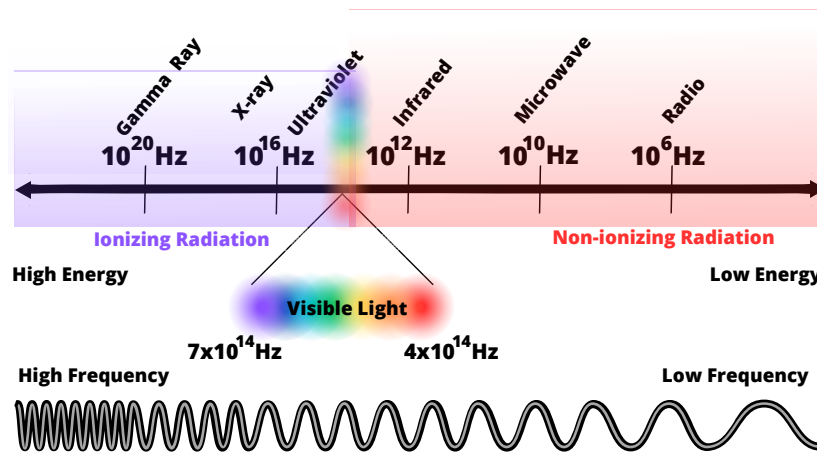


Figure 2.5: A electromagnetic spectrum diagram showing the non-ionizing and ionizing regions. The energy and frequency increase from the right to the left. The lowest frequency, radio waves, are transparent to the human body. Microwaves induce molecular rotation and torsion, while infrared induces molecular vibration. The visible light produces electron excitation to upper quantum levels. Ultraviolet light contains enough energy to ionize its target. X-rays hold enough energy to eject core electrons or scatter them. Besides the photoelectric effect and scattering, gamma rays can generate pair production.

techniques are available to characterize any material, depending on the information you want to extract (see Figure 2.6).

Among the characterization techniques, my PhD project proposed analyzing data from nano Perosvikite through X-ray Photoelectron Spectroscopy (XPS). X-ray spectroscopy deals with the interaction between radiation and matter, observing the photoelectrons coming from the sample. The methodology is based on the photon-electron effect, where it is possible to analyze the electron kinetic energy,  $E_k$ , as a function of the beam energy,  $h\nu$ , and the Binding Energy,  $E_b$ , associated with the electron's orbital. Einstein photoelectric effect formula is used as the basis for this methodology:

$$E_k = h\nu - E_b. \quad (2.4)$$

The synchrotron-based XPS permits shining monochromatic electromagnetic radiation ( $h\nu$ ) on a sample, causing the ejection of electrons with well-defined energy, which allows specifying the elements that make up the sample.

### 2.2.1 X-ray Photoelectron Spectroscopy

The main results of this work were from using data analysis over XPS. This technique is an analytical method that measures the kinetic energy of photoelectrons. By tuning the photon to match, or often, to surpass the BE of an electron belonging to an element, chemical information can be obtained from the surrounding environment of the respective atom. The ionized electron's Binding energy (BE) presents a chemical shift compared to the isolated element. This shift reveals changes in the chemical environment to which the atom is bound.

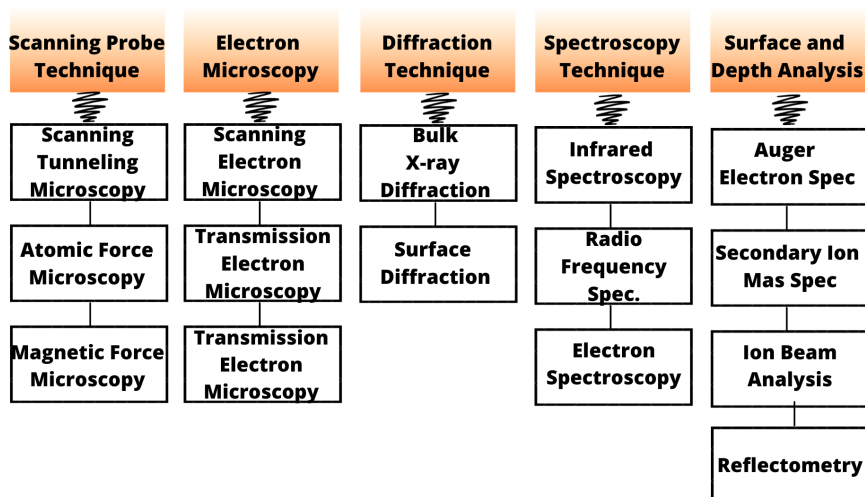


Figure 2.6: An overview of Characterization Techniques utilized in scientific research and analysis branches. Each technique offers unique capabilities for investigating the properties and structures of materials, enabling in-depth analysis and understanding of various scientific phenomena."

The XPS setup requires detectors and analyzers to measure the intensity of emitted photoelectrons as a function of their kinetic energy. However, different types of samples require unique arrangements. For example, liquid samples require a specialized setup with a nozzle or capillary system to generate a stable liquid jet, allowing for an in-situ probe of suspended nano-particles or droplets in a carrier gas. When analyzing liquid samples, it's important to choose a beam size that matches the dimensions of the liquid microjet. It is also possible that the sample is a thin film or solid substrate with a deposition layer serving as a reference. These samples are placed on a sample holder or stage during analysis.

We faced several challenges in studying the colloidal dispersions containing MPH directly in their liquid environment **without using a microjet**. In XPS, the emitted photoelectrons can only reach the detector under reasonable vacuum conditions. Indeed, the electron mean free path needs to be about the size of the experimental chamber. A pool of liquid having around 20 mbar pressure at room temperature subjected to a vacuum suitable for XPS will freeze in seconds due to evaporation. If we overcome this problem, further issues need to be addressed: (1) The interface of liquids is particularly prone to contamination due to the high diffusion rate; therefore, even a small amount of contaminants can migrate to the interface with great potential to spoil scientific findings. (2) Many liquids are molecular compounds and therefore susceptible to X-ray radiation damage; (3) Typical solutes give XPS signal so low that longer acquisition time or large photon flux is needed to obtain reasonable statistics; this factor increases the impact of points (1) and (2) substantially. Therefore, there is a great need for a technique to study liquid/solid interfaces free from contamination and radiation damage.

The solution to the above-mentioned problems is studying the liquid/solid interface with XPS based on microjet insertion methods. The approach was designed to use nanoparticles (NPs) as solids and shares three key advantages compared to other sample in-

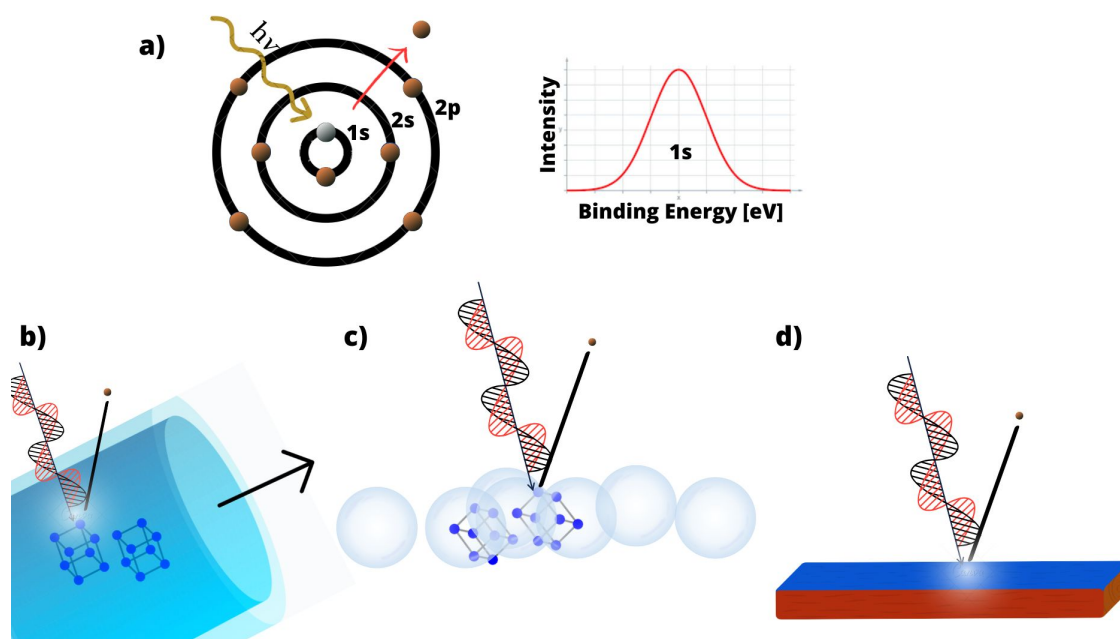


Figure 2.7: X-ray Photoelectron Spectroscopy (XPS) consists of ionizing the sample with a photon beam of energy  $h\nu$ . The process involves a photon-in electron-out scheme, which generates typical spectra. A nozzle or capillary system generates a liquid jet for nano-crystal analysis in colloidal dispersion. Gas-phase samples or aerosol particles require an inert carrier gas aerosol beam that suspends the crystals. A sample holder or stage is utilized for solid samples, where the sample is typically a thin film (the blue part on the surface) with a solid substrate as a reference, such as a metal (the bottom part in red). [1]

sersion methodologies. (1) They allow studies of the interface between a solid surface and a solvent in a colloidal phase. (2) They avoid the problem of radiation damage since the sample is continuously renewed. (3) They completely avoid sample contamination. However, it is important to emphasize that microjet is not the only insertion method for liquid samples in a vacuum chamber compatible with XPS. In reference [28], the authors describe various methods for preparing liquid interfaces in XPS experiments, considering factors such as experimental goals, thermodynamic conditions, and vapor pressure. Different preparation techniques are presented, including fast-flowing liquid jets and droplet trains, which offer advantages such as reduced beam damage and surface contamination. These methods allow XPS experiments to achieve high vacuum conditions and obtain reliable results with improved signal-to-noise ratios. Another point to ensure accurate analysis is the size of the X-ray beam, which must be carefully evaluated. The beam's spatial resolution, interaction volume, and signal-to-noise ratio are affected by its size. Critically, the beam size should align with the area covered by the liquid microjet. A beam too large might extend beyond the microjet boundaries, including areas without liquid. These areas may contain vapor from the solvent, contributing to overlapping lines in the XPS spectrum. Researchers can maintain a stable sample surface while obtaining the desired quality XPS spectra by selecting a beam size significantly smaller than the liquid microjet dimensions, i.e., one-micrometer diameter or lower.

Using XPS, we can analyze the electronic, optical, mechanical, and magnetic

properties of atoms, molecules, and condensed matter by examining their core and valence electrons. XPS is alternatively called electron spectroscopy for chemical analysis (ESCA) [29]. A Photoelectron can be attributed to a one-electron energy level (e.g.  $nlj$ ) where  $n$  is the principal quantum numbers 1, 2, 3, 4, ...;  $l$ , the angular momentum 0, 1, 2, 3... denoted by s, p, d, f... and finally, the total angular momentum is given by the absolute value of the sum of angular ( $l$ ) and spin ( $s$ ) momentum  $j=|s + l|$ .

### Core-level Spectra

Core-level spectroscopy is a powerful tool that investigates the behavior of core electrons in materials [30]. By creating core holes, which are vacancies in specific core levels, the lifetime of these vacancies can be evaluated, aiding in understanding decay mechanisms. XPS analysis, an essential technique in core-level spectroscopy, enables examining deeper electron levels specific to each element, which can also be called as element-specificity (see Fig.2.8). This analysis provides valuable information about elements' abundance and chemical state within a sample. The relationship between core-level peak area and the amount of an element in a material surface can be determined through photoionization cross-section corrections.

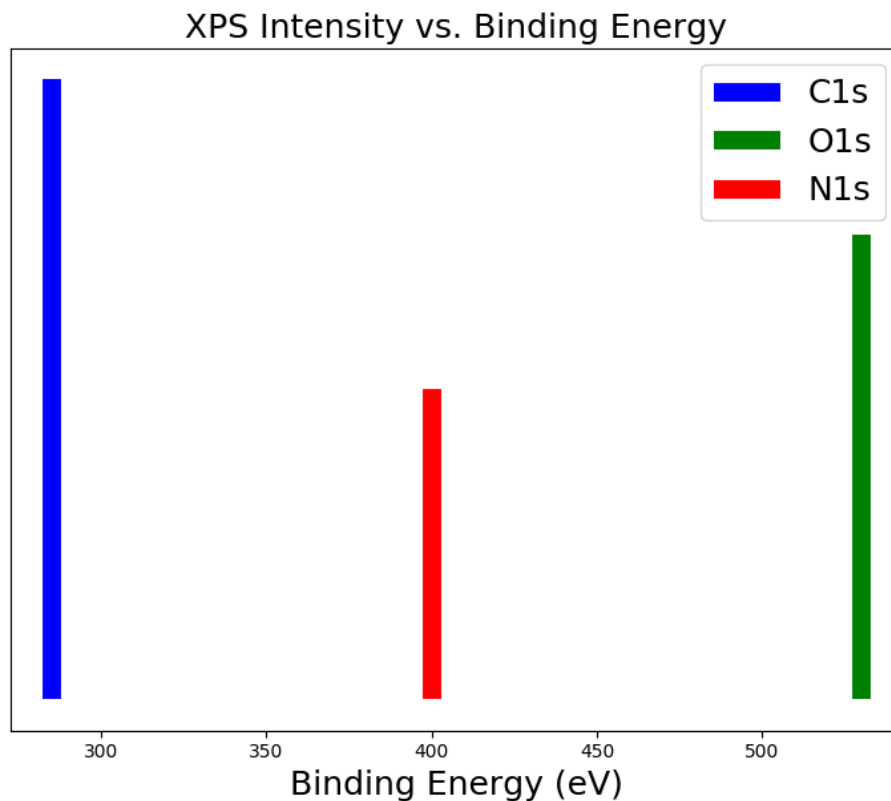


Figure 2.8: XPS Photoemission Peaks: 1s orbitals of C, O, and N elements. Notice how distinct peaks emerge from the same orbital, enabling precise elemental identification in the samples.

## Satellite Features

Shake-up satellites are transitions that can be identified in higher BE concerning the main ionization peak, corresponding to a process where one electron is excited from the valance band to the unoccupied levels during core-ionization. This description is based on the single-particle approximation.

In addition, the shake-up satellite peaks' intensity can alter depending on the compound and its constituents [31]. Distance between these satellite peaks and the core-level peak is determined by the energy differences between the filled and empty molecular orbitals, often associated with the energy of the highest occupied molecular orbital (HOMO). In addition to the shake-up features, another process can occur, such as shake-off, where the second electron is ionized. (see Fig.2.9).

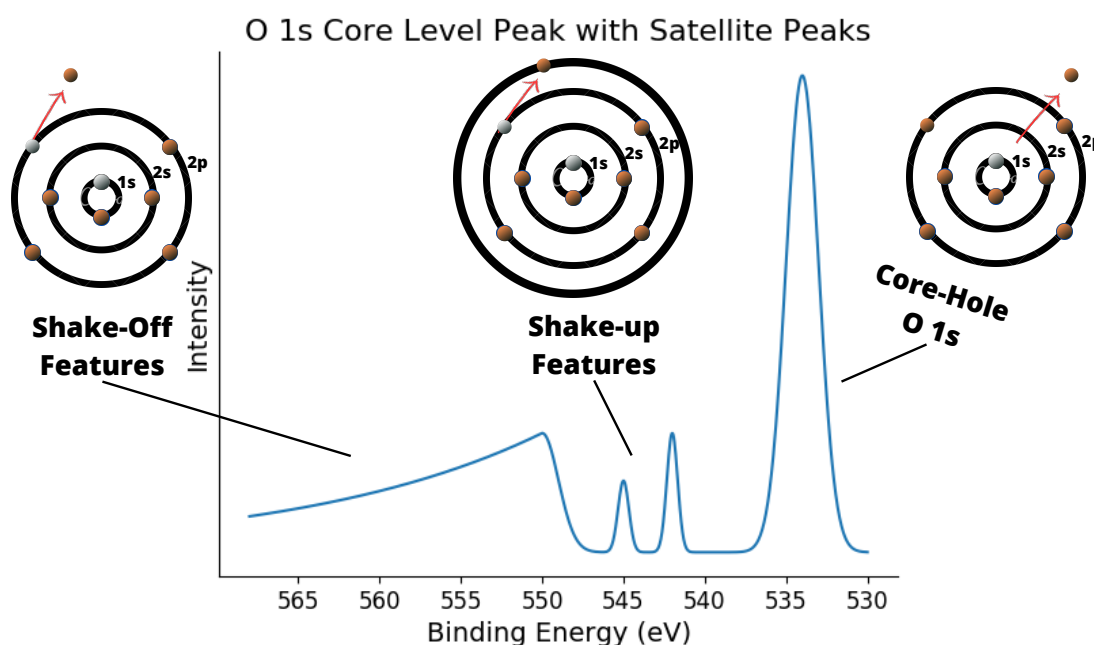


Figure 2.9: The figure shows a Python simulation of the core level and its satellite peaks. The O 1s core level is positioned at 534 eV. A valence electron is promoted to a higher energy state upon photoionization, resulting in two peaks between 540 and 550 eV for high binding energies. This interaction causes the energy in the core electron to reduce, leading to a satellite structure positioned a few eV below the core level on the kinetic energy (KE) scale. The Shake-off satellite effect is observed with its maximum at 550 eV and shows a tail that exponentially decays. This effect involves the complete ejection of a valence electron from the ion into the continuum, broadening the core level peak observed in XPS spectra or contributing to the inelastic background due to the wider range of energies associated with valence electrons compared to core electrons.

## Chemical Shift

As discussed in the subsection XPS core-level analysis, the photoemission lines are element-specific. Furthermore, the chemical environment produces a shift in the core electron binding energy, called a chemical shift [32]. In Table A.4, you can find the binding energy and associated core orbital for Carbon (C), Nitrogen (N), Oxygen (O), and Silicon (Si). As depicted

in Fig2.10, Carbon exhibits a positive shift of the 1s orbital binding energy when it bonds with more electronegative elements. This occurs because the more electronegative bonding elements attract the outer electrons of Carbon, leaving the inner electrons more susceptible to the coulomb force of the nucleus, thereby increasing their binding energy.

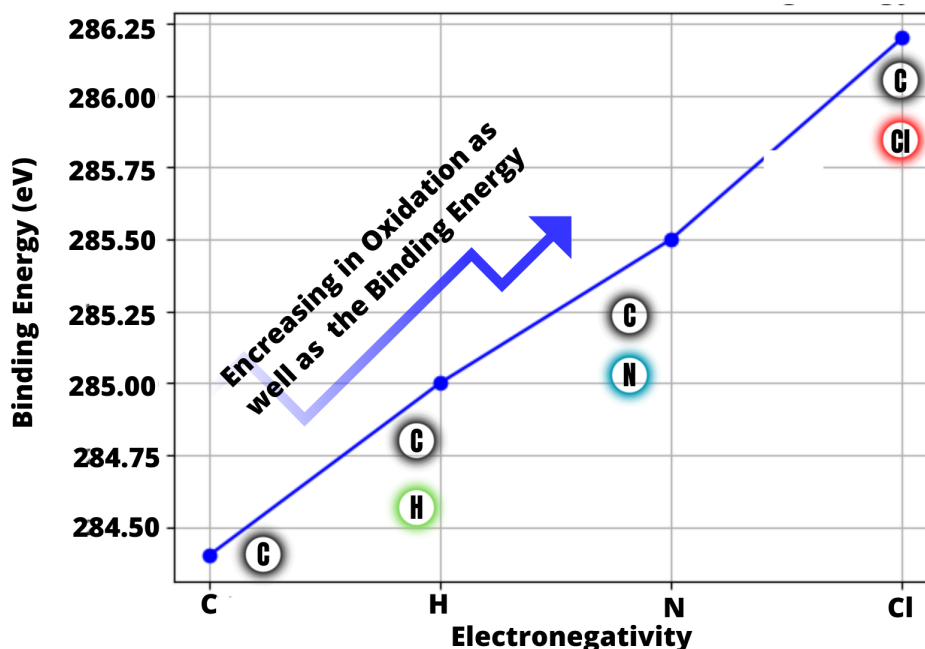


Figure 2.10: The oxidation state of carbon affects the C1s binding energy in XPS. As oxidation increases, the C1s peak shifts to higher binding energies where on the x-axis is the element bound to C and on the y-axis is the value for the respective binding energy. Chemical bonds with hydrogen, nitrogen, or chlorine induce higher binding energy than Carbon alone (in response to the increasing electronegativity: Cl > N > H). Oxidation increases the electron density of carbon, resulting in higher binding energies.

Element	Binding Energy (eV)
Carbon (C1s)	284.5 - 285.1
Nitrogen (N1s)	396.1 - 400.5
Oxygen (O1s)	526.2 - 533.5
Silicon (Si2p)	98.8 - 99.5

Table 2.1: The nominal binding energy ranges for selected elements in their elemental forms as observed in X-ray Photoelectron Spectroscopy.

### Core-level Multiplet Splittings

This phenomenon results in a splitting of spectral lines due to the interaction between electron spin and its orbital angular momentum. The splitting depends on the degree of spin density delocalization of the electrons in the valence orbitals. Therefore, one expected a more electron-withdrawing group (with a higher degree of spin density delocalization) would be associated with a larger spin-orbit splitting. The photoelectron state is identified by  $nlj$  level. A doublet peak structure contribution is observed for electron transitions from levels

with a total angular momentum higher than  $s$  ( $l = 0$ ), that is, for  $p$ ,  $d$ ,  $f$ . Whereas all  $s$  peaks are singlets, all other levels are doublets with slightly different energies. The energy separation of the two adjacent peaks of the same orbit (same  $n$ ,  $l$ ) increases with atomic number and decreases for the same  $n$  with higher  $l$  values. This indicates that spin orbit-coupling interactions are significantly larger for atoms further down a particular periodic table column. For example, the binding energy of the  $2p_{1/2}$  and  $2p_{3/2}$  is practically the same for Mg, which are  $E_b(2p_{1/2}) = 49.6$  and  $E_b(2p_{3/2}) = 49.2$  eV (see Fig. 2.11).

The total electronic angular momentum ( $j$ ) is determined by combining orbital angular ( $l$ ) and spin ( $s$ ) momenta. For  $l \neq 0$ , like in  $p$  orbitals, the line is a doublet with states  $p_{1/2}$  and  $p_{3/2}$ . The intensity ratio for the  $p$  orbitals doublet is  $1/2$ , while for  $d$  orbitals, it is  $2/3$ . The intensity ratio for the  $p$  orbitals doublet can be calculated as follows:

Lower energy state ( $p_{1/2}$ ):

$$2j - +1 = 2(1/2) + 1 = 2 \quad (2.5)$$

Higher energy state ( $p_{3/2}$ ):

$$2j + +1 = 2(3/2) + 1 = 4 \quad (2.6)$$

Therefore, the intensity ratio of the  $p$  orbitals between  $1/2$  (lower energy state) and  $3/2$  (higher energy state) is  $1/2$  (lower/higher).

### 2.2.2 The Electron Mean Free Path

As stated here, XPS provides a tremendous tool to probe the surface environment, but how can we be sure about that? It begins when we take a look at the inelastic mean free path (IMFP, also represented by  $\Lambda_e$ ). The IMFP defines a photoelectron's average distance from a material before undergoing an inelastic scattering event. The photoelectron IMFP as a function of the electron kinetic energy was similar for many materials studied. Therefore, this relation became the universal curve (see Fig.2.12). This curve provides a general trend or behavior observed across various materials. The universal curve of the MFP exhibits a specific trend influenced by different physical processes at varying kinetic energies. At high kinetic energies, the IMFP is large, indicating a longer mean free path due to elastic scattering with outer electrons. As the kinetic energy decreases, inelastic scattering becomes more significant, leading to a decrease in the IMFP. However, at very low energies, the IMFP starts to increase again due to the contribution of multiple scattering events and surface effects. This complex interplay between elastic and inelastic scattering processes determines the observed trend in the IMFP curve.

Quantitatively analyzing photoelectron signals from solute species in aqueous solutions is challenging due to various factors. The lack of reliable photoionization cross-

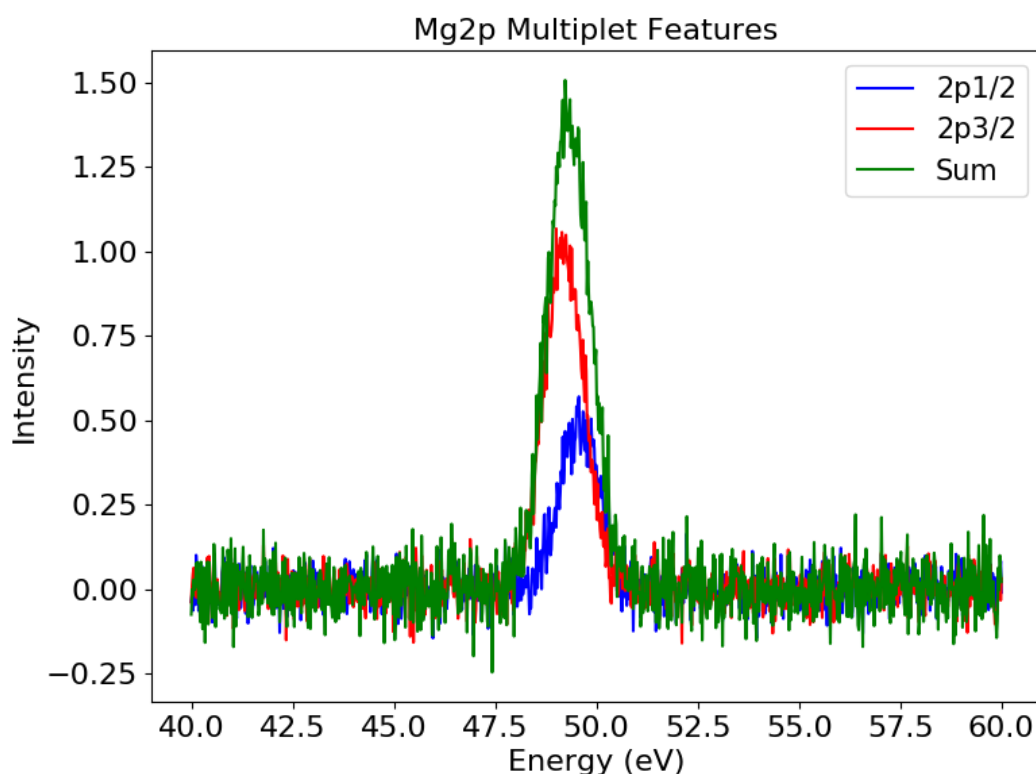


Figure 2.11: Above, one sees the depiction of Spin-orbit splitting and electron transitions in photoelectron spectra for Mg 2p transitions generated in Python, including noises in the signal features. The binding energies of 2p<sub>1/2</sub> and 2p<sub>3/2</sub> in Mg are nearly identical, 49.6 eV and 49.2 eV, respectively. The energy separation between adjacent peaks within the same orbit increases with atomic number and decreases for higher *l* values within the same *n*.

sections for solutes poses challenges in comparing the intensities of different species. The dependence of electron signal on detection angle, particularly for surface emission, is poorly understood.

## 2.3 Complementary Techniques

In scientific research, reporting tangible results requires multiple procedures. Different approaches will give you diverse information. then it is common practice to use a combination of experimental techniques to ensure the accuracy of material analysis. Thus, throughout our project, we utilized various methods to support our findings. The next section outlines the underlying principles of other techniques that assisted our findings.

### 2.3.1 X-ray Diffraction

When investigating MHP morphology, we utilized X-ray Diffraction (XRD) measurements based on the interaction between X-rays and the crystalline structure. So when the radiation

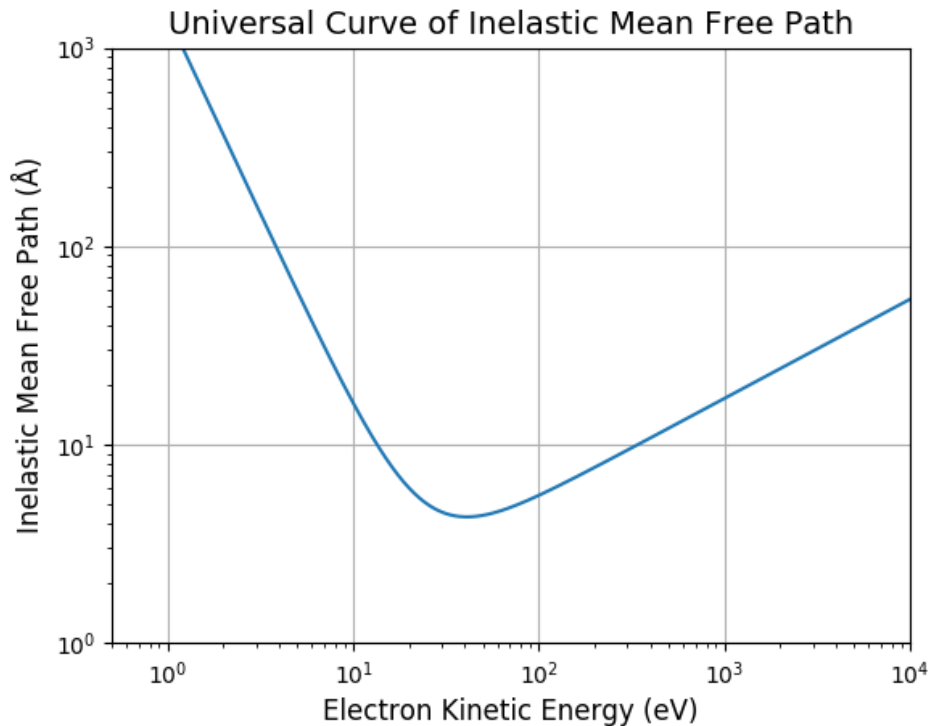


Figure 2.12: The curve above was plotted in Python, which illustrates the relationship between electron kinetic energy and the inelastic mean free path (IMFP) in condensed matter (Adapted from [2] where a fitting was produced based on [3]). The curve is described by the equation  $\Lambda_e = 1450/(\varepsilon_e^2) + 0.54\sqrt{\varepsilon_e}$ , where  $\Lambda_e$  represents the IMFP in angstrom units and  $\varepsilon_e$  represents the electron kinetic energy in electron volts (eV). The graph shows a logarithmic scale on both the x-axis (ranging from 0.1 to 10,000 eV) and the y-axis (ranging from 0.1 to 1000 Å).

interacts with a crystalline structure, diffracted images are produced through the constructive interaction between the outgoing X-ray reaching the detector. X-rays that have been dispersed are recorded based on the angles at which they scatter, forming a pattern that follows Bragg's Law ( $n\lambda=2d \sin \theta$ ). This pattern is associated with the distance between atoms. XRD allows determining the angle  $2\theta$  between the incident and diffracted x-rays by moving the sample or the detector. The analysis looks for the crystal structure, which is linked to the fact that every crystal configuration creates a specific diffraction pattern [33].

### 2.3.2 Transmission Electron Microscopy

Transmission Electron Microscopy (TEM) is an electron-based material characterization and analysis technique. It involves the projection of an electron beam through a sample affixed to a holder. The transversal interaction between electrons and the sample results in the formation of an image, magnified and directed toward an imaging system, which can take various forms, such as a fluorescent screen. The imaging system may take diverse forms, including a fluorescent screen, photographic film, or a sensor coupled with a scintillator and charge-coupled device. One of TEM's valuable attributes is its ability to provide crystal lattice structure images, which facilitate the measurement of lattice distances, unit cell dimensions, and

crystal orientations. These data play a crucial role in enhancing our understanding of materials at the nanoscale [34,35].

### 3 CsPbBr<sub>3</sub> PEROVSKITES IN A SOLID-STATE PERSPECTIVE

---

As a first step to probe the MHPs' surface properties and modifications, we conducted XPS measurements in the dried-out dispersion of NPs on a silicon substrate. For simplicity, from now on, we call these studies "solid-state measurements." These measurements were essential in assessing potential damage from radiation or contamination to the NCs under examination. We note that a previous XPS study exists for MHPs produced using the OLA<sup>+</sup> synthesis; possible radiation effects on the sample were not discussed, nor was a quantitative account of the electron mean free path from the surface to the bulk of the NCs were not addressed. We found no solid-state experiment with XPS for the NCs produced by the amine-free method in the literature.

Here, we aim to compare the two samples made with different methods and known to have better stability properties. We performed synchrotron-based XPS where the photon beam energy was 600 eV, 850 eV, 1253 eV, and 1500 eV. The signals from Pb 4f, Br 3d, and Cs 4d photoelectrons are representatives of the surface at the first and second smallest photon energy. In contrast, and according to previous studies [4], the two highest photon energies produce the above photoelectrons probing the NCs bulk.

To access the atomic composition of the NCs according to the synthesis method, we recorded the Pb 4f line corrected by the photoionization cross-section. After this, the corrected photoelectron signal is proportional to the amount of lead in the sample at the depth the photoelectrons come from. Suppose we want to determine the amount of lead atoms in the sample at a specific position. We need to know precisely the number of photons shining in the sample, the analyzer efficiency, and other experimental parameters that are difficult to obtain with acceptable precision. Instead, we analyzed the ratios of the photoelectron line corrected by the cross-section. In this way, all the above difficult-to-obtain experimental factors cancel out.

According to our experimental conditions, it was convenient to access the following corrected ratio (Pb 4f)/(Cs 4d) and (Br 3d)/(Cs 4d). For example, in bulk, this ratio should reflect the sample (PbCsBr<sub>3</sub> stoichiometric proportions or, in other words, Pb/Cs=1, and Br/Cs=3.)

In this solid-state study, we also aim to answer the question: Does the exposure to ionizing radiation over a typical XPS measurement period (one to 10 minutes) cause radiation-induced modifications in the sample? If so, we want to know if the radiation damage is restricted to the surface or how it changes toward the NC bulk. These evaluations will be performed by critically analyzing the XPS spectra and the evaluated ratios.

### 3.1 XPS Solid-State Approach for MHP

XPS is a prevalent technique for analyzing semiconductors in the solid state. Probing samples with X-ray can lead to positive charging due to photoelectron emission. Grounding the sample is common to maintain a crucial constant surface potential; this task is accomplished through various conductive methods [36].

Furthermore, different techniques to induce charge neutralization are used for insulating materials. In the present study, we employed a flood gun to neutralize charging effects in the sample [37].

These practices enable XPS to probe semiconductors in the solid state effectively. The measurements shown here were performed at the IPÊ beamline belonging to the fourth-generation Brazilian synchrotron Sírius.

This beamline is described elsewhere [38]. This user facility is cutting-edge for high-resolution resonant inelastic X-ray scattering (RIXS) and XPS in the soft X-ray range (100 – 2000 eV). The beamline photon energy resolution is projected to be 60.000 at 930 eV. The instrument allows energy scanning and offers versatile beam sizes  $0.8 \times 3.4 \mu\text{m}^2$  for  $\text{cff}=5$  and  $4 \times 5 \mu\text{m}^2$  at 930 eV and  $\text{cff} 2.2$ . The main XPS chamber attached to the beamline usually operates at  $1\text{-}2 \cdot 10^{-8} \text{ mbar}$ . The experimental apparatus also includes a flood gun to eliminate positive charges in the sample through radiating electrons beam over the substrate.

We dropped the colloidal solutions containing NCs on a silicon substrate, followed by natural drying under ambient pressure conditions within a fume hood. Subsequently, 4 sample holders, two containing MHP NCs OLA<sup>+</sup> and two MHP NCs AF (one with a thin layer and another thicker for each method), were introduced into the vacuum chamber for the XPS experiments, facilitating a thorough examination of the solid-state properties. More details about the MHPs synthesis method can be seen in the next chapter.

### 3.2 Evidence of oxidation induced by radiation using solid-state samples

Here, we bring the consequences of adopting the solid-state approach for investigating Perovskite materials. This approach provides a robust avenue for probing semiconductors under operational conditions since their use is meant to be an absorber layer for Solar panels. However, it is noteworthy that this method has unveiled various unfavorable aspects, particularly when assessing the chemical environment of MHPs. We noticed that the XPS spectra started to evolve within a short time after the sample received the incident of the X-ray beam. Immediately after the sample received an X-ray, (staring at a video camera) we could see visible fluorescence, which died out within a few seconds. This behavior suggests that the X-ray beam induced sample degradation. The AF was recorded for all four-photon energies, different from the OLA. The OLA results are presented at 600 and 1253 eV photon energies since

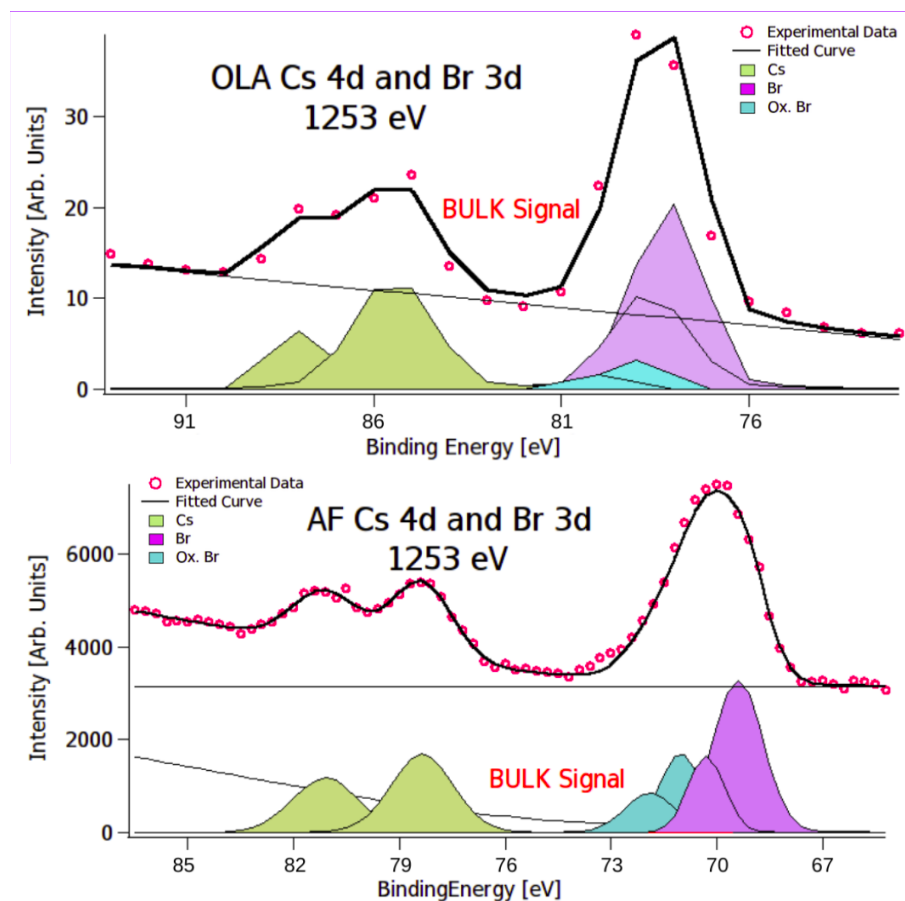


Figure 3.1: The spectra for Cs and Br ionized by a 1253 V photon beam. On the top, one can see the Cs 4d (from 82 to 90 eV) and Br 3d (from 76 to 81 eV). The Cs 4d (from 76 to 83.5 eV) and Br 3d (from 67 to 74 eV) are seen on the bottom. For both NCs, it is possible to identify oxidated Br species in pale blue). The experimental data is in pink circles, and the fitted curve containing all the Cs and Br feature contributions is in black.

we first recorded for these two photon energies; we could not record spectra for the other two selected energies due to a poor signal for Cs 4d and Br 3d regions in the XPS spectra (photoelectron signal loss). It was assumed that this was a result of X-ray damage on the samples. In Figure 3.1, the green region on the left-hand side of both spectra represents the presence of Cs 4d<sub>5/2</sub> and 4d<sub>3/2</sub> at lower and higher binding energy, respectively. The purple peaks correspond to Br 3d<sub>5/2</sub> and 3d<sub>3/2</sub> at lower and higher binding energies, respectively. At slightly higher binding, we observe a second set of spin-orbit split peaks in blue; this higher binding energy of the second set of Br peaks indicates a distinct change in the chemical environment at the sample. This second Br 3d species was consistently observed for all photon energies in both synthesis methods.

The dark higher BE Br 3d peaks have been observed before in the literature [4]. The authors identified these peaks due to the Br at the surface, which they claim was chemically different from bulk atoms. The presence of chemically distinct Br at the surface is inconsistent with more recent XPS results from suspended in vacuum NCs [39]. In this study, the Br 3d spectra show no sign of a second surface species. In reference, [19] the authors critically analyzed perovskites NCs degradation induced by radiation. They found clear signs of

Pb 4f oxidation peaks caused by radiation. Their studies did not look into the Br 3d region; however, from their findings, assigning the dark green extra peaks in both samples as oxidized Br induced by radiation is natural. To further characterize this assignment, we shall analyze the Pb 4f region, which has the advantage of presenting well-separated 4f spin-orbit peaks compared to the Br 3d case. The oxidation of surface species can alter the chemical state of elements, affecting binding energies and chemical compositions. This, in turn, hinders the precise determination of elemental and chemical states, impeding a comprehensive understanding of the sample's properties. No oxidation peaks were observed for the Cs region, which can be explained because Cs is more electronegative than oxygen.

The reader may notice the relatively lower statistical significance associated with OLA than AF, and an emerging trend in the recorded data became evident. This trend implies that achieving higher spectral resolution in the spectra necessitates subjecting the OLA MHPs to prolonged radiation exposure, which subjects the samples to a more deteriorated state.

Previously, it was pointed out that the Pb oxidate states of Perovskites change due to photodegradation under different light-exposure conditions [19].

The study reveals that photodegradation in CsPbI<sub>3</sub> is linked to forming Pb<sup>0</sup> clusters, causing a decrease in photoluminescence quantum yield (PLQY). During photodegradation, Pb oxidation states from Pb<sup>2+</sup> to Pb<sup>0</sup> were recognized through XPS analysis, leading to Pb cluster formation on the quantum dot surface, acting as charge carrier traps.

These findings highlight a concern: if visible light damages the material, what happens with an X-ray beam? We tested our hypothesis by taking successive spectra at the Pb 4f region, as illustrated in Figure 3.2. A normalization procedure was taken to obtain a quantitative comparison between the two curves (OLA and AF). As the area beneath the curves is related to the number of elements, we fitted each curve to its synthesis method and photon energy, respectively. Then, we compared their areas and, finally, the signal difference between each curve. The normalized curves were 0.86 for AF, 0.11 for the blue, and 0.8 for the red curve in the OLA case. The procedure to register the spectra began with recording the spectrum in a new sample spot, and the result is shown as a black continuous line in the figure.

During this first scan, we observed the 4f<sub>7/2</sub> peak at higher binding energy and the 4f<sub>5/2</sub> peak at low binding energy. There were no apparent signs of other chemically distinct lines. After about ten minutes of keeping the X-ray beam at the same spot in the sample, we recorded a new spectrum. The new spectrum shows the appearance of a new chemically shifted species at a high binding energy side to the main Pb lines. This extra feature became even more pronounced when a third spectrum was recorded seven minutes later while the first species decreased.

Similar effects were observed for the NCs' AF syntheses. In Fig.3.3, we used 600 eV photons to analyze the same 4f region at a fresh spot on the AF sample. We show the

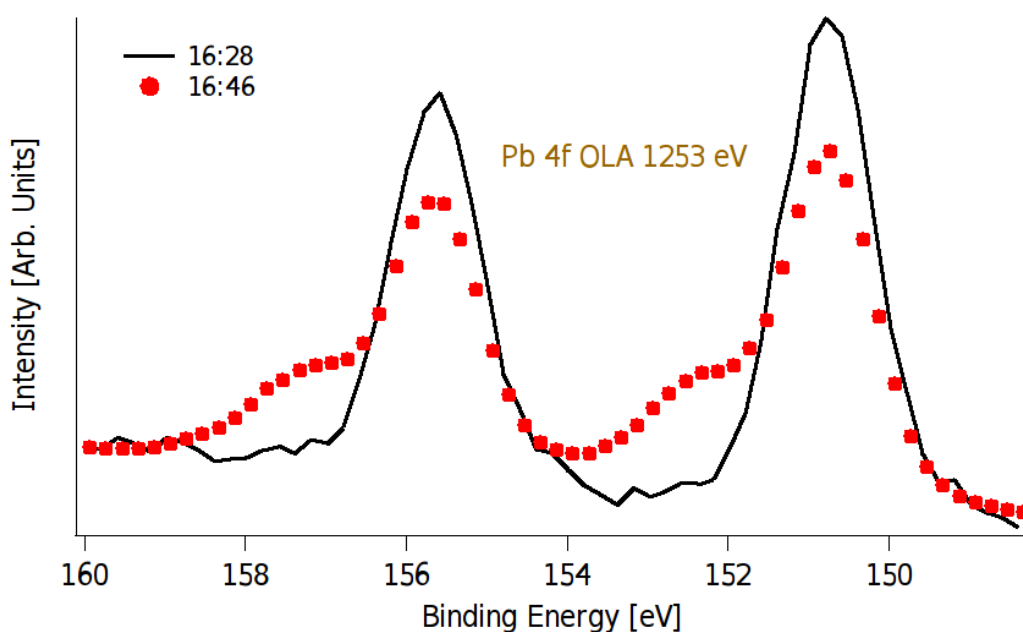


Figure 3.2: In both Nc synthesis methods, Pb oxidation is observed. A normalization procedure was implemented, and we obtained a signal difference of 0.8 between the red and black curves. In the Pb region, the degradation of OLA over time was registered in the black curve at the bottom, indicating no oxidation, and 17 minutes later, recorded from the same spot, a shoulder was present related to a Pb-oxidated state.

spectrum in dark blue. Even at the first recording, the characteristic oxidized state at higher binding energy appears as a shoulder at higher binding energy. After 10 minutes, we record a new spectrum, continuously keeping the X-ray at the same spot.

As can be seen in the spectrum at light blue color, the shoulder becomes dominant, and a third species appears at even higher binding energy. Following the assignments from 3.2 and the evolution observed, we assign the shoulder peaks as oxidation-induced by radiation  $\text{Pb}^{2+}$  species from  $\text{Pb}^0$  species, the main peaks in the dark blues spectrum. A third species appears at an even higher binding energy, with even higher Pb oxidation states.

It is worth mentioning that the  $\text{Pb}^{2+}$  species shoulder was consistently observed even after relocating the X-ray to a new sample spot. This was observed in samples produced by both synthesis methods. It is possible that the sample underwent degradation due to extended exposure to a vacuum without any radiation.

Next, We investigated how this oxidation could affect the XPS areas of Br/Cs and Pb/Cs, which were corrected by the ionization cross-section. Indeed, Ravi et al. [4] presented a chart with an elemental ratio for Br/Cs and Pb/Cs corrected by the photoemission cross-section to analyze the crystal composition. We calculated the areas under each spectrum for the same photon energy and normalized by the cross-section (see Appendix A and check the photoionization cross-section table). The plots were split between OLA and AF for better understanding.

In Fig. 3.4, we show two plots in which the green-filled circles dots are from OLA (on the left) and the blue-filled lozenge dots are respective to AF (on the right), both exhibit-

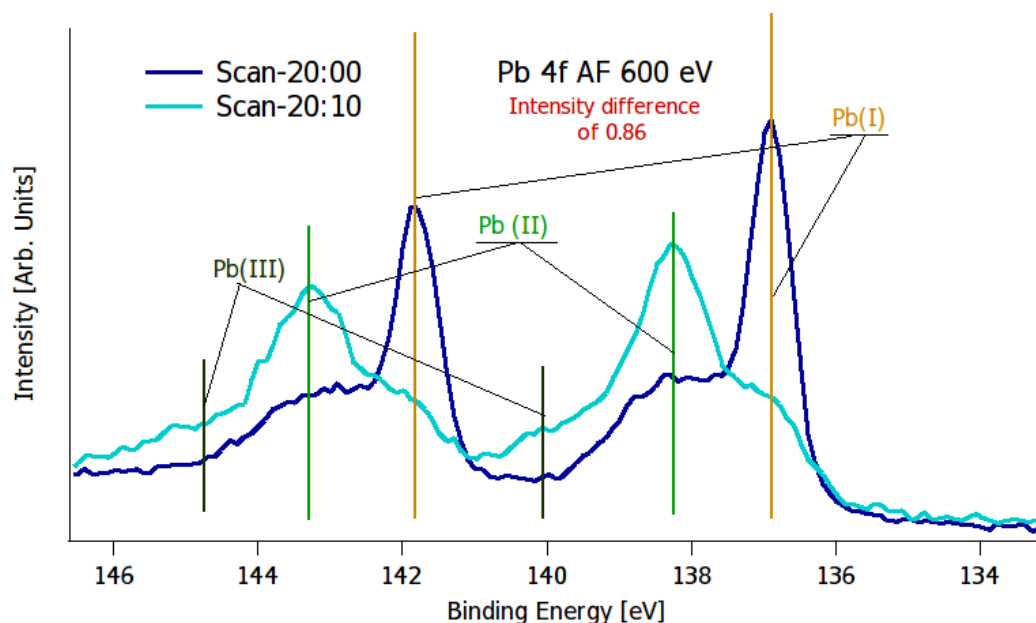


Figure 3.3: A normalization through the area under both curves was employed, and we found a signal difference of 0.86 between dark blue and light blue curves. It is demonstrated that oxidation of Pb in the AF Ncs has a distinguished behavior from the OLA case. Two Pb species are visible - one at a lower binding energy (Pb I) and another at a higher binding energy (Pb II), which is smaller due to an oxidized state. After 10 minutes, the oxidized species increases in size and becomes more prominent than the first species, leading to an inversion of proportion between the two species over time. Additionally, the late picture may depict the emergence of a third species with another oxidation state, Pb III.

ing the Pb/Cs (in red lines) and Br/Cs (in black lines). Also, the yellow dotted lines correspond to Ravi et al. [4] results OLA<sup>+</sup>. The dotted blue line at ratio 3 (1) corresponds to the bulk Br/Cs (Pb/Cs) stoichiometric ratio ( Notice that from the bulk composition, CsPbBr<sub>3</sub> leads to Pb/Cs=1 and Br/Cs=3). The Br/Cs ratio in the OLA+ sample is about five when exposed to 600 eV photons (representing the surface of the NCs) but decreases to slightly more than two at 1253 eV (representing the bulk of the sample). The OLA lines follow a similar trend as observed in the study by Ravi et al. However, the Br/Cs ratio at the bulk (1253 eV) is smaller than the stoichiometric ratio, which suggests that there may be a loss of Br atoms compared to Cs atoms. An interesting finding is the consistently larger Pb/Cs ratio for both photon energies. This indicates that Cs and more Br atoms are missing from the surface and bulk of the OLA<sup>+</sup> NCs.

In Figure 3.4, we analyzed the amine-free sample's Pb/Cs and Br/Cs ratios at four-photon energies. We observed that the Br/Cs ratio is higher near the surface, tending to 3 at the NCs bulk. These results are similar to Ravis's, but there are some discrepancies within the error bars. This behavior indicates that radiation-induced oxidation significantly affects the ratio, which raises questions about concluding the pristine sample from the solid state XPS results. Additionally, we found that radiation damage in AF NCs is less gradual than in the OLA case. The ratio does not smoothly shift from around 5 to 3 along the photon energy range studied.

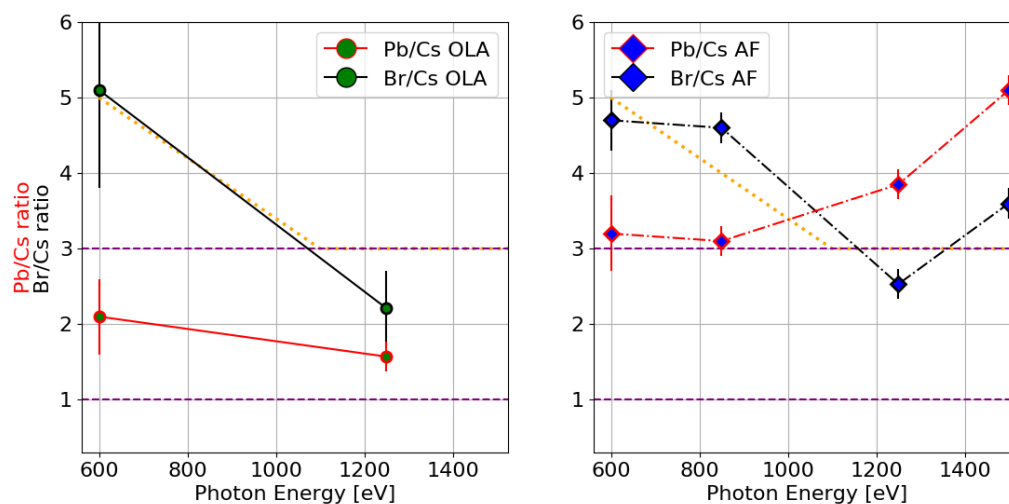


Figure 3.4: We present the Pb/Cs and Br/Cs ratios for two different methods of synthesizing MHPs. These ratios are shown as a function of Photon Energy and are corrected by the photoionization cross-section. The results are displayed in two plots, with green-filled circles representing the OLA method on the left and blue-filled lozenge dots representing the AF method on the right. The red lines show the Pb/Cs ratios, while the black lines depict the Br/Cs ratios. The yellow dotted line represents the Br/Cs trend in the Ravi et al. study. The change in the ratio from around 5 to 3 indicates the expected composition of NCs from surface to bulk due to the photoelectron mean free path as a function of its excitation energy. The purplish dashed lines (3 for Br/Cs and 1 for Pb/Cs) represent the expected values for bulk.

The Pb/Cs AF sample ratio significantly departs from 0.5 at the surface (see next chapter) and one at the bulk. The Pb/Cs are five times larger than expected in the bulk. Combining the Br/Cs and Pb/Cs ratio information, we conclude that radiation damage, augmented by vacuum damage, induces substantial loss of Br and Cs atoms from the sample as a whole.

The most important conclusion is that, despite the Amine-free sample being more stable under ambient pressure and conditions than the  $OLA^+$ , this sample is substantially more prone to radiation and vacuum damage than the  $OLA^+$ . To solve these severe problems when analyzing the dry sample with XPS, we will introduce a new XPS way to study NCs in colloidal dispersion in the next chapter.

## 4 MHP CORE-LEVEL XPS APPLYING MICROJET APPROACH

---

To overcome the limitations in studying MHP NCs in the solid state, we planned to use a new micro-jet sample insertion system in combination with XPS. We aim to investigate the crucial surface properties associated with organic capping ligands. As previously mentioned, MHP NCs are synthesized in a colloidal phase, which provides improved solar properties, photovoltaic efficiency, and cost-effectiveness. MHPs, such as  $\text{CsPbX}_3$  ( $X=\text{Cl, Br, I}$ , or combinations of the three atoms), show different bandgaps according to the halide component or its mixture. However, their colloidal stability is still a challenging research field. MHP NCs synthesized through an amine-free approach show improved stability. However, there is a shortage of knowledge about the atomic structure of MHP NCs' surface interface. Here, we plan to address this problem.

### 4.1 The MHP Scenario

Perovskite crystal is described by the formula  $\text{ABX}_3$  (where A is an organic or inorganic cation, B is a metal cation in the octahedral coordination state, and X is a halogen anion). Occurring naturally as a mineral of calcium titanate, portrayed by the chemical formula  $\text{CaTiO}_3$ . This mineral was first discovered by the German mineralogist Gustav Rose in 1839 and was named in honor of the Russian mineralogist Lev Perovski (first reported in [40]). Studies have shown that synthesizing Perovskites for optoelectronics in Solar Cells (the smallest unit of Solar Panels) [41], [42] firstly involved organic-inorganic hybrid compounds. Perovskites are manufactured in a colloidal phase, making them a nanomaterial. Consequently, it is more efficient and low-cost [43], [44]. A colloidal substance is a mixture in which one substance is the dispersion medium through which particles are dispersed. The motivation to investigate the MHPs (Metal Halide Perovskites) in the form of colloidal NCs (Nanocrystals) has its roots in the results obtained from colloidal Quantum Dots (QDs) of conventional semiconductors [45], [46]. Classical QDs are nanoparticles or nanocrystals of a semiconducting material with range diameters of 10 to 100 nanometers, in which the quantum confinement effects lead to a collapse of the continuous energy bands (conduction and valence) of the bulk material into discrete, "atomic" energy levels [47]. The discrete structure of energy states leads to the discrete absorption spectrum of QDs (schematically shown by vertical bars in Fig. 4.1a), which contrasts the continuous absorption spectrum of a bulk semiconductor. At the same time, the QD Band Gap can be tuned by adjusting its size (Fig. 4.1b). The fact that the semiconductor is on the nanoscale implies the size of the material becomes comparable to

or smaller than the de Broglie wavelength of electrons. So, the energy levels undergo quantum confinement, where the pair electron-hole distance is compared to the exciton<sup>1</sup> Bohr radius:

$$E = \left( -\frac{1}{\epsilon_r^2} \frac{\mu}{m_e} R_y \right), \quad (4.1)$$

where  $R_y$  is the Rydberg's energy ( $R_y = 13.6$  eV);  $\mu$  is the reduced mass of the exciton system (electron-hole);  $\epsilon_r$  is the dielectric constant;  $m_e$  is the effective mass of the electron. Also, decreased QD results in a higher degree of confinement, producing an exciton of higher energy for bigger band gap energy.

Besides the size dependence, MHPs have optical and electronic properties directly related to their composition. Permuting the Halide in  $\text{CsPbX}_3$  one tunes the bandgap (covering all the visible spectral region). In classical QD, the emission spectrum is highly sensitive to the particle dimension, e.g., the narrow spectral distribution, which is critical in display with a big range of colors, depends on a uniform size distribution. Additionally, it requires strict temperature and time control in the synthesis procedure and introduces extra costs in manufacturing [17]. From here on, among different types of synthetic Perovskite, we will concentrate on the inorganic MPH NCs, which can be synthesized using two methods. First reported by Protesescu et al. [17] using a nonpolar solvent synthesis method for  $\text{CsPbX}_3$  in which  $\text{PbX}_2$  salts were solubilized in oleylamine/OA capping agents in a non-coordinating solvent. It turned out that the NCs have great efficiency for optoelectronic applications: distinct narrow emission line widths of 12-42 nm; high quantum yields of 50-90%; and short radiative lifetimes of 1-29 ns (check on Protesescu. et al.). Although the synthesis method above had a good result, they exhibited poor colloidal stability and readily precipitated from the crude solution.

This synthetic approach encountered stability challenges when using oleylamine as a ligand for solubilizing the lead halide precursor. Oleylamine, being a long-chain organic molecule, introduced instability to the perovskite material, leading to degradation over time. Likewise, it involves the application of multiple competing ligands, intensifying the complexity and potential instability. A novel synthetic strategy was devised to overcome these obstacles, employing oleic acid as the exclusive stabilizing ligand and introducing a distinctive halide precursor; it was reported in [48]. The strategy that was developed involves the use of Quaternary Alkylammonium Halides as precursors, which eliminates the need for oleylamine. This new method, called Amine-free, enables the production of conductive PQD films through solution processing with reduced organic content and increased stability. However, although this new method enhances stability, the atomic surface remains poorly understood.

---

<sup>1</sup>Exciton is a quasiparticle formed by the bonding state of an electron and a hole. This quasiparticle is responsible for transporting energy without transfer charge only by diffusion in the material (material's structure, temperature, and the presence of defects)

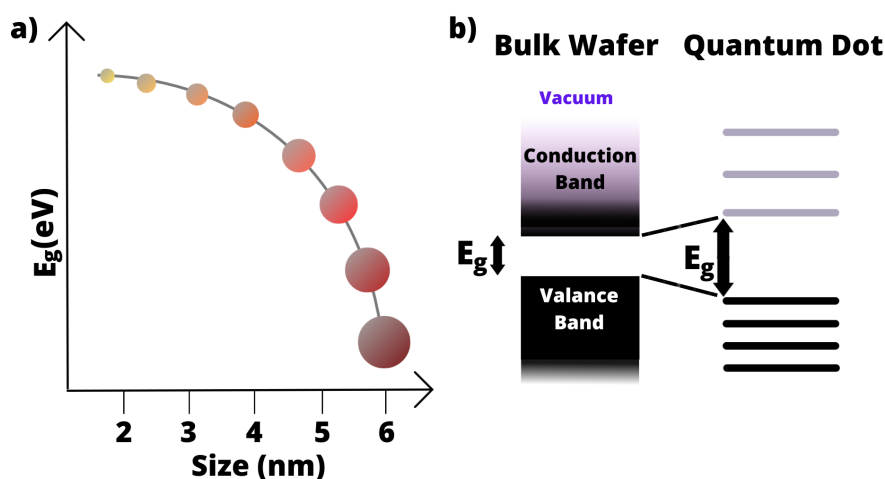


Figure 4.1: a) Studies have observed that the absorption coefficients of Quantum Dots (QDs) obey a power law. This is because as the size of the QD decreases, there is a higher degree of quantum confinement, which produces an exciton of higher energy. As a result, the band gap energy increases. By using models and spectroscopic measurements of the emitted photon energy, it is possible to measure the band gap of QDs. b) Due to quantum confinement, QDs have discrete "atomic-like" states in the conduction and valence regions compared to semiconductors of macroscopic sizes. This confinement occurs when the size of the nanoparticle is smaller than the exciton Bohr radius, which is led by the size shrinking that collapses the bulk material's continuous energy bands into discrete ones.

Another extraordinary property of the MPH NCs is that their band gap is free from levels formed when contaminants are attached to the NCs, making them "defect tolerant." This characteristic is unique to these materials, unlike other semiconductors that are intolerant of defects [49], [50]. Defects derive from interruptions in the original crystal lattice or impurities. Such defects can be electronically inert, or they can induce electronic states close to the edge of the conduction or valence band, the so-called shallow traps. These traps harm the device's performance, affecting the charge carrier's effective mobility. On the other hand, when defects introduce electronic states located within the semiconductor bandgap, so-called deep trap states, charge carriers have no null probability of being captured and wasted. These trapped charge carriers bring about additional non-radiative recombination phenomena, deteriorating the overall device efficiency.

Even with their "defect tolerance" feature, adjusting the band gap of nano-crystals for certain applications is still necessary. The occupied level binding energies of these crystals are best studied using ultra-violet electron spectroscopy, although Resonant Auger spectroscopy can also be used to enhance the valence levels of minority-diluted nano-materials compared to the liquid valence levels. Meanwhile, X-ray Absorption Spectroscopy, which is element-specific, can be used to examine the unoccupied orbitals.

Other studies about Perovskites analyzed their surface interplay, chemical environment, and structure. In a study by Ravi et al. [4], the authors proposed a method for understanding the binding mechanism of organic ligands on the surface of  $\text{CsPbBr}_3$  NCs produced with  $\text{OLA}^+$  synthesis using mainly XPS. However, this method is problematic as

the probing X-ray can cause oxidation and damage to the sample within seconds (see last chapter). Additionally, the previous study did not assess the distribution of the photoelectron signal as a function of the NCs layer from the surface to the bulk. The substitution proposed in the surface at the publication was based on information from Nuclear Magnetic Resonance (NMR), but this technique is not element-specific. Therefore, it is necessary to probe the OLA<sup>+</sup> sample studied in that text to assess possible surface substitutions impacting the NCs' stability accurately.

Another study in the literature investigated lead halide Perovskite CH<sub>3</sub>NH<sub>3</sub>PbBr<sub>3</sub> nanocrystals suspended in a vacuum. In this case, the sample was introduced in a vacuum by an aerodynamic lens [39]. We plan to use this study to support some of the conclusions in this chapter.

Conversely, the present work presents a novel design methodology that combines the characterization of liquid samples by a Cylindrical Microjet combined with X-ray Photoelectron Spectroscopy (cMJ-PES).

## 4.2 The Perovskite NPs under Micro-jet Operation

Liquid samples in XPS studies present distinct challenges and complexities compared to solid and gas samples. Physical properties (density, mobility, and surface tension) affect the solid-state and liquid samples' behavior under synchrotron radiation. These differences lead to variations in signal intensity, probing depth, and spectral resolution. Furthermore, gas-phase samples differ from solid and liquid samples due to their lack of surface and highly mobile nature, requiring specialized preparation and measurement techniques. In liquids, the surface imposes difficulties such as lower signal intensities, chemical shifts, and background contributions, further complicating data interpretation. The liquid samples for Photon Emission Spectroscopy (PES) were not used until the late 1980s. Its experimental realization finally came in 1997 [51]. To study liquids using X-ray techniques, one must fulfill specific conditions. Which enclose the following aspects: maintaining the liquid sample within a vacuum environment, ensuring its stability under high-vacuum conditions, guaranteeing the absence of contamination, arranging the liquid sample in a thin layer or beam to facilitate signal separation between the liquid and vapor phases, continual renewal of the liquid surface to enable an analysis of fresh samples, preventing condensation on electron optical elements during measurements, sustaining consistent sample conditions over prolonged recording periods.

Cylindrical Microjet X-ray Photoelectron Spectroscopy (cMJ-PES) meets all these requirements and provides reliable and accurate insights into the properties and environment of liquid samples, thereby enhancing our understanding of various phenomena and facilitating advancements in numerous scientific disciplines. When dealing with larger jet diameters or higher temperatures, molecular collisions with the photoelectrons become more

pronounced, [52]. A thorough understanding of and effectively controlling these factors are paramount for a microjet setup's successful assembly and operation. The geometry and dimensions of the microjet and the preservation of laminar flow play crucial roles in ensuring the existence of a smooth and undamaged cylindrical section. Additionally, the length of the turbulence-free region of the microjet can be fine-tuned by adjusting the flow velocity following Plateau–Rayleigh instability [53, 54], which describes at what distance from the nozzle the micro-jet decays into droplets. By conscientiously considering these factors, one can optimize the microjet diameter ( usually 10 to 25 micrometers) and operating conditions ( Usually a flow rate of 0.7 ml/minute), facilitating precise and controlled surface studies.

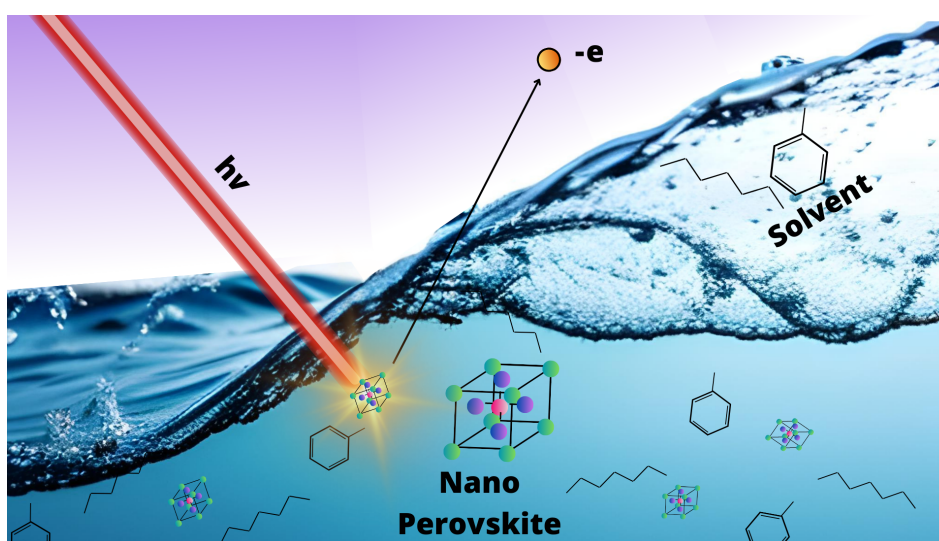


Figure 4.2: A depiction of the XPS technique applied at the liquid-solid interface. A well-tuned X-ray beam ( $h\nu$ ) interacts with the nanocrystal surface immersed in a solvent mixture, emitting photoelectrons. The analyzer then captures these emitted electrons, providing valuable information about the chemical environment surrounding the nanocrystal.

Ambient Pressure X-ray Photoelectron Spectroscopy (APXPS) is an alternate method for analyzing liquid samples. However, there are certain challenges and limitations that this method faces. Specialized instrumentation is required to handle higher pressures, which means the sample must be exposed to an ambient gas environment, and it can be challenging to maintain vacuum conditions. Moreover, gas molecules can weaken the photoemission signal and limit the probing depth of the near-surface region. This results in lower surface sensitivity compared to MJ-PE.S [55, 56]. Radiation damage in induced oxidation, as well as contamination, is also a problem in this technique.

Consequently, cMJ-PES remains a more suitable choice for the detailed characterization of surface chemistry and electronic properties in MHP NCs. Synchrotron facilities worldwide incorporated cMJ-PES experiments using a specialized setup that utilizes a small nozzle to generate a thin stream of liquid exposed to the synchrotron radiation beam. This setup provides a high degree of control over the liquid flow rate and temperature, facilitating the execution of experiments under a wide range of conditions. The diagram in Fig.4.2

demonstrates how the cMJ-PES setup effectively tackles the issue of exploring the surfaces of frequently used liquids with high vapor pressures (HPV). These liquids pose a challenge for investigation under vacuum due to their tendency to freeze or evaporate. However, despite cMJ-PES's success in combination with HVP liquids, a limited number of research studies have been conducted on nanoparticles that are diluted in HVP liquids using cMJ-PES techniques.

One reason for this absence is the short photoelectron effective attenuation length (EAL) in liquid, e.g., for water, the EAL is about  $2\pm 1$  nm at 100 eV, and it is  $6\pm 4$  nm at 600 eV [57, 58]. NPs tend to remain away from the liquid-vacuum interface. Obtaining XPS signals from NPs typically requires 600 eV photoelectrons, even for NPs larger than six nm [59]. Most cMJ-PES studies of NPs in liquid focus on aqueous solutions, and it is worth noting that all studies involving NPs or nanocrystals (NCs) are conducted using polar solvents like water. [60].

MHP NCs studies in evolving microjet were carried out at the FlexPES beamline [61], at the Swedish national synchrotron radiation laboratory MAX IV. Unfortunately, I could not participate (because of the pandemic's restrictions) in the Perovskite XPS beamtime. All in all, I had the chance to visit the FlexPES beamline (as well as DESY/Petra III - Germany) on multiple occasions when I was in an interchange at Uppsala University - Sweden, which has allowed me to develop a comprehensive understanding of its cutting-edge experimental setup, particularly focusing on the microjet configuration.

This experience has equipped me with a comprehensive understanding of the intricacies involved in sample handling and data acquisition using the microjet technique. However, I attended the online meeting to discuss the steps, methodologies, and parameters employed during the MHP NCs experiments.

The FlexPES microjet setup scheme is displayed in Fig. 4.3. The experimental procedure comprises a series of steps. Firstly, an HPLC pump introduces a solution containing colloidal-phased MHP NCs into the vacuum chamber. The sample is then propelled through a cylindrical nozzle with a 25-15 micrometer opening, producing a jet. The jet surface is free from turbulence during the first 3 to 5 mm. This micro-jet interacts with an X-ray beam along the 3-5 mm region and subsequently collides with a liquid nitrogen trap strategically positioned to prevent contamination from reaching the pumps by condensing vapor and liquid. The ejected electrons from the jet proceed through the differential pumping nozzle and enter the electron analyzer, where photoelectrons are sorted based on their kinetic energy. The acquired spectra are carefully recorded for further analysis. The system integrates a turbo molecular pump with a pumping speed of 1000 l/s to maintain the analyzer pressure at approximately  $10^{-6}$  mbar. Furthermore, an ice breaker mechanism has been integrated into the setup to avoid freezing the entire jet and the growth of ice needles caused by the LN2 trap, which could otherwise result in signal loss from the sample. The samples were kept between 2-8 Celsius.

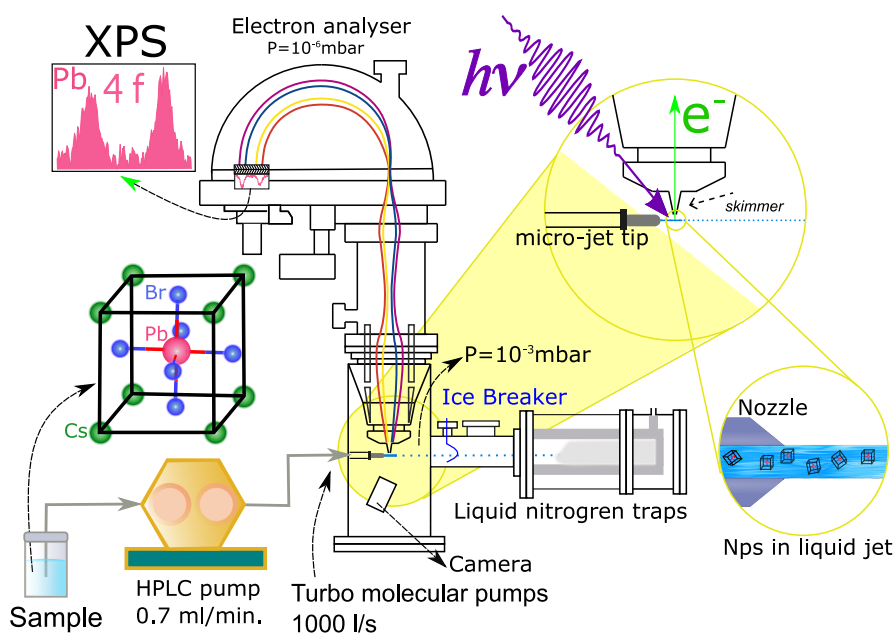


Figure 4.3: The cMJPEs setup description follows from the bottom-left to up-right. The solution the colloidal-phased MPH NCs are inserted through an HPLC pump straight into the vacuum chamber, where a cylindrical nozzle with a 15-25  $\mu$  m opening pushes the sample to form a jet. First, this micro-jet comes across with the X-ray beam. Second, the micro-jet strikes the liquid nitrogen trap, which condenses the vapor as well as the liquid, avoiding contamination getting into the pumps. After passing through the differential pumping nozzle, the photo-electrons are spatially separated according to their Kinetic Energy.

The FlexPES beamline is thoroughly described elsewhere [61]. In short, the FlexPES beamline has two branches: Surface and Material Science and the Low-Density Matter Branche (LDMB). In the LDMB, the photoemission ending station provides a microjet setup where one may perform electron spectroscopy. In our experiment, the photon energy resolution was  $\approx 0.17$  eV FWHM, and the X-ray spot size was  $\approx 65 \times 120 \mu$  m (FWHM H  $\times$  V), corresponding to a 60  $\mu$  m beamline exit slit. The photoelectron spectrometer was operated with 200 eV pass energy, giving a  $\approx 0.25$  eV resolution<sup>2</sup>. For the MHP NCs investigation, a cylindrical 24  $\mu$  m diameter nozzle was used. The micro-jet flow was 0.6 ml/min, and a High-Performance Liquid Chromatography (HPLC) pump was used to maintain a  $\approx 5$  mm laminar-flow liquid jet. FlexPES delivers linearly horizontally polarized X-rays from 43 to 1500 eV. It is compatible with electron spectroscopy studies of low-density samples using a Scienta R4000 electron analyzer connected to a micro-jet set-up. The nano-particle-containing samples were introduced using an injection loop to prevent any possibility of precipitation within the HPLC pump. The pressure in the main chamber where the spectrometer is mounted was around  $\approx 2 \times 10^{-5}$  mbar mainly caused by the hexane-toluene solvents. A photon energy lower than 400 eV yielded insufficient signal from the core levels, meaning the NCs are further away from the vacuum-liquid interface than the photoelectron

<sup>2</sup>To calculate the final resolution, we combine the spectrometer contribution (0.25 eV) and photon bandwidth (0.15 eV). The final resolution is determined by taking the square root of the sum of the squares of the individual resolutions, which in this case is approximately 290 meV.

mean free path at these conditions. Based on the parameters of the micro-jet experiments, we can determine critical conditions relevant to evaluating the status of contamination-free and the absence of radiation damage. The sample is only exposed to X-rays for 3.2 microseconds when an X-ray beam with  $160 \mu\text{size}^3$  (for his configuration it was recorded therefore the solvent feature in the gas-phase). A microjet speed of 50 m/s is used. Assuming the jet moves 2 mm until it reaches the X-ray and that one monolayer is formed at a surface at a pressure of  $1 \times 10^{-6}$  mbar, then  $8.00 \times 10^{-4}$  layers are formed in the micro-jet. This is equivalent to one second of surface exposure at a pressure of  $8 \times 10^{-10}$  in the chamber. Consequently, liquid surface contamination is ruled out in these types of measurements.

Radiation-induced oxidation is not a concern either in micro-jet experiments. One can verify it by calculating sample interaction time with the X-ray beam. The micro-jet moves at 50 m/s, and the X-ray dimension in the horizontal direction at FlexPES is 65 ( $\mu\text{m}$ ). This means the sample is exposed to X-ray only 1.3  $\mu\text{s}$ . Considering a minimum time of X-ray exposure of the solid sample of one second for a measurement, we immediately conclude that the solid samples are exposed to about one million times more radiation. Measurements in solid samples take longer, meaning our calculation is conservative.

The synthesis of amine-free CsPbBr<sub>3</sub> NCs was carried out using a hot injection protocol developed by Yassitepe [48]. The Cs- and Pb-oleate precursors were solubilized in a high boiling point solvent (1-octadecene) and were injected with the bromide precursor (TOABr) to form a greenish dispersion of CsPbBr<sub>3</sub> PNCs. The NCs were then purified by precipitation and redispersed in anhydrous hexane. Oleylammonium-capped CsPbBr<sub>3</sub> PNCs were synthesized using a hot injection method described by Protesescu's work [17]. The PbBr<sub>2</sub> salt was dissolved in 1-octadecene using oleic acid and oleylamine, and Cs-oleate precursor was swiftly injected into the solution to form a greenish dispersion of CsPbBr<sub>3</sub> NCs. The OLA/OA-capped PNCs were purified by centrifugation and redispersed in anhydrous Hexane for further analysis. A quaternary salt (TOABr) was added to make the sample conductive, but adding 50 mM of quaternary salt did not produce the desired effect and resulted in an energy shift of the XPS peaks with no clear broadening effect. To circumvent the HPLC pump's instability during the measurements, toluene was added to the sample in a proportion of 1:1 by volume. The NCs were dispersed in a nonpolar solvent mixture of hexane and toluene in a 1:1 volume ratio.

### 4.3 The MHPs Nanocrystals Core-Level Analysis

All the spectra were fitted using the IGOR PRO software (v. 6.37) [62]. In fitting the Pb, Br, and Cs spectra, the lifetime broadening and instrumental broadening were accounted for using a Voigt profile (corresponding a Lorentzian convoluted with a Gaussian [63]. We ob-

---

<sup>3</sup>The Beam focus and spatial resolution of the beamline is FWHM from 50 x 15  $\mu\text{m}$  (focussed beam) to 1000 x 400  $\mu\text{m}$  (defocussed beam)

tained the Lorentzian widths from the literature [64], and the Gaussian widths were kept as free parameters. We used a special package called SPANCF [65] inside the IGOR PRO data analysis program for all our fittings. In Fig.4.4 the calibrated spectra for Pb, Cs, and Br core levels in OLA and AF cases used in the analysis are presented. To check the calibration procedures employed in these spectra, please check Appendix A.1 for more details. The core spectra belonging to the two samples were normalized using the Pb  $4f_{7/2}$  peak, which shows an unchanged profile (the upper images in Fig. 4.5) between the two analyzed samples. This normalization choice is grounded on their topology and bonding scheme, consistent with the lack of Pb substitution reported in the literature. We used a beam of 600 eV to ionize the Pb 4f, Br 3d, and Cs 4d core levels.

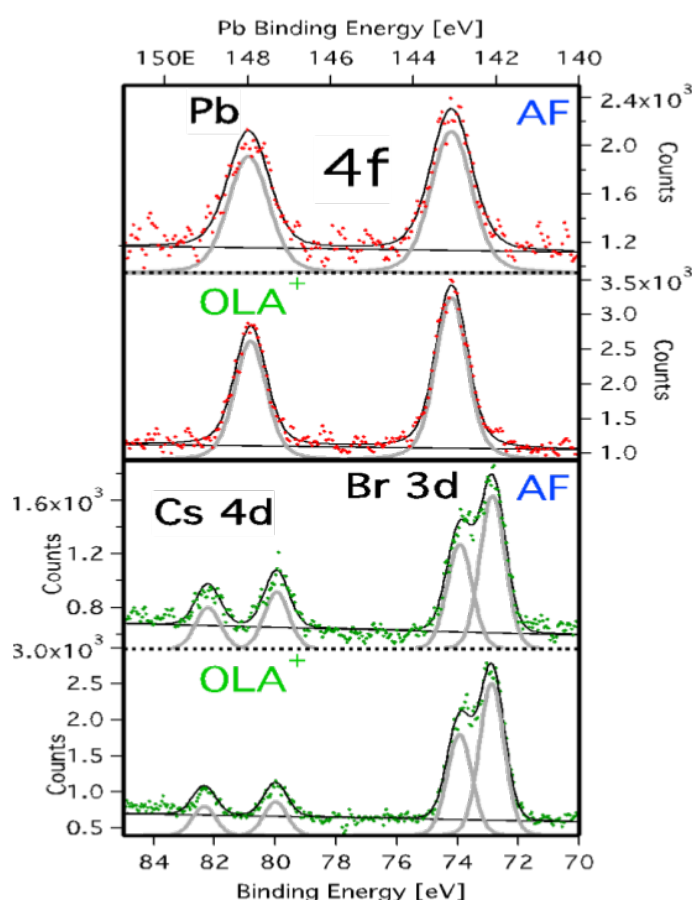


Figure 4.4: The calibrated spectra of Perovskite core level using the process described in Appendix A.1. In the first two spectra, the experimental data of Pb 4f electron peaks (split due to spin-orbit coupling) are depicted with red dots. The upper spectrum corresponds to the Amine-Free (AF) case, and the second spectrum represents the Oleylamine-capped ( $\text{OLA}^+$ ) case, with the binding energy axis placed at the top. The last two spectra display the Cs 4d (on the left) and Br 3d (on the right) electron peaks, once more for the Amine-Free sample, shown as green dots, with the binding energy axis at the bottom.

Inspecting the ratio between the Pb from both synthesis methods, we found a normalization factor 0.53 in the spectra between the two samples. (shown in the Fig4.5 a). We conclude that the absolute intensities of the XPS are consistent with the fact that the two types of NCs are buried at different average distances from the vacuum-liquid interface. We energy-shifted and aligned all the spectra to help their intensity comparison. No significant

difference between the samples was found for the Pb 4f<sub>5/2</sub> and Pb 4f<sub>7/2</sub> signals. In Fig. 4.5 b), the Br 3d peaks also show no change in the intensity between the two methods, meaning that no Pb substitution implies no Br substitution as well, sample-wise. The previous solid-state Br 3d spectra in Ravi et al. [4]) show shifted doublet peaks at higher binding energy. As pointed out by the authors, the contribution from the higher binding energy species (HBES) decreases as the photon energy increases. At 2500 eV, the HBES corresponds to about 50% of the lower binding energy species. It was correctly interpreted that the HBES is a signature of Br atoms belonging to the NC surface. Following this assignment, one would expect an even stronger signal from the HBES at 600 eV (or 650 eV) photon excitation.

Our Br 3d spectra cannot accommodate the existence of two chemically distinct Br species. Furthermore, the study performed in vacuum NCs shows no indication of a separate species, as suggested by Milosav et al. [39]. Our resolution indicates that the pristine NCs exhibit no chemically shifted species belonging to the surface and the bulk. We conclude that the surface oxidized Br species in the solid-state study may explain this inconsistency. These findings underscore the contamination-free nature of the present cMJ-PES probing method. We have conducted XPS spectroscopy of solid samples to elucidate this inconsistency in the last chapter. Our analysis indicates that Br radiation-induced oxidation is responsible for the HBES features in the solid sample.

In contrast to the Pb and Br spectral features, the Cs 4d peak is substantially reduced in the OLA<sup>+</sup> synthesis spectrum (Fig. 4.5b). We explain this reduction due to substituting the Cs atoms mechanism for the OLA<sup>+</sup> bonding to the NCs. The histogram in Fig. 4.5c makes it possible to see the signal difference of Cs between the two methods. OLA<sup>+</sup> has a 50 ± 10% lower Cs signal than AF Ncs. To determine the extent of Cesium substitution, it is necessary to identify the layers from which a certain amount of photoelectron signal originates.

To answer these questions, one can refer to the theoretical solvated NC and electron attenuation models exhibited in more detail in Appendix B (this model had experimental support from TEM and X-ray diffraction results described in more detail in the next section). The immediate implication of this model is that we found the electron attenuation length from the NC surface toward its core. We could use this factor and our derived surface substitution formulas to calculate the number of atoms substituted in the NC surface from the experimentally obtained Pb/Cs and Br/Cs ratios. In the text, we defined  $\alpha = \exp\{-5/2\text{ELA} \cdot n_0\}$ . This formula incorporates parameters related to the mean free path of photoelectrons (ELA), solvent properties ( $n_{sol}^0$ ), and the structure of CsPbBr<sub>3</sub> nanocrystals.

Fig. 4.5c shows a minor variation change for the *total* Pb 4f signal (4f<sub>7/2</sub> + 4f<sub>5/2</sub>) within the error bar (see Appendix AI to understand more about the error analysis). The relative dissimilarity in the Pb 4f signal is related to the 4f<sub>5/2</sub> feature (see Fig. 4.5a again). This observation might be attributed to decay processes that involve the VB. Depending on the synthesis method, the width in the Pb 4f<sub>5/2</sub> peak lines might change. A possible explanation

is that new decay channels may open for the 5/2 ionic state compared to the 7/2. A future study with a substantially higher statistical is required to verify whether this peak width divergence is authentic.

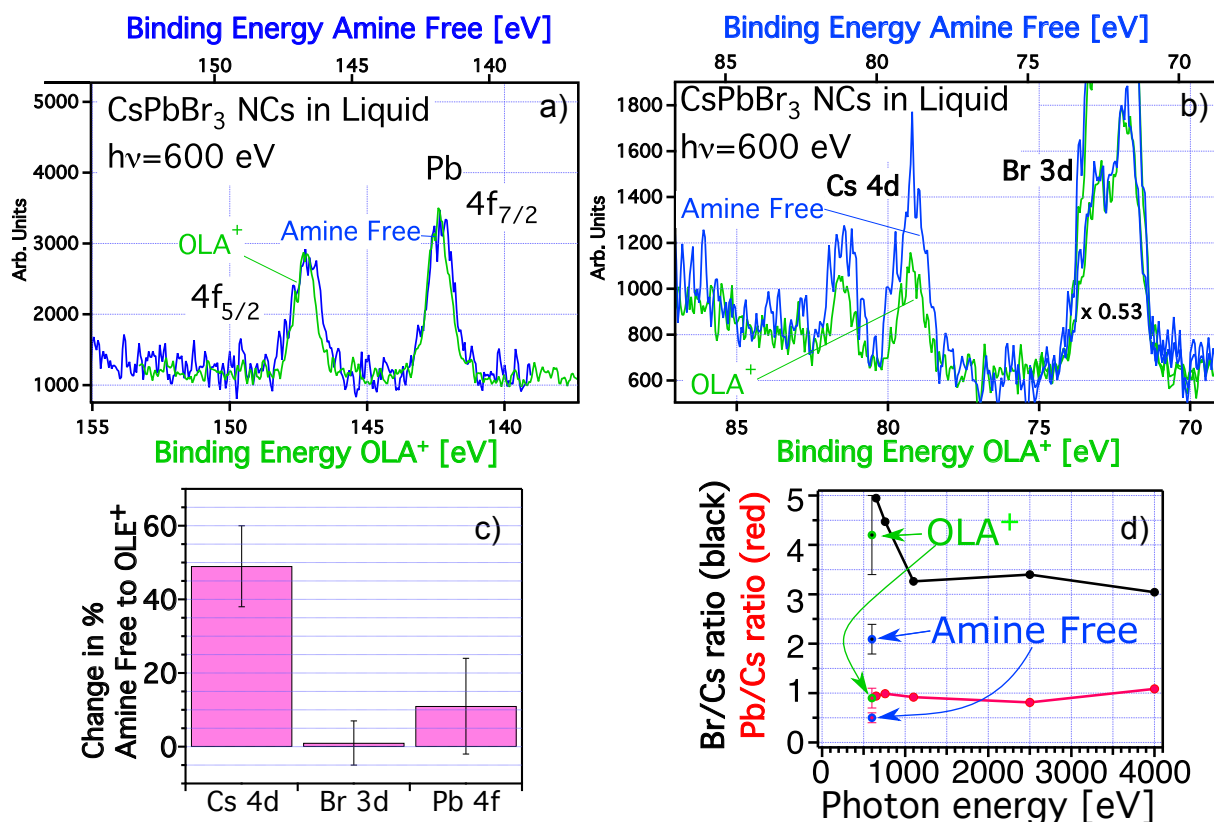


Figure 4.5: The spectra are normalized according to the Pb 4f<sub>7/2</sub> peak, and the error bars were obtained from the process described in Appendix A.2. In b) the Br 3d peaks show no change in the intensity between the two methods. This constancy agrees with what is observed for the Pb 4f peaks in a). In contrast, the Cs 4d peak is substantially reduced in the OLA<sup>+</sup> synthesis spectrum. We propose the substitution of Cs atoms by OLA<sup>+</sup> as a mechanism for the OLA<sup>+</sup> bonding to the NCs. The NCs are diluted in toluene + hexane 1:1 volume. 5% per weight. d) Br/Cs (black) and Pb/Cs (red) ratios for both amine-free (blue points - indicate results from this work) and OLA<sup>+</sup> samples (green points - indicate results from this work), with photon energy 600 eV. The measurements linked by the continuous lines (without error bars) were reported by Ravi *et al.* [4].

Another question: Is there any Cs substitution in the amine-free synthesis? To discuss this question, we turn to Fig. 4.5d, which shows the Br/Cs and Pb/Cs ratios as observed in the XPS intensities that were recorded using 600 eV photons (Fig. 4.5a and 4.5b). Also plotted in Fig. 4.5d is data reproduction from Ravi *et al.* [4], who only studied NCs synthesized by the OLA<sup>+</sup> method. Here, their experimental data is connected by a solid line, and all their data have no error bars. At 600 eV, our results reproduce theirs (measured at slightly higher photon energy - 650eV) within our uncertainties. The Br/Cs significant ratio reduction from about 5 to 3 as the photon energy increases to 1 keV is interpreted as a consequence of the detected photoelectrons at ~600 eV representing primarily surface electrons. In contrast, the photoelectrons detected for  $h\nu > 1$  keV are mainly representative of the bulk.

We observe striking changes in both ratios for the amine-free NCs at 600 eV. The amine-free sample's Br/Cs and Pb/Cs ratio is 2.1 and 0.5, respectively, where we corrected all intensities by the photoionization atomic cross sections [66]. We inserted this ratio in equations B.12 and B.13. we conclude from the equation that if  $\alpha$  is 0.5, the experimental ratio is consistent with no Cs substitution or Br substitution on the amine-free NCs. We have used Molecular Dynamics (MD) simulations and the results from transmission electron microscopy and X-ray diffraction to evaluate the crystals that have the lowest energy. According to the calculations, the MPH NCs have six faces terminated by CSBr. For the MHP OLA<sup>+</sup>, inserting Br/Cs and Pb/Cs experimental ratio is 4.2 and 0.9 in equations B.12 and B.13, we obtain 60% Cs substitution in the NCs surface and no Br substitution.

## 4.4 Complementary Characterization

The analysis of CsPbBr<sub>3</sub> nanocrystals, particularly their morphology, size, and absorption spectra, provides valuable insights into their quantum confinement regime and structural characteristics [67, 68]. The absorption spectra of these nanocrystals offer information on the thickness of the particles, indicating the presence of nanocubes with a size larger than the exciton Bohr radius for the case of amine-free Perovskite. As depicted in Figure 4.6, it is possible to observe that, for AF CsPbBr<sub>3</sub> PNCs, the shape presented by their absorbance spectrum indicates a majority of nanocubes with size larger than 7 nm (i.e., the exciton Bohr radius for CsPbBr<sub>3</sub> perovskite).

On the other hand, the absorption spectrum presented by OLA-capped CsPbBr<sub>3</sub> PNCs, also depicted in Figure 4.6, exhibits an absorption onset at lower wavelengths in comparison with the AF ones, also including a sharp excitonic peak around 450 nm, which indicates the presence of perovskite nanoplates thinner than 7 nm. The interpretations proposed for the absorption spectra presented by the two samples are supported by the size distribution analysis on the TEM micrographs for both samples. For the AF CsPbBr<sub>3</sub> sample, TEM images (Figure 4.7 on the right hand) reveal a nanocube morphology with an average size distribution of  $12.0 \pm 3.5$  nm (Figure 4.8 the green histogram). In the case of the OLA-capped CsPbBr<sub>3</sub> sample, TEM images (Figure 4.7 on the left hand) reveal a nanoplate morphology with a thickness distribution centered in 6 monolayers, i.e., 3.54 nm for each monolayer yields a distribution center in around 18 nm (Figure 4.8 the blue histogram). Additionally, the XRD diffractograms depicted in Figure 4.9 are from both samples.

The XRD spectrum from both synthesis methods provides valuable insights into their crystallographic structure. The AF intensities exhibit peaks for the [110] direction at  $2\theta = 15^\circ$ ; for [200]  $2\theta = 21^\circ$  and [220]  $2\theta = 30^\circ$ , suggests a strong presence of the crystal lattice planes corresponding to these directions. One can observe also peaks with lower intensity (compared to the other three) around  $2\theta \approx 34.8^\circ$ ,  $35.5^\circ$  and  $43.8^\circ$  indicate additional crystallographic features. For the OLA case, the [110] direction, evidenced by the peak at two theta

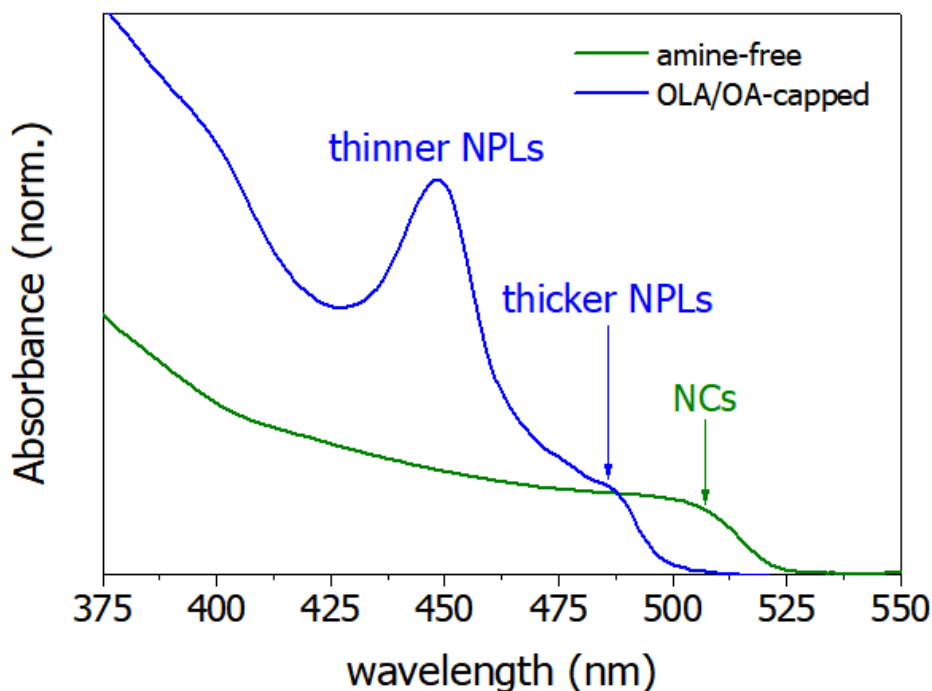


Figure 4.6: Visible-Ultra-violet absorption spectra, the sample size influences intensity and shape. As seen in the spectra above, thick samples deliver absorption spectra in the visible-ultraviolet range, tending to have well-defined peaks corresponding to electronic transitions. However, in thin samples, such as thin films or nanoplates, quantum confinement effects can cause the absorption bands to broaden and shift to higher energy (shorter wavelength). This shift is due to the limited number of available energy states and the confinement of charge carriers within the reduced dimensions of the thin sample.

=  $15^\circ$ , exhibits a feature that now is half of the [220] direction indicating a potential alteration in the atomic arrangement along this axis when compared to AF. In the [220] direction, which had an intensity of 16 at two theta =  $30^\circ$  in the previous spectrum, remains prominent and unchanged, indicative of a stable crystalline orientation. XRD results characterize crystallographic properties for the orthorhombic Perovskite phase (pnma point group) [69, 70].

In Fig. 4.10a some NCs show interlayer distances of about 0.28 nm, which is compatible with the [001] direction of the optimized bulk. Figure 4.10c displays an image of a representative NC of size  $\approx 11$  nm, obtained for the amine-free sample, where some values of the interlayer distances can be extracted. On the other hand, the observed distance between consecutive minima along the yellow direction (indicated in Fig. 4.10c) is 0.41 nm, which is in good agreement with the optimized [020] interlayer distance of 0.42 nm (Fig. 4.10d). Next, comparisons between the Appendix B model and the TEM images reveal essential information about the terminations.

In brief, the theoretical calculation looks up to the surface energies of the NCs and it came out the lower surface energies are for the [001] and [110] which are CsBr terminations. It was supported by a report where it is well understood that the [001]CsBr Perovskite terminations are the most stable ones [4, 71]. Furthermore, the next step was to find what is the contribution from the first layer where now it is set off to be CsBr. Resorting to Appendix

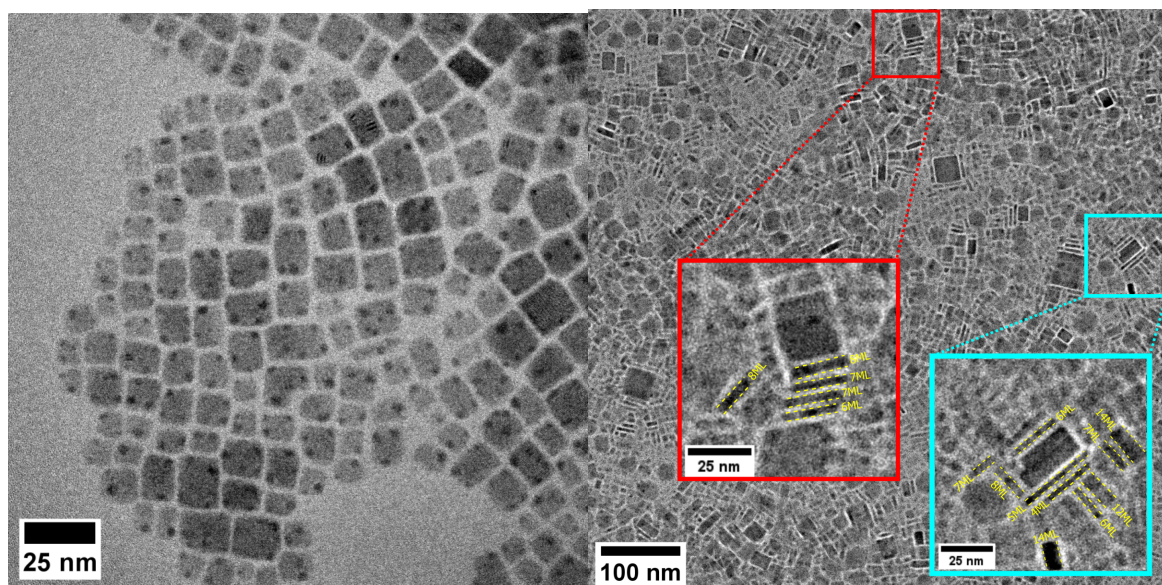


Figure 4.7: Transmission electron microscopy (TEM) images illustrating the morphology and size distribution of the CsPbBr<sub>3</sub> nanocubes in the AF and OLA samples. (a) The nanocube morphology with an average size of  $12.0 \pm 3.5$  nm is observed for AF. (b) The nanocube, along with nanoplate morphology, where these nanoplates were found to be monolayers (ML).

section B.1.1, it is defined an equation containing an analysis of the electron length attenuation. After manipulation of this equation, one ends up with a general relation for the XPS signal attenuation for the NC Perovskite independent of the solvent presence on the surface. This general equation takes up a crystal with a termination with a PbBr<sub>3</sub> and CsBr mixture termination as well as a term for Cs and Br substitutions. The keystone of the theoretical model is placed in equations B.8 and B.9 they define an attenuation factor for a crystal with 6 CsBr-termination and no substitution for Cs and Br. The outcome is that Pb/Cs is given by the attenuation factor ( $\alpha$ ). When compared to the AF ratio, one can deduce that the XPS attenuation for the first layer is half of the total signal since the Pb/Cs = 0.5. Hence, recalling the elementary ratios, the Br/Cs signal from the first layer in the Amine-Free is 1 implying the surface has a one-to-one relation for Cs and Br. Finally, we can define what is the Cs substitution amount in the OLA for AF. As half of the XPS signal comes from the NCs surface than in Fig. 4.5c the histogram shows AF has roughly 60% more Cs.

On the experimental side, according to TEM image, for the [010]-direction (yellow line on Fig 4.10c), the angle of 45° with the terminations supports the idea of the non-polar [110] surfaces. So it is likely that the other terminations are the stable [110]CsBr and/or [110]PbBr<sub>2</sub> ones (Fig. 4.10b). In addition, it is worth noting that there are no [100] and [010] layers respecting the charge neutrality. For the OLA<sup>+</sup> sample, the TEM images (Fig.4.7) also characterize the morphology distribution of the NCs. The image shows pseudocubic particles with sizes ranging from 4 nm to 38 nm.

Therefore, analyzing the core-level XPS applied on microjet with an NP Perovskite and Hexane/Toluene solvent brings more accurate insight into their surface chemical dy-

---

namics. This approach allows less radiation-damage exposure, which permits us to compare the surface stability between the two synthesis methods (OLA and AF), reporting that the absence of OLA in the Perovskite manufacturing process produces crystal without protonation. Also, along with TEM, XRD, and MD calculations, we were able to bring out that OLA  $60 \pm 10\%$  less Cesium in the surface than AF.

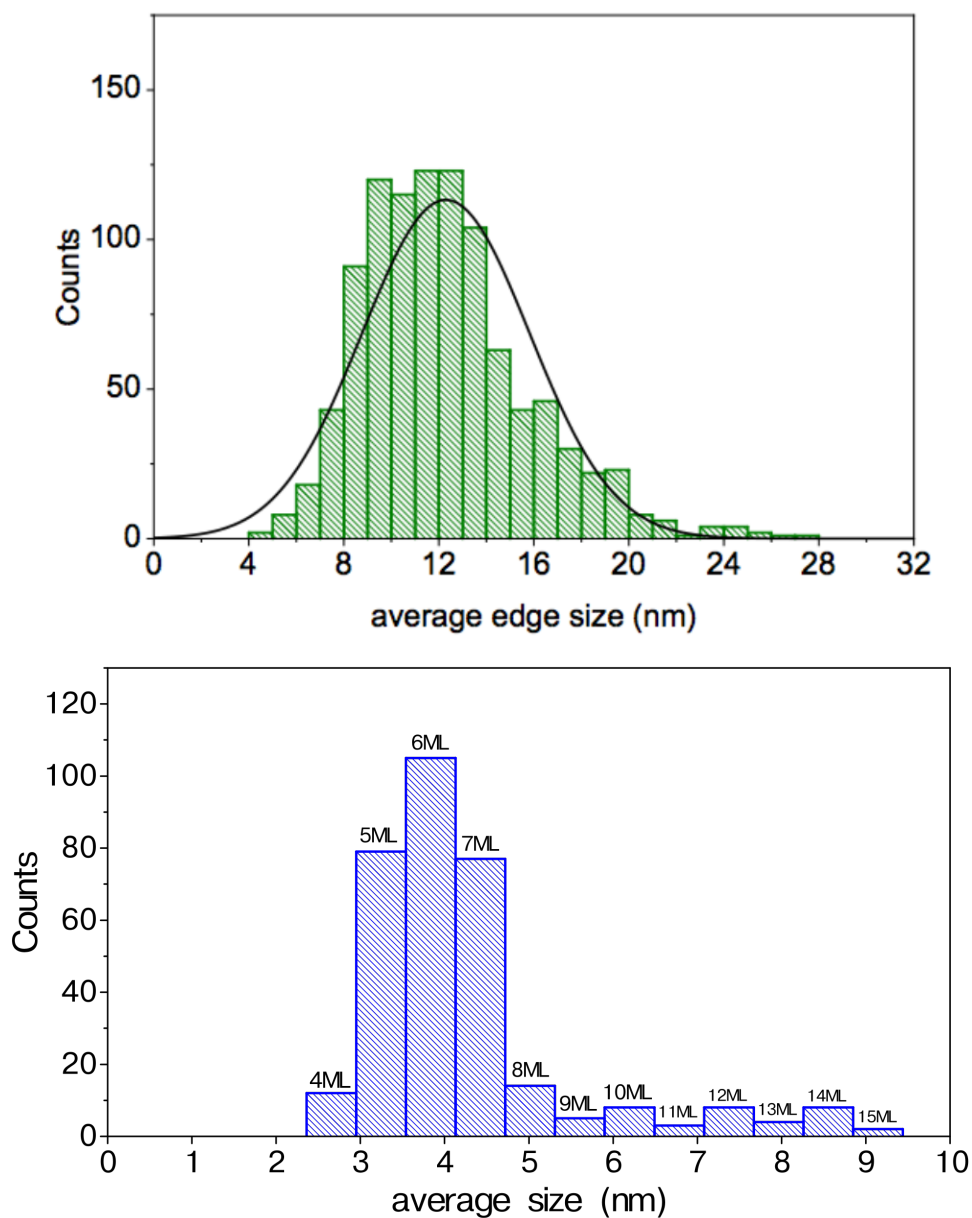


Figure 4.8: Lateral size distribution for the AF CsPbBr<sub>3</sub> NCs, a histogram showing an average size distribution of  $12.0 \pm 3.5$  nm, with intervals of 1 nm ranging from 4 to 28 nm. In addition, the thickness distribution for the OLA-capped CsPbBr<sub>3</sub> NC nanoplates was found centered in 6 monolayers corresponding to a 3.54 nm.

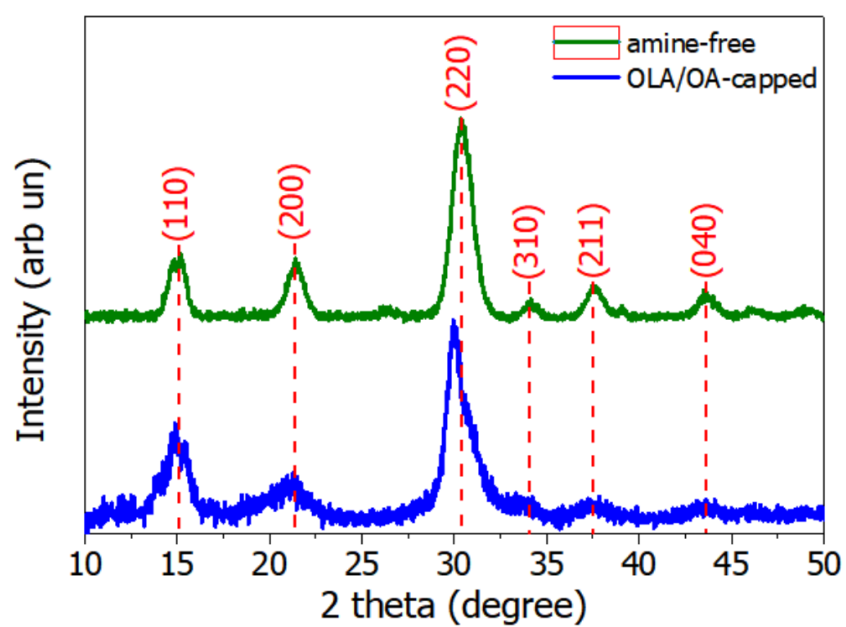


Figure 4.9: X-ray Diffraction spectra of AF and OLA-capped CsPbBr<sub>3</sub> PNCs.

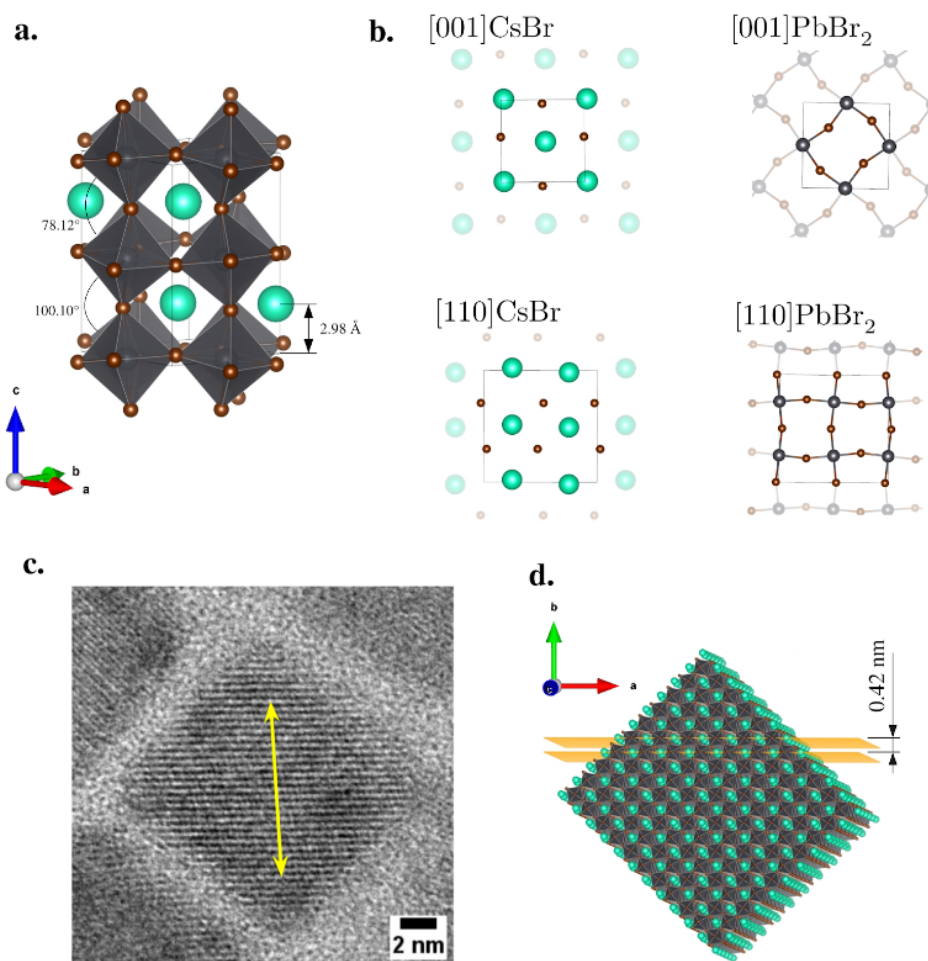


Figure 4.10: a. Unit cell of the orthorhombic phase of the  $CsPbBr_3$  Perovskites. The atoms are Cs (green), Pb (gray), and Br (brown). The optimized tilting angles of the Pb-Br octahedra and the [001] interlayer distance are indicated. b. Scheme of all CsBr and PbBr<sub>2</sub> terminations considered. c. TEM image of an NC, obtained within the Amine-free method. d. NC model.

## 5 MHP'S VALANCE BAND APPLYING MICROJET APPROACH

---

This final part of my PhD efforts aims to study the Valence Band (VB) characteristics when the MHP nanocrystals are subjected to liquid surroundings. What is the relevance of studying this aspect of the MHPs' electronic structure? VB is crucial in semiconductors and Perovskites, as it encloses the energy range of electron states responsible for bonding and electrical properties [72,73]. The valence band's characteristics determine the material's behavior in conducting electricity. In intrinsic semiconductors, the valence band is fully occupied, and a notable energy gap exists between the valence and conduction bands, where no electrons are present. However, external influences like doping can change the valence band energetics, allowing electrons to populate the conduction band, generating charge carriers, and enabling current flow via the application of electric fields. Here, we focus on studying the dispersion of nanocrystals in a colloidal phase. The liquid environment can impact the band gap through secondary effects, such as surface modifications or chemical reactions [74]. Moreover, nanoscale particles have a significantly larger surface area to volume ratio ( $>10^7:1$ ) compared to macro-sized particles [75,76]. As the surface area to volume ratio increases, more atoms are located at the surface, making the surface effects more dominant. Thus, the NCs interface with different materials can vary the effective band gap.

The interaction of nanocrystals with gases, liquids, or other materials at their surface can result in surface modifications, adsorption of molecules, and formation of surface states [77]. Thus, monitoring the possible solvent influence in the VB signal is good. XPS, or ultra-violet photoelectron spectroscopy (UPS), is well-known for probing occupied orbitals. In contrast, the unoccupied valence orbitals are traditionally probed by X-ray or UV/visible light absorption spectroscopy. There are, however, many other possibilities to probe the unoccupied orbitals, which are less known but useful. Shape-up transitions upon core ionization, also known as XPS satellites, is one of these techniques. Upon ionization of a core electron, a second electron may excite from the occupied valence band to an unoccupied one. Consequently, if we measure the energy and intensity of the lowest shake-up satellite to the core line, we obtain the band gap information of the ionic species and information about the overlap between the electronic distribution between the valence-occupied and unoccupied states.

In XPS spectra, satellite peak results from factors like the absence of a monochromatic beam, plasmon losses, and interactions between core and valence electrons. Understanding their origins is crucial for accurate data interpretation. Synchrotron radiation is highly monochromatic, which reduces the occurrence of satellite peaks compared to con-

ventional X-ray sources, see Chapter 2. Alternatively, Plasmon loss peaks can still be observed in synchrotron spectra. Plasmons are collective oscillations of electrons in a material, and when excited by X-rays, they can result in energy loss peaks in the spectrum [78]. These plasmon loss peaks provide valuable information about the electronic structure and properties of the material being studied. Although they can emerge in XPS spectra, they were not interesting to our study. The only effect left is the previously discussed electron discrete excitations.

## 5.1 The Valence Band in Solid/Aqueous Interface

The solid/aqueous interface is significant in materials science and electrochemistry, crucial for energy conversion applications, corrosion protection, and catalysis [79, 80]. A comprehensive understanding of the electronic structure at this interface is essential, especially regarding the valence band, which encloses the highest occupied molecular orbital (HOMO), also known as the valence band maximum (VBM). One of our objectives is to investigate and provide insights into the solvents' VB to uncover its electronic structure and surface reactivity with the NCs. The outcomes of this research may contribute to the advancement and optimization of novel materials and strategies for nanomaterials in colloidal manufacturing processes. For instance, in [81], the solid-liquid interface significantly impacts reduction reactions and coordination network formation involving copper ions. Ligand coordination is restricted at the interface, leading to distinct reactivity. The restricted approach enhances Cu(II) reduction and enables the formation of coordination networks.

The investigation of valence band properties and solvent-induced effects involves the employment of diverse experimental techniques. Notably, XPS (it has already been vastly described here), X-ray absorption spectroscopy (XAS), and scanning probe microscopy (SPM) are employed for the characterization and analysis of these properties. Photoelectron spectroscopy enables the direct measurement of the kinetic energy and intensity of photoemitted electrons, providing valuable information about the electronic structure and energy levels within the valence band.

XAS, alternatively, probes the interaction between X-rays and the nano semiconductors, offering insights into the electronic and geometric structure. By analyzing the X-ray absorption near-edge structure (XANES) and extended X-ray absorption fine structure (EXAFS), information about the unoccupied states, local coordination environment, and electronic transitions within the valence band can be obtained. This technique contributes to the comprehensive characterization of the valence band properties and the influence of the solvent environment.

Furthermore, scanning probe microscopy techniques, including atomic force microscopy (AFM) and scanning tunnelling microscopy (STM), provide high-resolution surface imaging and mapping of the nano semiconductors. These techniques offer the capability to

investigate the surface morphology, topography, and local electronic properties, facilitating the examination of solvent-induced effects on the valence band.

In situ, X-ray Photoelectron Spectroscopy (XPS) offers unique capabilities in elucidating the valence band structure of Perovskite materials in liquid/solid interfaces. With its inherent surface sensitivity and broad energy range, XPS provides valuable insights into the surface's electronic structure and chemical composition. Sub-monolayer electronic structure information can be easily detected, allowing for precise surface chemistry analysis. However, there are certain limitations to consider. XPS cannot provide phase information of surface chemical species, as variations in crystal structure do not induce significant shifts in core levels. On the other hand, the valence band is sensitive to changes in neighbouring atom arrangement, making it a potential probe for surface phase composition. Nevertheless, accurately determining surface phase composition within a 10 nm range presents significant challenges [82, 83].

## 5.2 Solvent Features: Valence Band Spectra and Satellite Effects

Toluene liquid UPS shows a significant shift

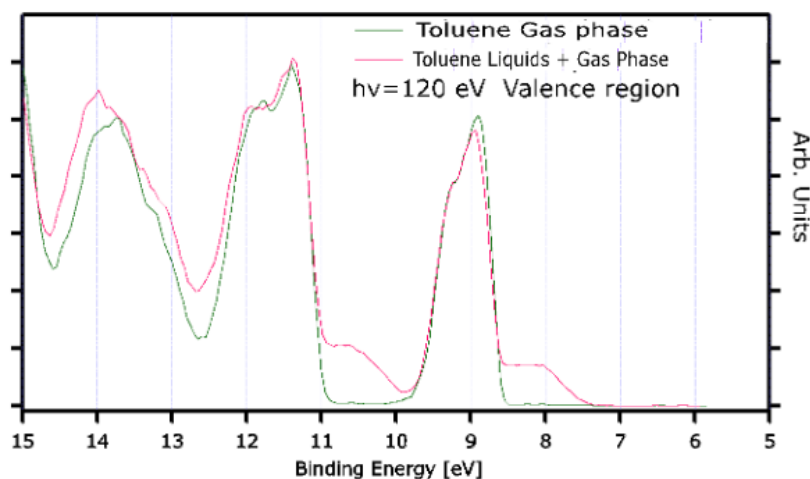


Figure 5.1: The green spectrum shows the toluene gas phase, while the red spectrum shows the toluene plus liquid. It is notable to identify the liquid and gas phase contributions and the upper feature is placed below 7 eV.

The valence band spectra shown here are from NCs created using the OLA<sup>+</sup> method and diluted in a mixture of Hexane and Toluene to study two different MHP NCs, one containing Br and another I. The measurements were performed during the same XPS MHP NC beamtime. Before analyzing the perovskite VB, we need to calibrate it using the solvent VB. Furthermore, the gas and liquid phase spectra from both solvents must be assigned in detail to identify the remaining features of the MHP NCs. There are two solvents, Toluene

and Hexane. The hexane gas phase and liquid plus gas have recently been calibrated in ref. [39]. This information will be used for our MHP NCs calibration.

## Calibration and Blank solutions

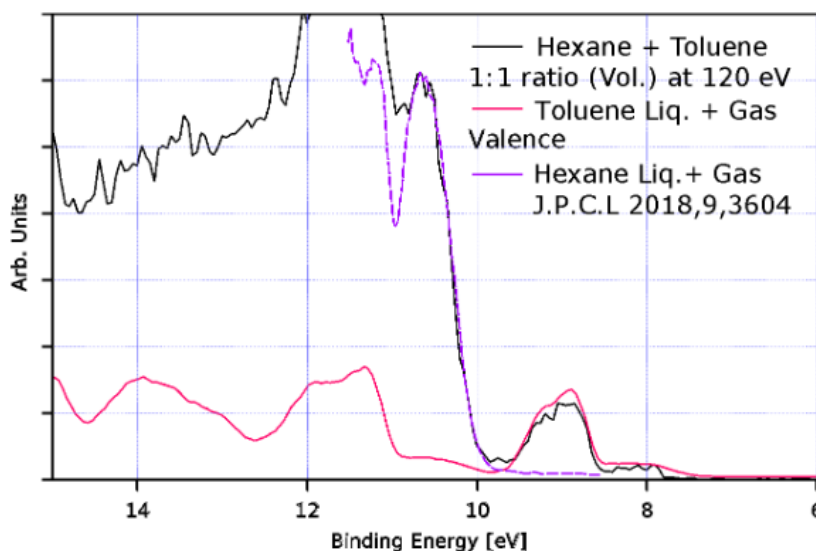


Figure 5.2: The black solid line represents the valence band spectra of the Hexane + Toluene mixture in liquid + gas phase. The red curve represents Toluene liquid + gas features. The lowest contribution in the valence band ranges from 9.6 to 7.3 eV.

We have conducted a valence spectrum analysis of the toluene gas and liquid + gas phases to distinguish liquid features from the spectra. Our findings show that the occupied states in the liquid phase have lower binding energy than the gas phase. This is because, in the liquid state, the charge of the ion produced by photoelectron ejection is partially shielded by the surrounding molecules, resulting in reduced Coulomb attraction. As a result, the remaining ion contains a smaller effective charge, reflecting a photoelectron kinetic energy increase and lowering its binding energy compared to the isolated molecule where no shielding is possible.

Fig.5.1 Upper part shows only the gas signal in green, which is slightly more intense than the liquid plus gas signal. In the liquid + gas signal, small shifted peaks correspond to the electronic states in the liquid at lower binding energy. In Fig.5.1 Lower panel, in black solid-line, the Hexane + Toluene mixture is exhibited. In red, the Toluene liquid + gas features were repeated to depict that the lowest binding energy contribution in the VB comes from the liquid toluene in a range of 9.6 to 7.3 eV. In Fig.5.3, the calibration spectra for CsPbBr<sub>3</sub> and CsPbI<sub>3</sub> aligning the Toluene and Hexane features from the blank solution over the Solvent with the MHPs. In the study, the Hexane VB area was investigated in conjunction with Toluene. The calibration spectra of CsPbBr<sub>3</sub> and CsPbI<sub>3</sub> were aligned with Toluene and Hexane features from the blank solution over the Solvent with the MHPs.

Additionally, to our knowledge, we recorded the first shake-up spectra from non-polar liquids, see Fig.5.4. The shake-up effect refers to the phenomenon where an electron

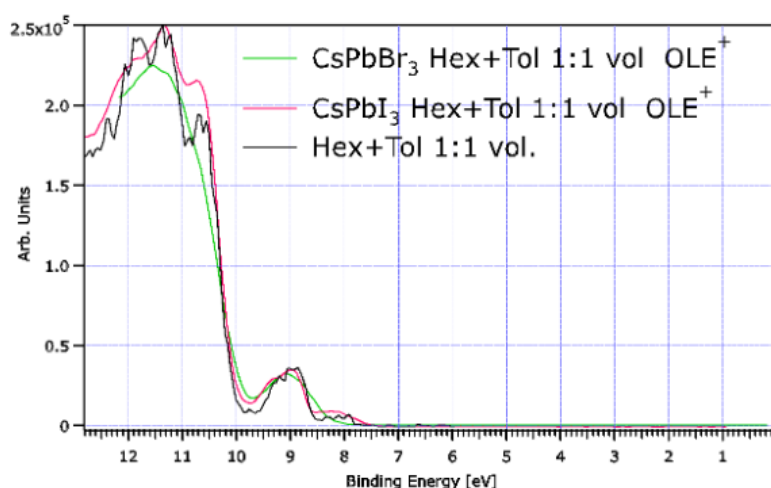


Figure 5.3: The upper figure shows calibration spectra of CsPbBr<sub>3</sub> and CsPbI<sub>3</sub> aligned with Toluene and Hexane features. The liquid Toluene's lowest contribution in the VB ranges from 9.6 to 7.3 eV, as reiterated in red in Fig.5.1. These findings demonstrate the important role of XPS spectra in studying the electronic structure of materials.

from a core level is excited to a higher energy level, leaving behind a core hole [84–86]. The valence electrons readjust to compensate for the core hole, resulting in energy transfers and additional peaks in the XPS spectra. This effect provides valuable information about the electronic structure of the analysed material. The shake-off effect is when a second electron is completely ejected from the atom due to a strong interaction with the ejected photoelectron. It is more prominent in heavier elements and higher X-ray energies.

The shake-up intensity can provide a significant understanding of the sample. Higher shake-up intensities may suggest electron-electron interactions or molecular electronic configurations. It can also indicate the presence of localized or delocalized electronic states and the degree of electron correlation in the system.

For the present study, the Toluene shake-up spectra show that (1) The C1s main-line gas phase spectra and the liquid C1s spectrum have comparable widths. Please notice that the "pure" liquid C1s spectrum was obtained by subtracting the liquid plus gas phase from the pure gas phase spectrum. This comparable width in the spectra confirms that no significant extra-broadening comes from this highly isolating liquid. (2) The shake-up satellites are enhanced in the liquid compared to the gas phase. (3) the band gap is about the same in the gas phase and liquid.

The increase in shake-up intensity may be due to photoelectron losses in the liquid phase and an increased overlap between VBM electrons and Conduction Band Minimum (CBM) orbitals in the liquid. However, the fact that the band gap is similar between the gas phase and liquid indicates that the CBM in the toluene liquid has higher energy since we already know that the VMB has lower binding energy in liquids.

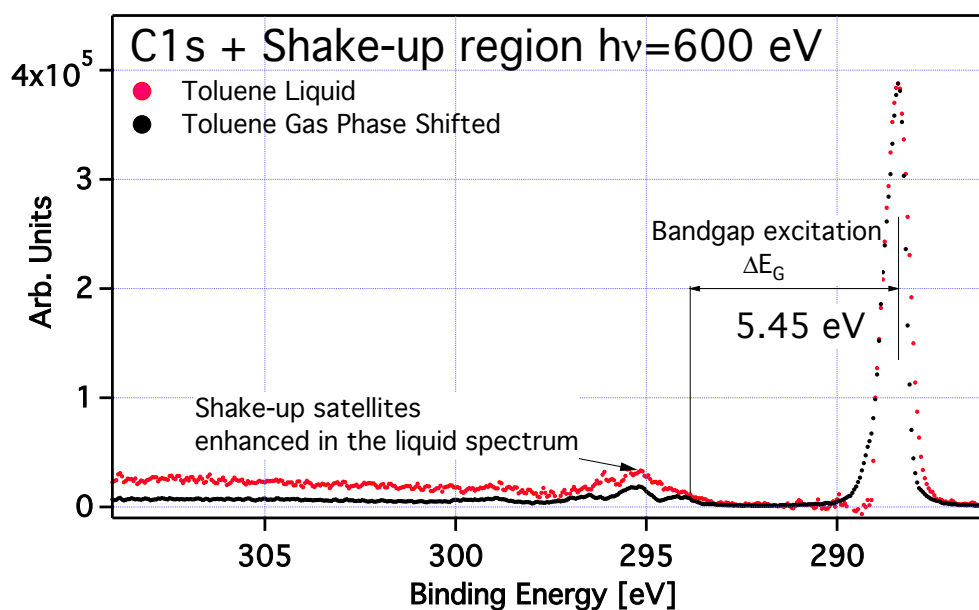


Figure 5.4: The toluene shake-up C1s spectra. This effect provides valuable insights into the electronic structure of the analyzed material. See text for more details

### 5.3 The Environment's Influence on Perovskite Electronic Properties

Synchrotron facilities offer possibilities to study the electronic properties of materials through Ultraviolet Photoelectron Spectroscopy (UPS). Researchers study the electronic structure NPs suspended in vacuum to analyze the change in their electronic structure without solvation. Recent research reported on the valence band of OLA<sup>+</sup> Perovskite suspended in vacuum and the VBM alignment to the vacuum of CH<sub>3</sub>NH<sub>3</sub>PbBr<sub>3</sub> NCs and associated ligands used in their synthesis [39].

The research in [39] examines the potential impact of ligand molecules on the observed properties of Perovskite NCs and compares their electronic characteristics to those of bulk materials. The experimental findings are further substantiated through DFT calculations. They used an aerosol spray system, which included an Ar carrier gas. The aerosols passed through a heated metallic tube, which aided the evaporation of the solvent, Hexane. The aerosol beam was then focused using an AL, so the NCs were characterized as isolated in vacuum. The investigation revealed that the valence band mainly comprises Br 4p and Pb 6s states. The Br 4p states primarily comprise the HOMO due to surface ligands masking the signal, making it challenging to determine the valence band edges from gas-phase UPS spectra. The VBM was observed at 6 eV for the small NCs (Size =  $11 \pm 3$  nm), and in the same study, they showed Blank Oleic acid and Octyamone in hexane at VBM 7.5 eV. Therefore, at the NCs VBM, there is no interference with the solvent ligands levels. Their findings demonstrated that the valence band composition remained consistent with the presence of the Br

4p states and the Pb 6s states, with no significant deviation observed compared to the bulk material, even for nanocrystals in the size range of 8-15 nm. In the study by Zhao Liu et al. ref [87], the band gap of CsPbI<sub>3</sub> was determined to be 1.763 eV through calculations. The report focuses on the simulation and analysis of the perovskite materials TIPbI<sub>3</sub> and CsPbI<sub>3</sub>. Experimental measurements of the absorption spectrum of CsPbI<sub>3</sub> were informed to yield an optical band gap value of 1.73 eV, which closely aligns with the simulated value obtained from the calculations. This agreement between the calculated and measured optical band gaps validates the accuracy and reliability of the theoretical predictions for CsPbI<sub>3</sub>.

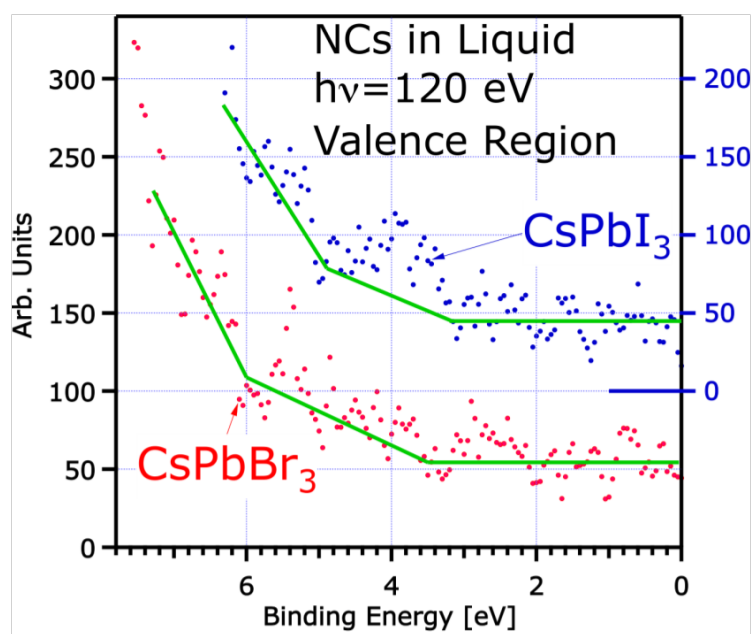


Figure 5.5: Valence region. The CsPbI<sub>3</sub> NCs spectrum is shifted upwards according to the right scale

Here, we bring the first valence band spectra of MHP NCs diluted in liquid. We manage to record spectra from the valence region for CsPbI<sub>3</sub> and CsPbBr<sub>3</sub>, which are shown in Fig.5.5. The HOMO or VBM are present below 6 eV BE, contrasting to what was reported for the isolated NPs study. We were able to record the HOMO structure at lower binding energy than 6 eV because no other levels from the solvents are present at these energies. In the CsPbI<sub>3</sub> signal, there is a contribution of up to 3.0 eV. A steeper increase occurs at 4.9 eV. For the CsPbBr<sub>3</sub> signal, there is a contribution up to 3.5 eV. However, the steeper increase in the signal occurs at 6.0 eV which agrees with the VBM of the MaPbBr<sub>3</sub> suspended in vacuum.

We concluded that there are differences in the observed valence band signals between the gas-phase (solid-state) and liquid environments. These differences suggest that the electronic properties and band structures of the Perovskite materials may be influenced by the surrounding medium, such as the presence of solvents or ligands in the liquid phase, leading to variations in the valence band characteristics.

## 6 CONCLUSION

---

This investigation delves into the use of electron spectroscopy studies on nanoparticles present in nonpolar liquids, which is a novel approach. Although there were some difficulties in conducting XPS investigations on liquid samples, this PhD project demonstrated that studying nanometal halide perovskite (MHP) under liquid conditions produces far more accurate results than the usual solid sample studies. This method fulfills essential conditions to provide a detailed analysis of solvated nano-systems, which can serve as a standard for their solid counterparts (e.g., dry nano-particles in a solid substrate). Among them, we can cite contamination-free NCs and constant renewal of samples leading to a one million times smaller radiation dose than solid samples measured during one second at the same spot.

Previously reported solid state chemically shifted Br 3d lines can be explained as being due to surface Br oxidation induced by radiation damage. To further support our findings, we measured the IPE beamline at Sirius for OLA and AF Perovskite NCs. When subjected to a solid-state XPS strategy, the findings indicated a radiation-induced degradation of perovskite nanocrystals. Oxidation in the Br 3d region was observed in NC, OLA, and AF samples, indicating their sensitivity to radiation-induced Br oxidation. In addition to the Br oxidation, Pb atoms show clear radiation-induced oxidation. The Pb-induced oxidation can affect the quality of photoluminescence quantum yield (PLQY) and act as charge carrier traps on quantum dot surfaces when exposed to visible and near-infrared. These findings are confirmed by a publication for CsPbI<sub>3</sub>. We identified Pb oxidated species for both Ncs, emphasizing the Amine-Free case in which the Pb species change their amount over time. It's worth mentioning that Pb<sup>2+</sup> species in the form of a shoulder were consistently observed for both synthesis methods even after changing the sample location, indicating the possibility of sample degradation due to extended vacuum exposure, regardless of radiation.

Oxidation significantly affects the Br/Cs and Pb/Cs ratios in XPS analysis. The OLA+ sample shows a decline in the Br/Cs ratio and an increase in the Pb/Cs ratio, while the amine-free (AF) sample experiences more abrupt changes. This indicates a significant loss of Br and Cs atoms due to radiation and vacuum damage, particularly in the more stable AF sample. The interpretation of pristine sample results from solid-state XPS data is being questioned. Our findings likely apply to other X-ray techniques.

We have developed a new XPS approach to study NCs in colloidal dispersion, which aims to address the challenges associated with this process. We have obtained XPS spectra for Cs 4d, Pb 4f, and Br 3d for both OLA and AF Ncs. Upon examining the ratio between Pb from both synthesis methods, we could identify a normalization factor of 0.53. This finding indicates that the two types of nanocrystals are located at different depths from the

vacuum-liquid interface. There were no significant differences in Br 3d peak intensity between the two methods, indicating no Br substitution. Our analysis contradicts the presence of two distinct Br species. The Cs 4d peak was significantly reduced in the OLA<sup>+</sup> spectrum, indicating Cs atom substitution. The Cs signal from the surface was 50±10% lower in OLA<sup>+</sup> compared to AF NCs.

A combination of XPS Br/Cs and Pb/Cs ratios, DFT calculations using the accurate orthorhombic geometry, and high-resolution electron microscopy confirm that the surface of the  $\approx$  6-18 nm NCs is terminated by a CsBr layer based on the total energy of the system. Our study also reveals that, with a photon energy of 600 eV, nearly half of the detected photoelectrons from the NCs come from the first monolayer of their surfaces. In contrast, 25% of these photoelectrons come from the second layer, and so on. Future research with higher statistics could explore small changes in the peak profile and determine if Cs substitution occurs in a second layer below the surface. The Br/Cs and Pb/Cs ratios also revealed distinct changes for the amine-free NCs, suggesting different surface stoichiometry than the bulk. Atomistic models for surface stoichiometric NCs were built. In our model, all six facets are constituted by the most stable CsBr terminations. The surface stoichiometries (equations B.8 and B.1.1 in Appendix B) impose that  $\alpha \approx 1/2$ , suggesting scarced substitution rates of Br<sup>-</sup> by oleylamine anions at the surfaces in the Amine-Free NCs. From the error bars, this rate might be between zero and 10%. Considering that  $\alpha$  is roughly the same for the OLA<sup>+</sup> sample, we conclude that the overall rate of OLA<sup>+</sup>  $\longleftrightarrow$  Cs<sup>+</sup> substitution on the NCs surfaces is between 60% and 70%. Besides, we could estimate the electron length of attenuation (ELA) in the NCs from  $\alpha$ , obtaining 4.29 Å.

That does not mean our main model is the only structure compatible with surface stoichiometry. The occurrence of different NCs, presenting PbBr<sub>2</sub> facets, is also a possible alternative. However, because of the higher surface energy, compared to the previous model, they are only statistically significant when dealing with smaller particles with an average size below 1 nm. The TEM images show that NCs size is 12-18 nm in size, excluding the PbBr<sub>2</sub> terminated NCs.

Our study also explores the Valence Band behavior in MHP nanocrystals within colloidal phases, revealing the impact of the environment on the band gap. The argument elucidates the electronic structure of OLA<sup>+</sup> Perovskite, addressing if and how ligand molecules could affect the electronic characteristics of these NCs within a solvent compared to under solid-state conditions. Combining experimental findings with Density Functional Theory calculations from the literature highlights the primary composition of the valence band, mainly consisting of Br 4p and Pb 6s states. Another study in the gas phase was taken as a comparison with our results, Although surface ligands challenge the determination of valence band edges in gas-phase Ultraviolet Photoelectron Spectroscopy (UPS) spectra, the research identifies the valence band maximum for small NCs as 6 eV. Moreover, the findings reveal that the VB composition remains consistent even for NCs in the 8-15 nm size range,

without significant deviations compared to bulk materials.

The research also records the first valence band UPS spectra of MHP NCs in liquid, specifically CsPbI<sub>3</sub> and CsPbBr<sub>3</sub>. The study reveals that the highest occupied molecular orbital (HOMO) or valence band maximum (VBM) is situated below 6 eV binding energy, providing insights into the electronic structure of these materials in liquid environments. This contrasts with isolated NC studies, as the absence of solvent-related energy levels enables the recording of HOMO structures at lower binding energies. These findings offer valuable information about the electronic properties and behavior of MHP NCs in colloidal phases. There are questions to be addressed for future investigations to explore alternative synthesis techniques and various ligands, focusing on understanding their impact on the surface stability of NCs and their correlation with their optoelectronic performance. Additionally, researchers can monitor changes in electronic structure and surface chemistry over time or under different external conditions like temperature, pressure, or gas exposure.

In summary, this work provides a solid foundation for further research into the electronic properties of nanomaterials in aqueous vicinity. Also, it offers a valuable tool for the continued development of nanoscience.

## BIBLIOGRAPHY

- [1] Kruse, C. The fel-simulator imaging nano-particle injectors using strong-field-ionisation time-of-flight mass-spectrometry (2015).
- [2] Willmot, P. *An Introduction to Synchrotron Radiation* (2011).
- [3] Seah, M. P. & Dench, W. A. Quantitative electron spectroscopy of surfaces: A standard data base for electron inelastic mean free paths in solids. *Surface and Interface Analysis* **1**, 2–11 (1979).
- [4] Ravi, V. K. *et al.* Origin of the substitution mechanism for the binding of organic ligands on the surface of cspbbr3 perovskite nanocubes. *The Journal of Physical Chemistry Letters* **8**, 4988–4994 (2017).
- [5] Chen, F., Imran, M., Pasquale, L., Salerno, M. & Prato, M. Long-term optical and morphological stability of cspbbr3 nanocrystal-based films. *Materials Research Bulletin* **134**, 111107 (2021).
- [6] Burschka, J., Pellet, N., Moon, S.-J. & *et al.* Sequential deposition as a route to high-performance perovskite-sensitized solar cells. *Nature* **499**, 316–319 (2013).
- [7] Liu, M., Johnston, M. B. & Snaith, H. J. Efficient planar heterojunction perovskite solar cells by vapor deposition. *Nature* **501**, 395–398 (2013).
- [8] Tsai, H., Nie, W., Blancon, J.-C. & *et al.* High-efficiency two-dimensional ruddlesden-popper perovskite solar cells. *Nature* **536**, 312–316 (2016).
- [9] Xing, G., Mathews, N., Lim, S. S. & *et al.* Low-temperature solution-processed wavelength-tunable perovskites for lasing. *Nature Materials* **13**, 476–480 (2014).
- [10] Zhang, Q., Ha, S. T., Liu, X., Sum, T. C. & Xiong, Q. Room-temperature near-infrared high-q perovskite whispering-gallery planar nanolasers. *Nano Letters* **14**, 5995–6001 (2014).
- [11] Zhu, H., Fu, Y., Meng, F. & *et al.* Lead halide perovskite nanowire lasers with low lasing thresholds and high quality factors. *Nature Materials* **14**, 636–642 (2015).
- [12] Tan, Z.-K., Moghaddam, R. S., Lai, M. L. & *et al.* Bright light-emitting diodes based on organometal halide perovskite. *Nature Nanotechnology* **9**, 687–692 (2014).
- [13] Xing, J., Yuan, Z., Yu, J. & *et al.* High-efficiency light-emitting diodes of organometal halide perovskite amorphous nanoparticles. *ACS Nano* **10**, 6623–6630 (2016).

- [14] Yuan, M., Quan, L. N., Comin, R. & et al. Perovskite energy funnels for efficient light-emitting diodes. *Nature Nanotechnology* **11**, 872–877 (2016). PMID: 27347835.
- [15] Hanna, M. & Nozik, A. Solar conversion efficiency of photovoltaic and photoelectrolysis cells with carrier multiplication absorbers. *Journal of Applied Physics* **100** (2006).
- [16] The national renewable energy laboratory. <https://www.nrel.gov/pv/interactive-cell-efficiency.html>. Accessed: 2023-08-13.
- [17] Protesescu, L. & et al. Nanocrystals of cesium lead halide perovskites ( $CsPbX_3$ , X=Cl, Br, and I): Novel optoelectronic materials showing bright emission with wide color gamut. *Nano Lett.* **15**, 3692–3696 (2015).
- [18] Bonato, L. G. *et al.* Photostability of amine-free  $CsPbBr_3$  perovskite nanocrystals under continuous uv illumination. *J. Mater. Chem. C* **11**, 8231–8242 (2023).
- [19] An, R. *et al.* Photostability and photodegradation processes in colloidal  $CsPbI_3$  perovskite quantum dots. *ACS applied materials & interfaces* **10**, 39222–39227 (2018).
- [20] Ali, H., Winter, B. & Seidel, R. The metal-oxide nanoparticle–aqueous solution interface studied by liquid-microjet photoemission. *Accounts of Chemical Research* 4511–4523 (2023).
- [21] Kim, G.-W. & Petrozza, A. Defect tolerance and intolerance in metal-halide perovskites. *Advanced Energy Materials* **10**, 2001959 (2020).
- [22] Akkerman, Q. A., Rainò, G., Kovalenko, M. V. & Manna, L. Genesis, challenges and opportunities for colloidal lead halide perovskite nanocrystals. *Nature materials* **17**, 394–405 (2018).
- [23] Siegbahn, K. Electron spectroscopy for atoms, molecules and condensed matter - an overview. *Journal of Electron Spectroscopy and Related Phenomena* **36**, 113–129 (1985).
- [24] Faubel, M., Schlemmer, S. & Toennies, J. P. A molecular beam study of the evaporation of water from a liquid jet. *Zeitschrift für Physik D Atoms, Molecules and Clusters* **10**, 269–277 (1988).
- [25] Röntgen, W. C. Ueber eine neue art von strahlen. *Annalen Der Physik* **300**, 1–11 (1898).
- [26] Istone, W. K. *X-Ray Photoelectron Spectroscopy (XPS)*, 235–268 (CRC Press, 2020).
- [27] Akbal, Z. Synchrotron radiation. *Graduate Texts in Physics* (2021).
- [28] Dupuy, R. *et al.* Core level photoelectron spectroscopy of heterogeneous reactions at liquid–vapor interfaces: Current status, challenges, and prospects featured. *J. Chem. Phys.* **154**, 060901 (2021). URL <https://doi.org/10.1063/5.0036178>.

- [29] Fadley, C. S. X-ray photoelectron spectroscopy: Progress and perspectives. *Journal of Electron Spectroscopy and Related Phenomena* **178-179**, 2–32 (2010).
- [30] Greczynski, G., Primetzhofer, D., Lu, J. & Hultman, L. Core-level spectra and binding energies of transition metal nitrides by non-destructive x-ray photoelectron spectroscopy through capping layers. *Applied Surface Science* **396**, 347–358 (2017). URL <https://www.sciencedirect.com/science/article/pii/S0169433216322760>.
- [31] Guerra, M., Jones, D., Colonna, F. P., Distefano, G. & Modelli, A. Decrease of the xps shake-up intensity on going from paranitroaniline to nitro-amino azabenzene. *Chemical Physics Letters* **98**, 522–526 (1983).
- [32] Baer, D. R. *et al.* Practical guides for x-ray photoelectron spectroscopy (xps): First steps in planning, conducting and reporting xps measurements. *Journal of Vacuum Science & Technology A* **37** (2019).
- [33] Aramesh, N., Bagheri, A. R., Nguyen, T. A. & Bilal, M. 3 - characterization techniques for nanomaterials used in nanobioremediation 29–43 (2022). URL <https://www.sciencedirect.com/science/article/pii/B9780128239629000180>.
- [34] Ni, H., Bi, X.-X. & Stencel, J. M. Tem studies on the morphology, size distribution and structure of nanocrystalline iron particles using a formvar embedded preparation technique. *MRS Proceedings* (1993).
- [35] Filip, Z. *et al.* Surface structure and morphology of m[com]o<sub>4</sub> (m = mg, zn, fe, co and m = ni, al, mn, co) spinel nanocrystals—dft+u and tem screening investigations. *Journal of Physical Chemistry C* (2014).
- [36] Stevie, F. A., Garcia, R., Shallenberger, J., Newman, J. G. & Donley, C. L. Sample handling, preparation and mounting for xps and other surface analytical techniques. *J. Vac. Sci. Technol. A* **38**, 063202 (2020). Submitted: 30 June 2020. Accepted: 20 August 2020. Published Online: 11 September 2020.
- [37] Baer, D. R. *et al.* Xps guide: Charge neutralization and binding energy referencing for insulating samples. *Journal of Vacuum Science & Technology A* **38** (2020).
- [38] Rocha, T. C. R. Ipe beamline (2023). URL <https://lnls.cnpem.br/facilities/ipe-en/>. Accessed on November 3, 2023.
- [39] Milosavljević, A. R. *et al.* Electronic properties of free-standing surfactant-capped lead halide perovskite nanocrystals isolated in vacuo. *The Journal of Physical Chemistry Letters* **9**, 3604–3611 (2018).
- [40] Rose, G. Ueber einige neue mineralien des urals. *Journal für Praktische Chemie* **19**, 459–468 (1840).

- [41] Burschka, J. *et al.* Sequential deposition as a route to high-performance perovskite-sensitized solar cells. *Nature* **499**, 316–319 (2013).
- [42] Grätzel, M. The light and shade of perovskite solar cells. *Nature Materials* **13**, 838–842 (2014).
- [43] Snaith, H. J. Perovskites: The emergence of a new era for low-cost, high-efficiency solar cells. *The Journal of Physical Chemistry Letters* **4**, 3623–3630 (2013).
- [44] Park, N.-G. Organometal perovskite light absorbers toward a 20% efficiency low-cost solid-state mesoscopic solar cell. *The Journal of Physical Chemistry Letters* **4**, 2423–2429 (2013).
- [45] Pu, Y., Cai, F., Wang, D., Wang, J.-X. & Chen, J.-F. Colloidal synthesis of semiconductor quantum dots toward large-scale production: a review. *Industrial & Engineering Chemistry Research* **57**, 1790–1802 (2018).
- [46] Karim, M. R., Balaban, M. & Ünlü, H. Strain effects on the band gap and diameter of cdse core and cdse/zns core/shell quantum dots at any temperature. *Advances in Materials Science and Engineering* 1–10 (2019).
- [47] Brkić, S. Applicability of quantum dots in biomedical science. In Djeddar, B. (ed.) *Ionizing Radiation Effects and Applications*, chap. 2 (IntechOpen, Rijeka, 2017). URL <https://doi.org/10.5772/intechopen.71428>.
- [48] Yassitepe, E. & et al. Amine-free synthesis of cesium lead halide perovskite quantum dots for efficient light-emitting diodes. *Advanced Functional Materials* **26**, 8757–8763 (2016).
- [49] Kim, G. & Petrozza, A. Defect tolerance and intolerance in metal-halide perovskites. *Advanced Energy Materials* (2020).
- [50] Akkerman, Q. A., Rainò, G., Kovalenko, M. V. & Manna, L. Genesis, challenges and opportunities for colloidal lead halide perovskite nanocrystals. *Nature Materials* **17**, 394–405 (2018).
- [51] Faubel, M., Steiner, B. & Toennies, J. P. Photoelectron spectroscopy of liquid water, some alcohols, and pure nonane in free micro jets. *Journal of Chemical Physics* **106**, 9013–9031 (1997).
- [52] Artiglia, L. *et al.* A surface-stabilized ozonide triggers bromide oxidation at the aqueous solution-vapour interface. *Nature Communications* **8** (2017).
- [53] Eggers, J. Nonlinear dynamics and breakup of free-surface flows. *Reviews of Modern Physics* **69**, 865–930 (1997).

- [54] Faubel, M. *Liquid Micro Jet Studies of the Vacuum Surface of Water and of Chemical Solutions by Molecular Beams and by Soft X-Ray Photoelectron Spectroscopy*, 597–630 (Springer International Publishing, Cham, 2021). URL [https://doi.org/10.1007/978-3-030-63963-1\\_26](https://doi.org/10.1007/978-3-030-63963-1_26).
- [55] Karslıoğlu, O. & Bluhm, H. *Ambient-Pressure X-ray Photoelectron Spectroscopy (APXPS)*, 31–57 (Springer International Publishing, Cham, 2017). URL [https://doi.org/10.1007/978-3-319-44439-0\\_2](https://doi.org/10.1007/978-3-319-44439-0_2).
- [56] Mun, B. S., Kondoh, H., Liu, Z., Ross, P. N. & Hussain, Z. *The Development of Ambient Pressure X-Ray Photoelectron Spectroscopy and Its Application to Surface Science*, 197–229 (Springer New York, New York, NY, 2014). URL [https://doi.org/10.1007/978-1-4614-8742-5\\_9](https://doi.org/10.1007/978-1-4614-8742-5_9).
- [57] Signorell, R. Electron scattering in liquid water and amorphous ice: A striking resemblance. *Phys. Rev. Lett.* **124**, 205501 (2020). URL <https://link.aps.org/doi/10.1103/PhysRevLett.124.205501>.
- [58] Seidel, R., Winter, B. & Bradforth, S. E. Valence electronic structure of aqueous solutions: Insights from photoelectron spectroscopy. *Annual Review of Physical Chemistry* **67**, 283–305 (2016). URL <https://doi.org/10.1146/annurev-physchem-040513-103715>. PMID: 27023757, <https://doi.org/10.1146/annurev-physchem-040513-103715>.
- [59] Ali, H., Seidel, R., Bergmann, A. & Winter, B. Electronic structure of aqueous-phase anatase titanium dioxide nanoparticles probed by liquid jet photoelectron spectroscopy. *J. Mater. Chem. A* **7**, 6665–6675 (2019). URL <http://dx.doi.org/10.1039/C8TA09414D>.
- [60] Roo, J. D. *et al.* Highly dynamic ligand binding and light absorption coefficient of cesium lead bromide perovskite nanocrystals. *Journal of Physical Chemistry Letters* **10**, 20712081 (2016).
- [61] Preobrajenski, A. *et al.* FlexPES: a versatile soft X-ray beamline at MAXIV Laboratory. *Journal of Synchrotron Radiation* **30**, 831–840 (2023). URL <https://doi.org/10.1107/S1600577523003429>.
- [62] WaveMetrics, Inc., P.O. Box 2088 Lake Oswego, OR 97035 USA. *Igor Pro*. [Http://www.wavemetrics.com/](http://www.wavemetrics.com/).
- [63] Hollas, J. *Modern Spectroscopy* (Wiley, 2004), 4th edn.
- [64] Campbell, J. L. Width of the atomic  $k-n7$  levels. *Atomic Data and Nuclear Data Tables* **77**, 1–56 (2001).

- [65] Kukk, E. Spectrum analysis by curve fitting (spancf)-macro package for igor pro. Tech. Rep., University of Turku (2012). Edwin.kukk@utu.fi.
- [66] Yeh, J. & Lindau, I. Atomic subshell photoionization cross sections and asymmetry parameters:  $1 \leq Z \leq 103$ . *Atomic Data and Nuclear Data Tables* **32**, 1–155 (1985). URL <https://www.sciencedirect.com/science/article/pii/0092640X85900166>.
- [67] Almeida, G. *et al.* Role of acid–base equilibria in the size, shape, and phase control of cesium lead bromide nanocrystals. *ACS Nano* **12**, 1704–1711 (2018). URL <https://doi.org/10.1021/acsnano.7b08357>. <https://doi.org/10.1021/acsnano.7b08357>.
- [68] Bonato, L. G. *et al.* Revealing the role of tin(iv) halides in the anisotropic growth of cspx<sub>3</sub> perovskite nanoplates. *Angewandte Chemie International Edition* **59**, 11501–11509 (2020). URL <https://onlinelibrary.wiley.com/doi/abs/10.1002/anie.202002641>.
- [69] Cottingham, P. & Brutchey, R. L. On the crystal structure of colloiddally prepared CsPbBr<sub>3</sub> quantum dots. *Chem. Commun.* **52**, 5246–5249 (2016). URL <http://dx.doi.org/10.1039/C6CC01088A>.
- [70] Bertolotti, F. *et al.* Coherent nanotwins and dynamic disorder in cesium lead halide perovskite nanocrystals. *ACS Nano* **11**, 3819–3831 (2017). URL <https://doi.org/10.1021/acsnano.7b00017>. <https://doi.org/10.1021/acsnano.7b00017>.
- [71] Yang, Y., Hou, C. & Liang, T.-X. Energetic and electronic properties of CsPbBr<sub>3</sub> surfaces: a first-principles study. *Phys. Chem. Chem. Phys.* **23**, 7145–7152 (2021). URL <http://dx.doi.org/10.1039/D0CP04893C>.
- [72] Lu, W. & Fu, Y. *Introduction to Physics and Optical Properties of Semiconductors*, 23–71 (Springer International Publishing, Cham, 2018). URL [https://doi.org/10.1007/978-3-319-94953-6\\_2](https://doi.org/10.1007/978-3-319-94953-6_2).
- [73] Cox, P. A. *The Electronic Structure and Chemistry of Solids* (Clarendon Press, 1987), 1st edn.
- [74] Volnianska, O., Szymura, M., Mikulski, J. & Kłopotowski, How surface proximity to copper dopants affects photoluminescence of cdse colloidal quantum dots. *J. Phys. Chem. C* **125**, 16827–16836 (2021). URL <https://doi.org/10.1021/acs.jpcc.1c04826>.
- [75] Laroui, H. *et al.* Nanomedicine in gi. *American Journal of Physiology-Gastrointestinal and Liver Physiology* **300**, G371–G383 (2011).
- [76] Peter, I. *Ratio of Surface Area to Volume in Nanotechnology and Nanoscience*. Basic Nanomechanics Series (Petra Books, 2011).

- [77] Gatin, A. *et al.* Less and less noble: Local adsorption properties of supported au, ni, and pt nanoparticles. *Nanomaterials (Basel)* **13**, 1365 (2023).
- [78] Alshehabi, A. On the plasmon contribution to x-ray electron emission spectroscopy background: q-statistical analysis. *Solid State Communications* **357**, 114979 (2022). URL <https://www.sciencedirect.com/science/article/pii/S0038109822003039>.
- [79] Kataoka, S. *et al.* Investigation of water structure at the tio<sub>2</sub>/aqueous interface. *Langmuir* **20**, 1662–1666 (2004).
- [80] Gopalakrishnan, S., Liu, D., Allen, H. C., Kuo, M. & Shultz, M. J. Vibrational spectroscopic studies of aqueous interfaces: Salts, acids, bases, and nanodrops. *ChemInform* **37** (2006).
- [81] Rana, S. *et al.* Spontaneous reduction of cu(ii) to cu(i) at solid-liquid interface. *The Journal of Physical Chemistry Letters* **9**, 5699–5704 (2018).
- [82] Liu, G., Jaegermann, W., He, J., Sundström, V. & Sun, L. Xps and ups characterization of the tio<sub>2</sub>/znpcgly heterointerface: alignment of energy levels. *The Journal of Physical Chemistry B* **106**, 5814–5819 (2002). URL <https://doi.org/10.1021/jp014192b>.
- [83] Brown, M. A. *et al.* In situ photoelectron spectroscopy at the liquid/nanoparticle interface. *Surface Science* **610**, 1–6 (2013).
- [84] Padalia, B. D., Lang, W. C., Norris, P. R., Watson, L. M. & Fabian, D. J. X-ray photoelectron core-level studies of the heavy rare-earth metals and their oxides. *Proceedings of the Royal Society A: Mathematical, Physical and Engineering Sciences* **354**, 269–290 (1977).
- [85] Jørgensen, C. K. Photoelectron spectra showing relaxation effects in the continuum and electrostatic and chemical influences of the surrounding atoms. vol. 8 of *Advances in Quantum Chemistry*, 137–182 (Academic Press, 1974). URL <https://www.sciencedirect.com/science/article/pii/S0065327608600611>.
- [86] Krause, M. O. & Wuilleumier, F. Photoionization of helium: study of he+h ν = he+(n=2)+e. *Journal of Physics B: Atomic and Molecular Physics* **5**, L143 (1972). URL <https://dx.doi.org/10.1088/0022-3700/5/7/003>.
- [87] Liu, Z. *et al.* Electronic properties of a new all-inorganic perovskite tlpbi<sub>3</sub> simulated by the first principles. *Nanoscale Research Letters* **12**, 232 (2017).
- [88] Parry, D. Atomic calculation of photoionization cross-sections and asymmetry parameters. *Gordon and Breach Science Publishers* (1993).
- [89] Cros, A. Charging effects in x-ray photoelectron spectroscopy. *Journal of Electron Spectroscopy and Related Phenomena* **59**, 1–14 (1992).

- 
- [90] Sturges, H. The choice of a class-interval. *American Statistical Association* **21**, Mar., 1926. URL <http://www.jstor.org/stable/2965501>.
- [91] Myrseth, V., Børve, K. J. *et al.* The substituent effect of the methyl group. carbon 1s ionization energies, proton affinities, and reactivities of the methylbenzenes. *The Journal of Organic Chemistry* **72**, 5715–5723 (2007).
- [92] Scott, D. W. On optimal and data-based histograms. *Biometrika* **66**, 605–610 (1979).
- [93] Faubel, M. *Photoionization and Photodetachment, Part I* (2000).

# APPENDIX A - XPS FITTING/CALIBRATION AND UNCERTAINTY DETERMINATION

---

[name=Appendix A]

In XPS data analysis, calibration involves aligning the XPS energy scale to reference energies, allowing for precise determination of binding energies of elements in a sample. Appropriate calibration is essential for obtaining reliable chemical information and identifying chemical states in the material under study. However, it is crucial to acknowledge that all scientific measurements inherently carry some degree of uncertainty. Despite the meticulous calibration process, uncertainties may arise due to instrumental limitations, sample conditions, or data analysis techniques. Scientists must consider and account for these uncertainties to make informed interpretations and draw reliable conclusions from their XPS data.

## A.1 XPS Fitting

MHPs' solid state spectra data analysis

We fitted the solid-state sampled spectra at different photon energies - 600, 850, 1253, and 1500 eV. For elemental analysis, we referred to photoionization cross-sections ( $\sigma(\omega)$ ) that were mentioned in literature [88]. The chosen values for this investigation are listed in table A.1. These cross-sections normalize the area under the XPS curves of an element, as the probability of ejecting an electron from an orbital varies with the photon energy. Thus, the signal, represented by a peak in an XPS scan, does not directly reflect the concept of 'one electron equals one element.' Hence, finding this relationship was necessary for our analysis to quantify Cs, Br, and Pb elemental content from the XPS spectra by calculating  $\text{area}/\sigma(\omega)$ . The XPS curves utilized in the elemental ratio are represented in Fig. A.1, A.2A.3. Apart from the ratio comparison, these curves allow us to dissect the spectra for Cs 4d, Br 3d, and Pb 4f. Our main objective was to quantify and differentiate each element's signal across multiple species of the same element. Error bars for each fitting were achieved by utilizing the residue points to calculate the standard deviation. A more detailed explanation of the statistical analysis process is available in Appendix Section A3. Due to a more degraded surface, the quality of OLA's spectra is significantly compromised, resulting in poorer statistics. As discussed in the main text, AF is less resilient than OLA when considering susceptibility to radiation damage.

A fitting for Pb 4f was required to determine the correlation between the spectra associated with radiation damage over time in the Pb region (refer to Fig. A.4). Calculating

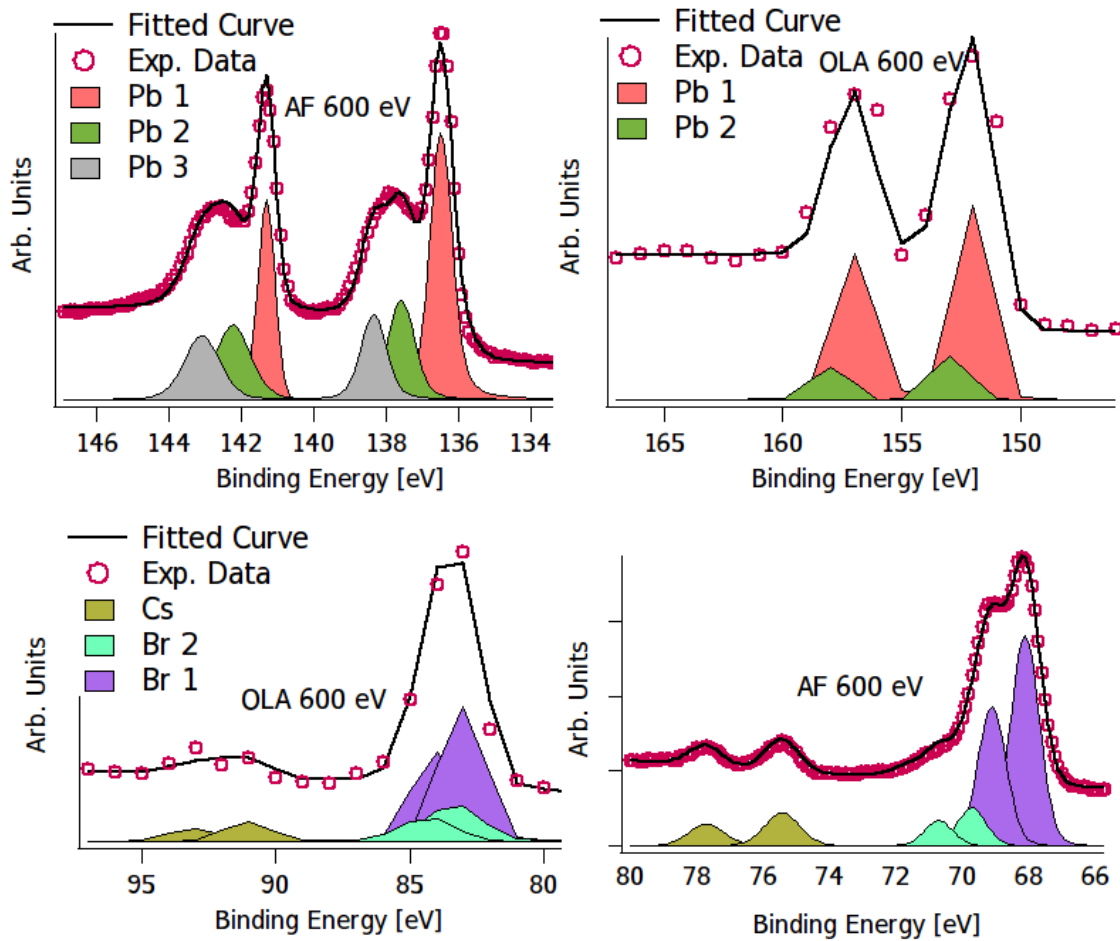


Figure A.1: The two sets of curves on the top refer to the Pb 4f for AF and OLA from the left to the right. Both exhibit oxidation species (in light red and green) in particular AF has an extra Pb oxidate species in gray. On the bottom OLA and AF spectra for Cs 4f and Br 3d. Cs region reveals only one type of Cs however the Br 3d has 2 types which were widely discussed in the main text.

Photonization Cross-Section					
Z	Atom Level	600 eV	850 eV	1253 eV	1500 eV
35	Br 3d	0.03801	0.06786	0.2264	0.6076
55	Cs 4d	0.07061	0.1096	0.257	0.4837
82	Pb 4f	0.3243	0.5452	1.503	3.098

Table A.1: Values for the photoionization cross-section as a function of photon energy [eV].

the area under each curve enabled us to distinguish the signal difference between curves with the same photon energy and synthesis method. Ultimately, we calculated the difference between the spectra of OLA and AF, obtained from Fig. 3.2 and Fig. 3.3 in the main text respectively. In OLA case, normalization took place between the 18-minute (in red circle) and the earlier curve (solid line in black). Eventually, the signal contract was 0.92 for the 18-minute curve. Similarly, the strategy for the AF case Pb 4f features merely following what was done for the previous spectra comparison. Now it is just a matter of summing all the

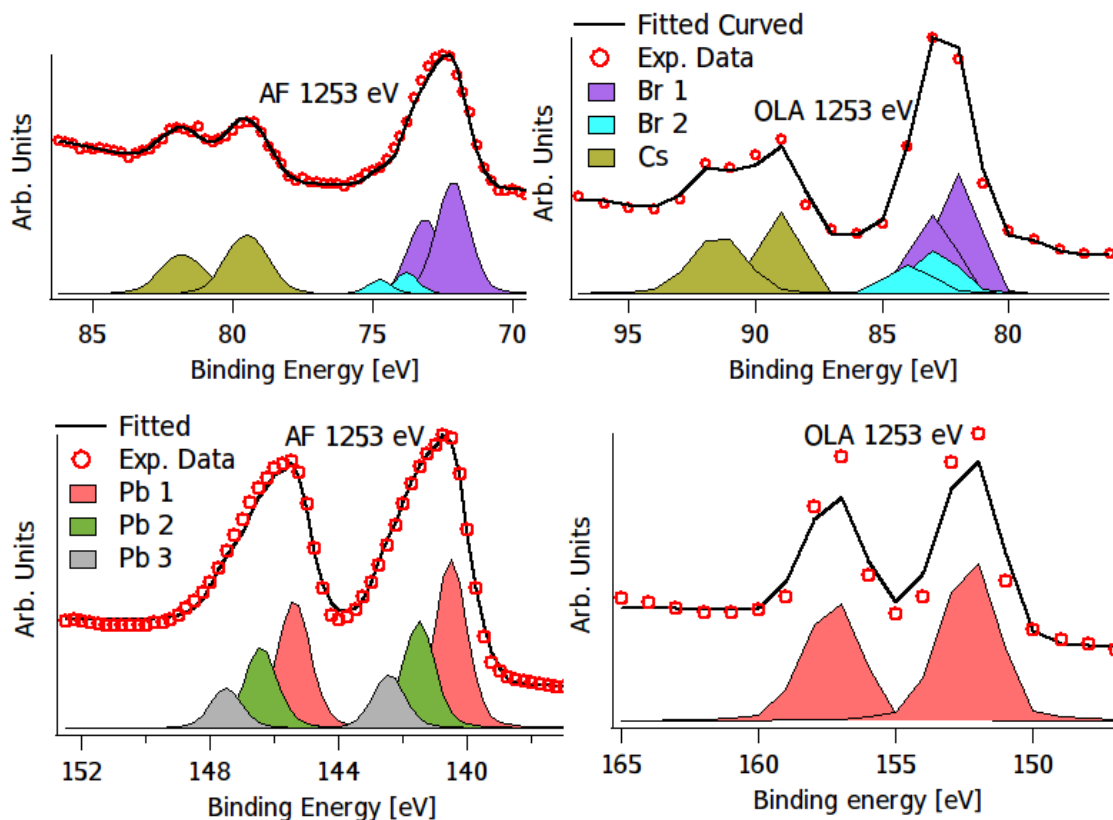


Figure A.2: Following the colors initially defined in the 600 eV spectra, we once again observe the same color scheme for both OLA and AF records: Pb 4f ions in light red and Pb oxide species in green and gray. Cs 4f and Br 3d 2 are indicated in purple for ionic Cs and in blue for the oxidized state."

contributions of each Pb species under the same curve and obtaining the ratio between the dark blue and light blue curves which we ended up in the value of 0.86 (see the figure on the bottom related to the Pb degradation in the main text). These values were used to multiply the respective curves and finally get a normalized picture.

It was obtained the spin-orbit split the values for both synthesis methods. For AF: Cs (3/2 - 5/2) eV 2.30 eV, Br (3/2 - 5/2) 1 eV and Pb (5/2 - 7/2) 4.75 eV. In OLA we have: Cs (3/2 - 5/2) 2.22 eV, Br (3/2 - 5/2) 1 eV and Pb (5/2 - 7/2) 4.96 eV. Values for Cs and Pb exhibit deviations between the AF and OLA synthesis methods, confirming the potential differences in their chemical environments. It seems that bromine has a stable and consistent chemical environment in both methods, as evidenced by the consistent values for Br in both methods. Additionally, the distance between elements experiencing different chemical environments reveals an important relationship. Tables A.2 and A.3 exhibit the BE distance between peaks of different elemental species for AF and OLA, respectively. Both tables do not contain values for Cs. This is because each spectrum only has one type of Cs.

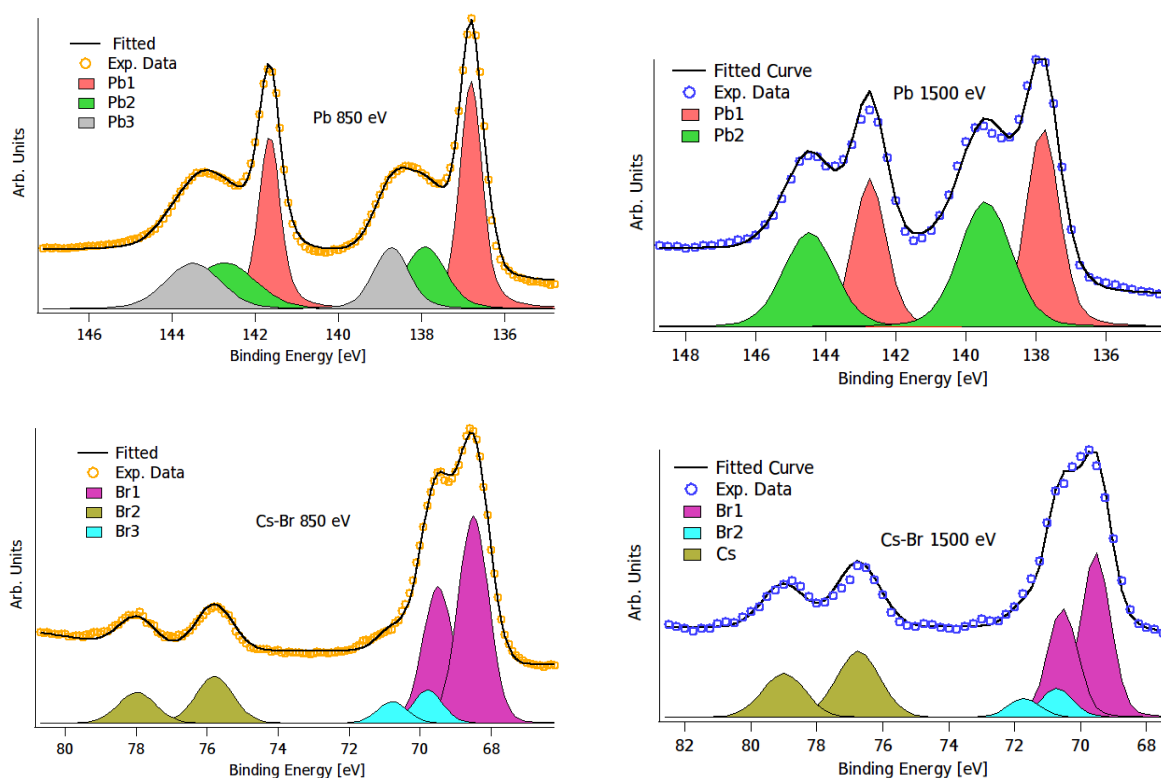


Figure A.3: Fitting for both 850 eV (in orange circle dots) and 1500 eV (in blue circle dots) from AF records (as it was not possible to acquire signal from Cs and Br for OLA NCs). The color scheme follows the same pattern as at 600 eV: Pb 4f ions are represented in light red, Pb oxide species in shades of green and gray, ionic Cs 4f in purple, and oxidized Br 3d 2 in blue. Exceptionally, the 1500 eV spectra only exhibited two types of Pb species among AF spectra.

AF Chemical Shift between Element Species				
BE difference between Element Types	600 eV	850 eV	1253 eV	1500 eV
Br2 - Br1	1.61 eV	1.34 eV	1.70 eV	1.10 eV
Pb2 - Pb1 (5/2)	0.90 eV	1.06 eV	1.03 eV	1.15 eV
Pb2 - Pb1 (7/2)	1.09 eV	1.19 eV	0.99	1.03 eV
Pb3 - Pb2 (5/2)	0.82 eV	0.84 eV	1.08 eV	0.56 eV
Pb3 - Pb2 (7/2)	0.76 eV	0.77 eV	0.92 eV	0.59 eV
Pb3 - Pb1 (5/2)	1.72 eV	1.90 eV	2.11 eV	1.61 eV
Pb3 - Pb1 (7/2)	1.85 eV	1.96 eV	1.91 eV	1.72 eV

Table A.2: The binding energy distance between elements peaks from all Amine-Free spectra.

## A.2 XPS Calibration

A noteworthy part of our data analysis spectra for our colloidal samples spectra was the energy calibration. Originally, we monitored the energy distance between the toluene C1s gas and liquid-phase peaks as a function of the photon flux. Depending on the photon flux, the

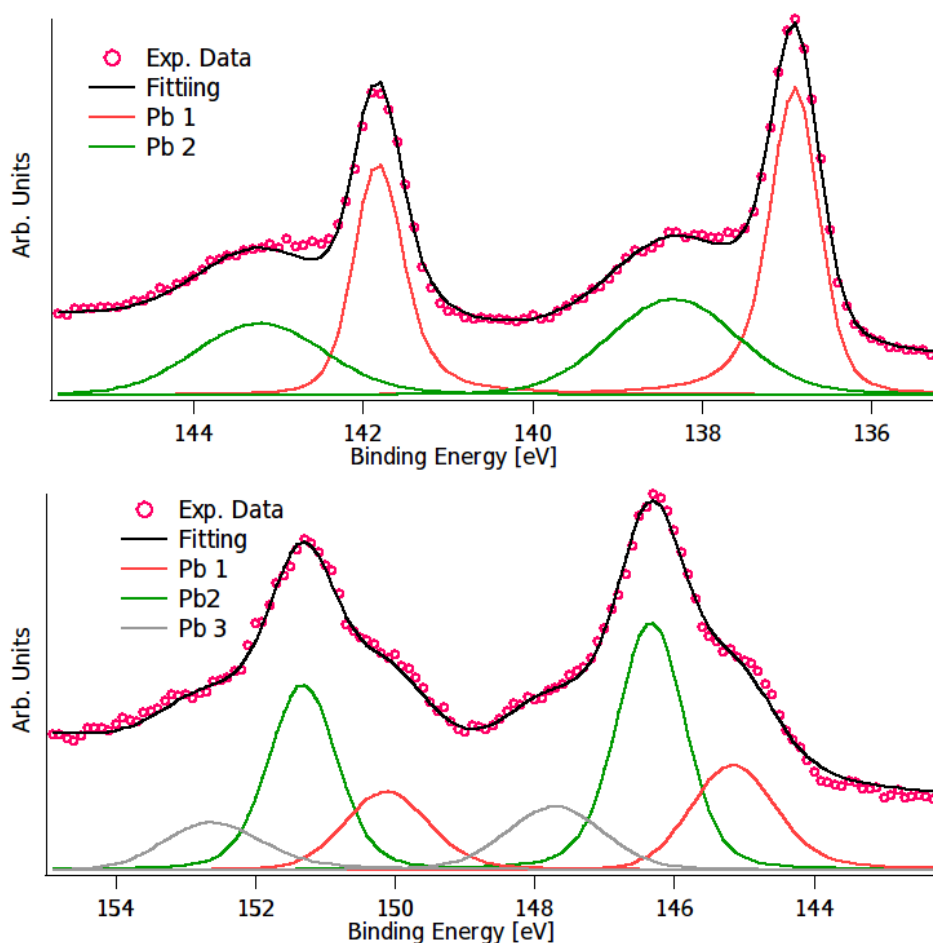


Figure A.4: The first figure is from the first scan where we have two types of Pb in red and green. For the bottom figure we have three Pb features the same two types from the first (the red and green features) but now followed by a third one in gray.

OLA Chemical Shift between Element Spicesn		
Atom Level	600 eV	1253 eV
Br2 - Br1	0.22	0.82 eV
Pb2 - Pb1 (5/2)	1.22 eV	- eV
Pb2 - Pb1 (7/2)	0.99 eV	- eV

Table A.3: The binding energy distance between elements peaks.

distance between the two features increases due to the charging effect. The phenomenon known as the charging effect pertains to accumulating a positive surface charge on an insulating sample when subjected to X-rays or charged particle beams. This charge can introduce distortions in the obtained XPS spectra, potentially yielding inaccurate or deceptive outcomes. The charging effect arises due to the insulating nature of the sample, impeding the dissipation of charge created by the photoelectrons generated by the incident X-rays, consequently leading to a build-up of positive charge on the sample surface [89].

Liquid toluene is a non-polar solvent that exhibits a relatively low dielectric constant. Indeed at higher flux, the isolating Toluene liquid micro-jet changes more due to the

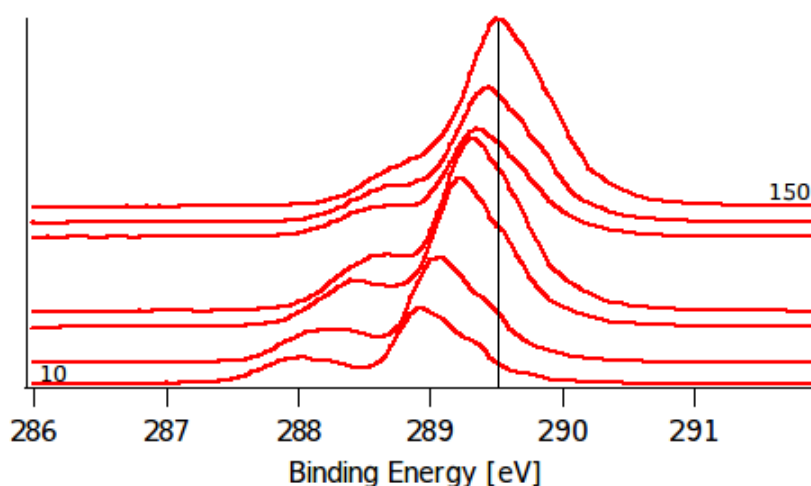


Figure A.5: Spectra for Toluene C1s region for a beamline slit increasing at 10, 25, 5, 60, 75, 100 and 150  $\mu\text{m}$ , respectively, from below to upward. The C1s has two features: the gas phase on the right (the most protuberant contribution) and liquid phase on the left.

ejection of photoelectrons. The gas phase part of the C1s peak is less affected by changes since the electric potential from the cylindrical liquid jet decays as  $1/r$  ( $r$  = the radial distance). By measuring the distance between the C1s gas and liquid phase peaks at decreasing photon flux, we aim to extrapolate this split to zero photon flux and zero charging. Knowing the calibrated energy of the gas phase signal and the shift gas-liquids, we can obtain calibrated C1s liquid signal. Subsequently, we can use the C1s liquid energy to calibrate all the peaks in our sample.

In Fig.A.6, one can see seven spectra of toluene C1s for different photon fluxes. Looking at them, it is possible to identify that the gas and liquid peaks move away with the decreasing photon flux incident on the sample. The liquid-gas energy distance is plotted in Fig.???. We made a least square fit using a quadratic curve. Extrapolation to zero photon flux gives 0.984 eV. This means the toluene liquid is shifted by 0.98 eV to the gas peak. Remaining for us to determine the calibrated energy of the C1s peak gas peak. In [90,91], we identify the calibrated value of 290.120 eV for Toluene C1s gas-phase.

To obtain the “calibration-shift” values for OLA<sup>+</sup> and Amine-Free (AF) core level, one must select the Pb spectrum recorded for the same photon flux (slit size). In the Amine-Free case, we used spectra recorded using 60  $\mu\text{m}$  slit size. Applying the calibrating shift at the Pb spectra, we expect to obtain the shift values for the Cs-Br since the Pb is within the nanocrystal. Therefore the chemical shift presented by its spectrum is only due to the liquid environment. For the OLA<sup>+</sup> sample, we had to use another procedure because, unfortunately, the toluene C1s liquid spectra taken using 60  $\mu\text{m}$  slit could not be separated from the gas phase spectra. However, we noticed that it operated a 7  $\mu\text{m}$  slit for the C1s toluene liquid spectra, and the C1s gas phase was separated enough to identify the liquid peak we needed for calibration. We got the values of Pb and C1s using 7  $\mu\text{m}$  slit. Now having the calibrated spectrum of Pb at 7  $\mu\text{m}$  slit, we calibrate the spectra of Pb using 60  $\mu\text{m}$  slit. Finally, from the

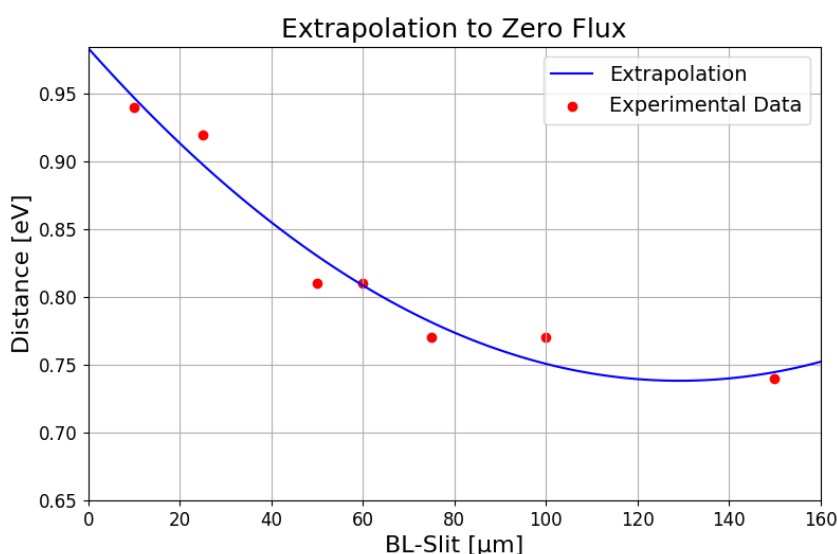


Figure A.6: The values of the distance between the gas and liquid peaks (at the ordinates) as a function of the photon flux aperture from the beamline (at the abscissas) are illustrated above. The points gave us two possible functions: exponential and quadratic. Since as much closer the photon flux approaches zero on the exponential curve, the distance goes to infinity, so we used the quadratic one.

Pb calibrated spectra at 60  $\mu\text{m}$  we calibrated the spectra of Cs-Br also taken at 60  $\mu\text{m}$  slit. In Table A.4, We show the Binding Energy (BE) for C1s, Pb4f and Cs-Br from both OLA and AF.

The table shows the chemical shifts of core-level electrons between Amine-Free and Oleylamine-capped. These chemical shifts may be fundamental in understanding the two methods' electron binding characteristics and ionization potential. In the context of ionization potential, the chemical shifts directly relate to the energy required to remove an electron from an atom or molecule, leading to the formation of an ion. In this analysis, a positive chemical shift signifies that the core-level electron in the OLA+ sample is less tightly bound than its counterpart in the AF sample. Conversely, a negative chemical shift suggests that the electron is more strongly bound in the OLA+ sample.

For instance, we observe that the binding energies (BE) for the Pb 4f electrons in the OLA+ sample are slightly smaller than those in the AF sample. This implies that it requires less energy to ionize the Pb 4f electrons in the OLA+ sample, indicating a lower ionization potential than the AF sample. Similarly, the BE for Cs 4d and Br 3d electrons also show differences between the samples. The Cs 4d and Br 3d electrons in the OLA+ sample exhibit higher binding energies, resulting in a higher ionization potential, as indicated by the positive chemical shifts.

### A.3 Uncertainty: Residual Analysis

The data quality shall be classified through its uncertainty analysis which in the XPS measurement may be caused by several components such as the X-ray flux; analyzer pass en-

Chemical shift between the two samples	
Amine-Free Samples Values	Calibrated Values
Tol C1s	289.14
Pb 4f 5/2	148.00
Pb 4f 7/2	143.10
Cs 4d 3/2	81.18
Cs 4d 7/2	78.88
Br 3d 3/2	72.78
Br 3d 7/2	71.78
OLA <sup>+</sup> Samples Values	Calibrated Values
Tol C1s	289.14
Pb 4f 5/2	147.94
Pb 4f 7/2	143.07
Cs 4d 3/2	82.20
Cs 4d 7/2	79.92
Br 3d 3/2	73.89
Br 3d 7/2	72.82

Table A.4: Here we present the BE for AF and OLA of the Toluene C1s as well as Pb and Cs-Br with their spin-orbit contributions. The last values show us the AF-OLA shift, which might give us a hint about the Ionization potential for the two different methods.

ergy; aperture settings; area of sample available for analysis. Looking at the signal-to-noise relation as well as the background shape, one may define the quality of spectra. Thus, we used a procedure to provide the uncertainty based on residues (which is defined as the difference between the fitting curve to the experimental curve). First, we set up the parameters in IGOR PRO to yield a fit that would be as close as possible to the experimental points so that the residue contains only the statistical uncertainty. We used the XPS spectra of the core lines Pb 4f, Cs 4d, and Br 3d from CsPbBr<sub>3</sub> with OLA<sup>+</sup> and AF. Please notice that the residual lines can not be extracted from the fitting procedure directly since fitting parameters are constrained to physical boundaries such that they did not produce a proper background and noise. The idea here was that if we average this residue, we will get close to zero and the standard deviation of the residue will then be  $\sigma$ . Thus, unlike what was done to fit the Pb, Cs, and Br peaks, we add extra peaks and leave most fitting parameters free. For instance, we allow the Voigt Full Width at Half Maximum (FWHM) and asymmetry to change freely. Keeping the energy position of the former peaks (Pb 4f, Cs 4d, and Br 3d) the same.

In Fig. A.7 below, we show the fitted spectra according to this procedure. The pinkish circles are the experimental spectra, while the black solid line is the sum of all element's features and the background. The blue solid line is the residue, and the straight solid black line is the background. After we obtain a suitable residue, we start "binning" the

residue data points, one can see this procedure for the Cs and Br AF case in Fig. A.8, and in the lower part of the figure, the blue dots are the residue. We bin the data in intensity intervals slightly smaller than 50 counts in each bin. All the data in the bin is added, and the added counts' intensity corresponds to the height of each rectangle in the upper spectrum. We determine the width of each bin interval according to Sturges and Scott's rule [92] ( $k = \lceil \log_2(n) + 1 \rceil$ ). As we can see, the intensity of the bins, represented by rectangles, resembles a Gaussian distribution, as expected. We fitted a Gaussian to the binned spectrum and obtained an average differing only 2%

Spectra Uncertainty	
Peak	Uncertainty
Pb OLA <sup>+</sup>	68.23
Pb AF	77.36
Cs and Br OLA <sup>+</sup>	32
Cs and Br AF	43.13

Table A.5: The  $\sigma$  for each spectrum measuring the spread in the distribution about the mean value (zero).

We obtained sigmas for all four spectra (see Table A.5) after establishing a procedure to evaluate the area uncertainties so that we could determine the Pb/Cs and Br/Cs area ratio uncertainty corrected by the ionization cross-sections for OLA<sup>+</sup> and AF methods. These ratios are related to the amount of each element on the NCs surface. First, we spot the background contribution in the experimental spectra. Second, we aimed to get two spectra: one adding  $+\sigma$  at the non-background features and the other taking off  $-\sigma$  to the non-background points. One could use a Python-based algorithm to identify the background points. This algorithm considers all points in the background with an intensity smaller than one sigma after it adds  $\pm\sigma$ . Thereby we were able to get the  $\pm\delta$  for the area in each peak of the four spectra, e.g., in the Pb 4f spectra, we got two  $\delta$  values regarding the spin-orbit split (5/2 and 7/2). After comparing the  $\pm\delta$ , we decide that the larger one should be taken as the uncertainty in the area. Since both spin-orbit components give the same physical information in the present case, we combine the two to reach better statistics and reduce the error bar. For instance, the uncertainty from the sum of Br 3d<sub>5/2</sub> plus Br 3d<sub>3/2</sub> with OLA<sup>+</sup> is 3.47%, depicted in Table A.6.

In order to account for uncertainty in the Br/Cs and Pb/Cs ratio, we utilized the same areas that were employed in the previously outlined process. We then multiplied the photoionization cross-sections for each respective element. The resulting values are as follows: Br/Cs AF = 0.65; Br/Cs OLA = 0.31; Pb/Cs AF = 0.18; Pb/Cs OLA = 0.10.

XPS Area Uncertainty	
Peak	Uncertainty
Br3d OLA <sup>+</sup> 5/2 + 3/2	3.47%
Cs4d OLA <sup>+</sup> 5/2 + 3/2	17.87%
Br3d AF 5/2 + 3/2	4.89%
Cs4d AF 5/2 + 3/2	12.72%
Pb4f OLA <sup>+</sup> 7/2 + 5/2	6.51%
Pb4f AF 7/2 + 5/2	12.98%

Table A.6: The values for the area uncertainty, which is related to the element amount in the sample. It was considered the maximum uncertainty between the  $+\sigma$  and  $-\sigma$ .

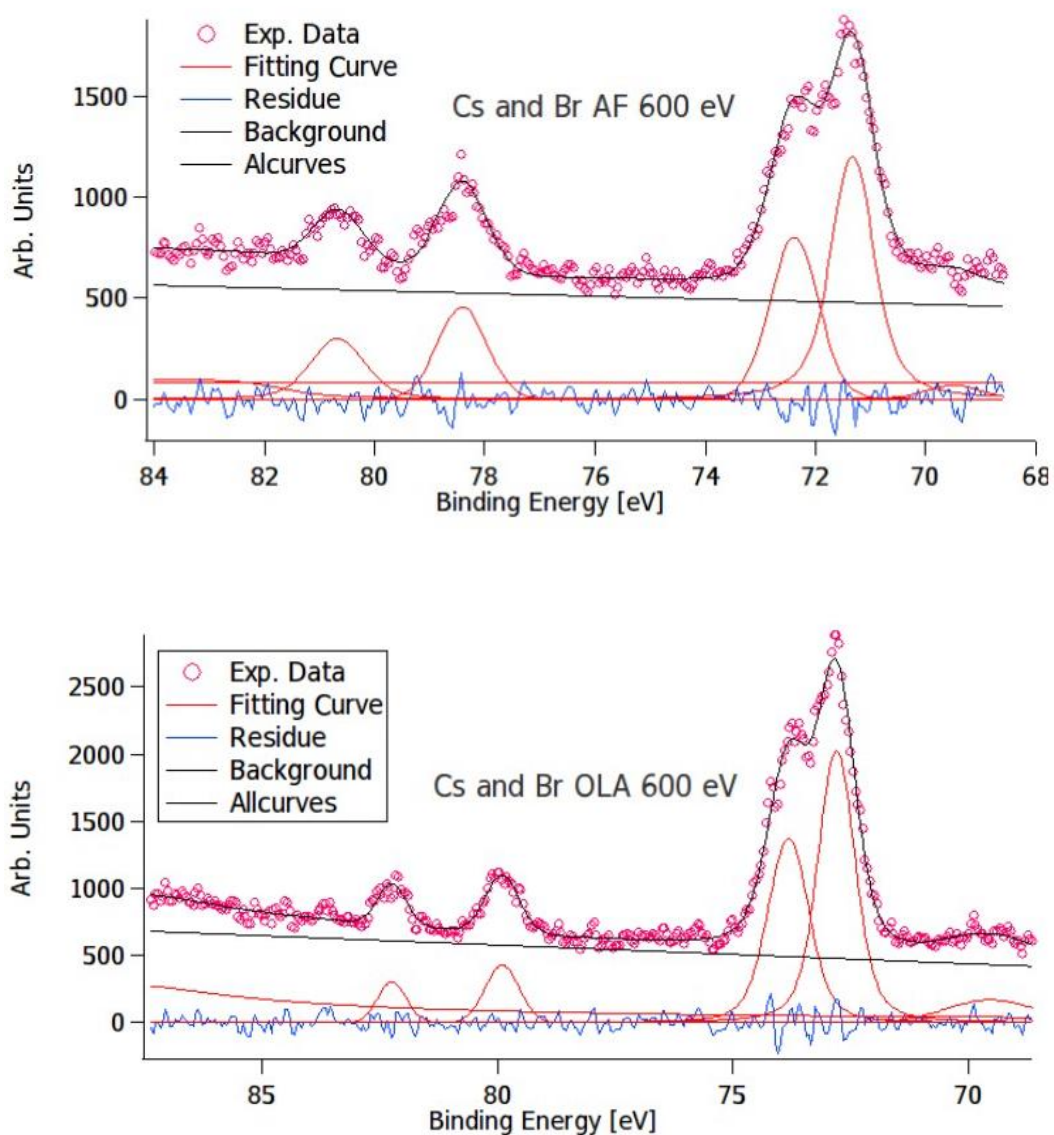


Figure A.7: Cs and Br fitting. The circles in pink are experimental points, and the solid black curve is the sum of all peaks. Black straight lines are the background, solid red is Voigts, and blue residue. In the top spectra, we added two extra peaks: around 84 to 82 eV and another 70 to 68 eV. In the bottom fitting also were added two extra peaks, but now one of them was an arc-tangent shape covering from 84 to 68 and the other from 71 to 69 eV. The objective was to get a fitted line as close as possible to the experimental data. See text for more details.

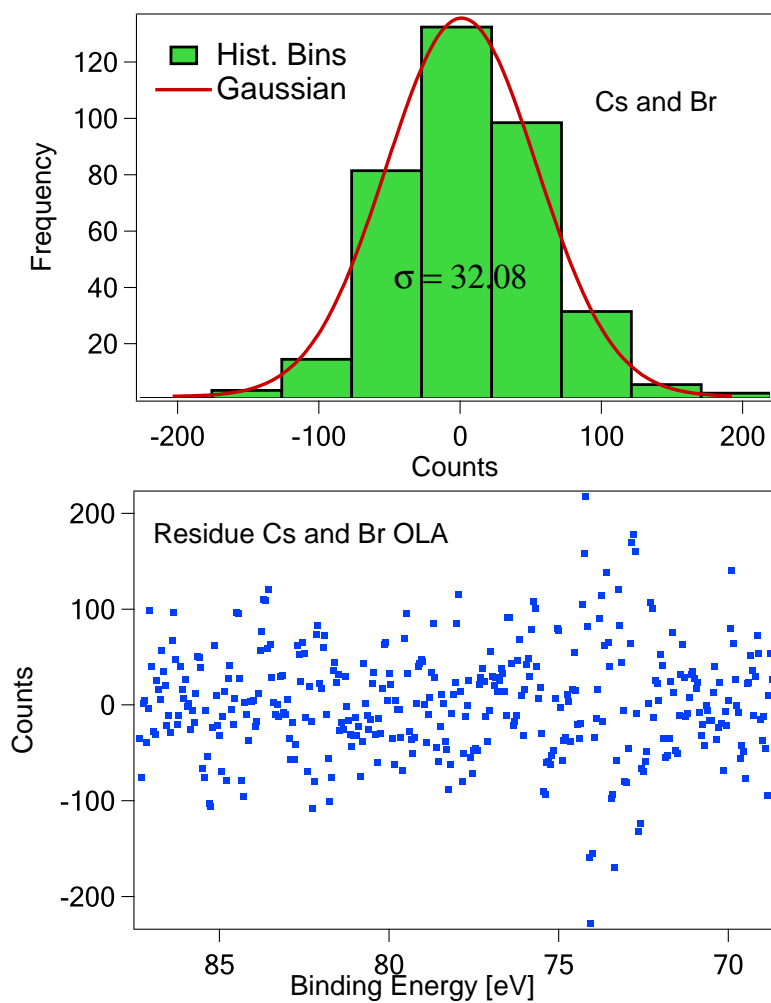


Figure A.8: Blue dots refer to the Cs and Br OLA spectrum residue. We produced a histogram from the scattered blue points (the top image in green). From the histogram, we could get the respective Gaussian Distribution which has a  $\sigma = 32.08$ .

## APPENDIX B - NANOCRYSTAL THEORETICAL MODEL

---

Here in the first section, we are going to address the model for NC. MHPs bearing pseudocubic structures have emerged as pivotal subjects of study, owing to their remarkable properties and potential applications across diverse domains. This investigation is dedicated to comprehending NCs featuring stable non-polar terminations, with specific emphasis on the CsBr and PbBr<sub>2</sub> surfaces. A profound comprehension of their structural and energetic facets is pivotal to optimizing their utilization in areas like optoelectronics and photovoltaics. In another section, we investigate the interplay between XPS signal intensity and the NC structure, taking into account the contributions from individual atomic layers. We start with the reasonable assumption that the signal's strength is highest when it originates from the termination layer, gradually decreasing as we move into deeper layers, following an exponential depth distribution. Based on this assumption, we establish an attenuation factor, which represents the ratio of signal intensities originating from atoms in consecutive layers. The primary consequence of this factor is the attenuation of the signal. The obtained factor allowed us to determine the eventual amount of atom substitutions in the outermost layers. To our knowledge, this is the first time such a factor has been evaluated for a nano-particle immersed in liquid and the evaluation can be extended for any nano-particle in solution.

### B.1 Nanoparticles Model

Our model for the NCs is assumed to be pseudocubic (six faces of similar surface areas) particles consisting of the most stable non-polar terminations. According to the adopted orientation (displayed on Fig. 2a in the main text), the terminations are characterized by the [001] and [110] indices and, along with both directions, the two possible CsBr and PbBr<sub>2</sub> surfaces were considered (Fig. 2b in the main text). We have performed DFT calculations in order to investigate both the bulk and surface structures, as well as their energetic features, of the orthorhombic phase. Slab models were employed for the [001] and [110] surfaces, in which all slab cells have an asymmetric arrangement of 5 CsBr and 5 PbBr<sub>2</sub> stacked layers, together with 15 Å of vacuum gap. The asymmetric slabs were built in such a way that the supercells respect the bulk stoichiometry. Two different relaxation calculations were performed in order to study CsBr and PbBr<sub>2</sub> terminations along each direction, and four (the bottom ones) out of the ten layers are kept frozen during the relaxation in each case. The number of layers guarantees the convergence of both energy and structure features in comparison to the bulk. All electron-core interactions were described using the projector augmented-wave (PAW) method. The kinetic energy cutoffs used for wavefunction and charge density were

50 Ry and 250 Ry, respectively, which is reasonable for PAW calculations. The description of the exchange-correlation potential was addressed with the PBE parametrization of the generalized gradient approximation (GGA) functional. We have used the Marzari-Vanderbilt smearing of 0.005 Ry widths to speed up the convergence. We include the van der Waals dispersion corrections in all calculations. Such long-range interactions are absent in the usual GGA and its importance for accurate descriptions of both geometry and electronic structure has been observed. For SCF convergences and structure relaxations, the Brillouin zone integrations were performed over an  $8 \times 8 \times 6$  Monkhorst-Pack  $k$ -point mesh for bulk calculations,  $8 \times 8 \times 1$   $k$ -point mesh for the [001] surfaces, and  $6 \times 6 \times 1$   $k$ -point mesh for the [110] surfaces. All calculations were performed using the Quantum ESPRESSO software package (v.6.7).

The characterizations for both the  $\text{CsPbBr}_3$  bulk and the four considered surfaces are consistent with previous works [4,71]. From the bulk calculations, we obtained the lattice parameters of  $a = 8.27 \text{ \AA}$ ,  $b = 8.33 \text{ \AA}$  and  $c = 11.91 \text{ \AA}$ , which are in good agreement with the previous studies. The bulk structure shows alternate stacking of two kinds of charge-neutral layers; one containing Cs and Br atoms in 1:1 ratio (CsBr layer) and the other containing Pb and Br atoms in a 1:2 ratio ( $\text{PbBr}_2$  layer). Both Cs and Br atoms in a CsBr layer lie on the same plane, while because of the octahedron tilting, the Pb and Br atoms in a  $\text{PbBr}_2$  layer are not exactly on the same plane. Instead, taking the plane containing the Pb atoms as a reference, the Br atoms divide themselves into two groups; one  $0.30 \text{ \AA}$  above and another  $0.30 \text{ \AA}$  below that reference. For the octahedron structure, we found the distance between Pb and the nearest Br atoms on the  $\text{PbBr}_2$  plane to be  $2.98 \text{ \AA}$ , while the distance between the Pb atoms and the nearest Br atoms on the CsBr plane is  $3.00 \text{ \AA}$ . The alternating CsBr/ $\text{PbBr}_2$  layers along the [001]-direction are arranged with a distance of  $d = 2.98 \text{ \AA}$ , corresponding to a distance between two equivalent layers of  $5.96 \text{ \AA}$ .

The optimization of the slabs shows that the distance between consecutive layers at the surface differs from that of the bulk by less than 0.5% in all cases. However, in the [001]CsBr case, the interlayer distance between the top CsBr layer and the  $\text{PbBr}_2$  layer immediately below it is significantly shorter than that in bulk ( $2.57 \text{ \AA}$ ). Still, about the [001]CsBr termination, we found that the top CsBr layer does not hold the Cs and Br atoms on the same plane. The relative rumpling creates two parallel planes - one of the Cs atoms and another one of the Br atoms - about  $0.37 \text{ \AA}$  apart. For the [001] $\text{PbBr}_2$  termination, we also observed that the distance between the top  $\text{PbBr}_2$  layer and the CsBr layer immediately below it is shorter than the bulk ( $2.87 \text{ \AA}$ ), but the effect is less significant. The half-octahedron structures at the surface share similar features with the bulk. We found the distance between Pb and the nearest Br atoms on the top  $\text{PbBr}_2$  layer to be  $2.96 \text{ \AA}$ , whereas the distance between the Pb atoms and the nearest Br atoms on the CsBr layer immediately below is  $2.90 \text{ \AA}$ ,  $0.1 \text{ \AA}$  shorter than that in the bulk. The tilting angles associated with the octahedra do not suffer significant alterations at the surface. The values differ from the ones shown in Fig 1.a by less than  $1^\circ$ .

The energetics of the bulk was studied using the following procedure. One unit cell of the bulk is formed by 4 Cs atoms, 4 Pb atoms, and 12 Br atoms (Fig. 2a in the main text), i. e., 4 times the formula unit (f.u.) 1Cs/1Pb/3Br. The formation energy per bulk unit can be defined as  $E_{bulk} - 4E_{Cs} - 4E_{Pb} - 12E_{Br}$ , where  $E_{bulk}$  is the total energy per unit cell of the bulk and  $E_{Cs}$ ,  $E_{Pb}$  and  $E_{Br}$  are the energies of the atoms on their element phases. The formation energy per formula unit is therefore  $\Delta H_{bulk} = E_{bulk}/4 - E_{Cs} - E_{Pb} - 3E_{Br}$ . Naturally, the atomic terms were calculated at the same level of theory, and we obtained  $\Delta H_{bulk} = -7.78$  eV. For comparison, our calculations for the cubic phase with the same methodology give  $\Delta H_{bulk} = -7.76$  eV, about 17 meV per f.u. above the orthorhombic result. Our  $H_{bulk}$  value for the cubic phase is in good agreement with the results reported by Yang *et al* [71].

On the other hand, the energetics of the surfaces here were in an alternative approach, compared to the work published by Yang *et al.* [71]. Here the surface energy is built as a function of the cleavage energy  $E_{cle}$ . Upon a cleavage parallel to the xy plane, the bulk is decomposed into two structures with complementary terminations. The cleavage energy is transferred to the subsequent structures, and from the energy conservation, we can write  $E_{cle} = E_{cle}^{CsBr} + E_{cle}^{PbBr_2}$ . Our unrelaxed asymmetric slab respects the bulk stoichiometry and contemplates both CsBr (top) and  $PbBr_2$  (bottom) terminations, so the total cleavage energy is given by  $E_{cle} = E_{unrelaxed} - nE_{bulk}$ , in which  $E_{unrelaxed}$  is the total energy of the unrelaxed slab and n is the number of bulk formulas in the slab. Using a first approximation, we assume  $E_{cle}^{CsBr}$  and  $E_{cle}^{PbBr_2}$  to be similar quantities. Finally, the surface energy is

$$\gamma^s = \frac{E_{cle}^s + E_{rel}^s}{S^s},$$

where the superscript s stands for the surface (CsBr or  $PbBr_2$ ),  $E_{cle}^s$  is the energy transfer to the (rigid) slab upon cleavage,  $S_{slab}$  the relaxed slab area and  $E_{rel}^s = E_{relaxed}^s - E_{unrelaxed}^s$  is the relaxation energy. We have obtained  $E_{cle} = 1.06$  eV per slab of the [001] surfaces and  $E_{cle} = 2.33$  eV per slab of the [110] surfaces.

Out of all the considered surfaces, the most stable NCs have two CsBr terminations in the [001] direction and four CsBr terminations in the [110] direction (Tab. S1), which agrees with the previous results [71].

Surface	$E_{rel}$	$\gamma$
[001]CsBr	-13.8	14.5
[001]PbBr <sub>2</sub>	-8.5	14.8
[110]CsBr	-13.0	14.9
[110]PbBr <sub>2</sub>	-9.8	15.2

Table B.1: Relaxation energies  $E_{rel}$ , in meV/f.u., and surface energies, in meV/Å<sup>2</sup>, for all considered terminations.

### B.1.1 b) Relation between XPS signal and surface stoichiometry

The total recorded photoelectron (PE) signal arising from a particular atomic species  $i$  is given by [93]

$$N_i = \sigma_i A \int_0^\mu n_i(z) \exp \left[ -\frac{1}{\text{ELA}} \int_0^z \frac{n_{tot}(\xi)}{n_0} d\xi \right] dz, \quad (\text{B.1})$$

where the constant  $A = \gamma FT$  is an experimental factor,  $\mu$  is the sample size in the  $z$  direction, ELA is the *electron length of attenuation*, which depends on the inelastic mean free path of the PE,  $\sigma_i$  is the atomic photoionization cross-section of the species  $i$  and  $n_i$ ,  $n_{tot}$  and  $n_0$  describe the  $i$ -, total and average target density functions. In the case of low energy photons, the signal arises mostly from the sample surface, so  $\mu \rightarrow \infty$  is a good approximation for the integral in expression 1.

Our goal is to apply equation 1 to a sample composed of CsPbBr<sub>3</sub> NCs in a (organic) solvent environment. Supposing that the solvent is distributed between  $0 < z < z_0$  (see Fig. B.1) and recalling that the NCs are composed by alternating CsBr and PbBr<sub>2</sub> layers, the density functions can be built like

$$n_{tot}(z) = n_{sol}(z) + n_{\text{NC}}(z) \approx n_{sol}^0 \theta(z_0 - z) + n_{\text{NC}}(z) \quad (\text{B.2})$$

and

$$\begin{aligned} n_{\text{NC}}(z) &= n_{\text{Cs}}(z) + n_{\text{Pb}}(z) + n_{\text{Br}}(z) \\ &= \sum_{j=0}^{\infty} \delta(z - z_0 - ja) + \sum_{j=0}^{\infty} \delta(z - z_0 - ja - a/2) + \\ &+ \sum_{j=0}^{\infty} [\delta(z - z_0 - ja) + 2\delta(z - z_0 - ja - a/2)] \\ &= \sum_{j=0}^{\infty} \left[ \underbrace{2\delta(z - z_0 - ja)}_{\text{CsBr layers}} + \underbrace{3\delta(z - z_0 - ja - a/2)}_{\text{PbBr}_2 \text{ layers}} \right]. \end{aligned} \quad (\text{B.3})$$

In the above equations, we considered that the NC has a cubic structure - of lattice parameter  $a$  - for simplicity, although the results presented here can be viewed as a good approximation for the orthorhombic phase NCs. In our example, the termination is a CsBr layer facet. Besides,  $n_{sol}^0$  is the average density of the solvent,  $\theta$  is the Heaviside function and the coefficients 2 and 3 associated with the delta functions in equation 3 reflect the layers stoichiometries (CsBr and PbBr<sub>2</sub>).

Using equations 2 and 3, and considering  $z > z_0$ ,

$$\int_0^z n_{tot}(\xi) d\xi = n_{sol}^0 z_0 + 2 \sum_{j=0}^{\infty} \int_0^z \delta(\xi - z_0 - ja) d\xi + 3 \sum_{j=0}^{\infty} \int_0^z \delta(\xi - z_0 - ja - a/2) d\xi. \quad (\text{B.4})$$



$\exp\{-5/2\text{ELA} \cdot n_0\}$ , we can rewrite the Pb/Cs and Br/Cs ratios as:

- **Pb/Cs**:

$$\frac{N_{\text{Pb}}/\sigma_{\text{Pb}}}{N_{\text{Cs}}/\sigma_{\text{Cs}}} = \frac{\alpha}{1 - \alpha^2}(1 - \alpha^2) = \alpha \quad (\text{B.8})$$

- **Br/Cs**:

$$\frac{N_{\text{Br}}/\sigma_{\text{Br}}}{N_{\text{Cs}}/\sigma_{\text{Cs}}} = \left[ \frac{1}{1 - \alpha^2} + 2\frac{\alpha}{1 - \alpha^2} \right] (1 - \alpha^2) = 1 + 2\alpha \quad (\text{B.9})$$

The interpretation of equations 8 and 9 is that when dealing with pseudocubic NCs with six (all) facets composed by CsBr terminations, the Pb/Cs and Br/Cs ratios arising from the XPS measurements are, respectively,  $\alpha$  and  $1 + 2\alpha$ , independently of the solvent attenuation inserted in the constant  $B$ . In addition, it is worth keeping in mind that the  $\alpha$  factor is dependent on the photon energy via the ELA quantity. The limits of the expressions 8 and 9 for the photon energy going to 0 and infinity can be taken making  $\alpha \rightarrow 0$  and  $\alpha \rightarrow 1$ , respectively. In the latter case, it is easy to check that the values for Pb/Cs and Br/Cs become 1 and 3, corresponding to the bulk stoichiometry. In the case of mixed facets, we could have in principle  $n_{\text{CsBr}}$  CsBr terminations and  $n_{\text{PbBr}_2}$  PbBr<sub>2</sub> terminations such that  $n_{\text{CsBr}} + n_{\text{PbBr}_2} = 6$ . Here we consider that all the facets have similar surface areas. The Pb/Cs and Br/Cs ratios with mixed facets are:

- **Pb/Cs**:

$$\frac{N_{\text{Pb}}/\sigma_{\text{Pb}}}{N_{\text{Cs}}/\sigma_{\text{Cs}}} = \frac{n_{\text{CsBr}}\alpha + n_{\text{PbBr}_2}}{n_{\text{CsBr}} + n_{\text{PbBr}_2}\alpha} \quad (\text{B.10})$$

- **Br/Cs**:

$$\frac{N_{\text{Br}}/\sigma_{\text{Br}}}{N_{\text{Cs}}/\sigma_{\text{Cs}}} = \frac{n_{\text{CsBr}}(1 + 2\alpha) + n_{\text{PbBr}_2}(2 + \alpha)}{n_{\text{CsBr}} + n_{\text{PbBr}_2}\alpha} \quad (\text{B.11})$$

where we can immediately check that they reduce to expressions 8 and 9 in the case of  $n_{\text{CsBr}} = 6$  and  $n_{\text{PbBr}_2} = 0$ .

Lastly, we discuss how the ratios are modified in the presence of the substitution/passivation on the surfaces. The primary effect of a substituent species is to attenuate the signal arising from the atom that was removed only from the term related to the outermost layers. For the CsPbBr<sub>3</sub> NCs, we consider that the candidates for substitution are the Cs and Br atoms. It is understood that they may occur, respectively, in the OLA<sup>+</sup> and AF samples. In order to adapt the expressions, we define the factor of average substitution, per atom, as  $\chi_{\text{Cs}}$  and  $\chi_{\text{Br}}$ , both real numbers between 0 and 1. One of the assumptions here is that  $\chi_{\text{Br}}$  are approximately the same for the CsBr and PbBr<sub>2</sub> terminations. The ratios are now given by:

- **Pb/Cs**:

$$\frac{N_{\text{Pb}}/\sigma_{\text{Pb}}}{N_{\text{Cs}}/\sigma_{\text{Cs}}} = \frac{n_{\text{CsBr}}\alpha + n_{\text{PbBr}_2}}{n_{\text{CsBr}}(\chi_{\text{Cs}}(1 - \alpha^2) + \alpha^2) + n_{\text{PbBr}_2}\alpha} \quad (\text{B.12})$$

- **Br/Cs**:

$$\frac{N_{\text{Br}}/\sigma_{\text{Br}}}{N_{\text{Cs}}/\sigma_{\text{Cs}}} = \frac{n_{\text{CsBr}}(\chi_{\text{Br}}(1 - \alpha^2) + \alpha^2 + 2\alpha) + n_{\text{PbBr}_2}(2\chi_{\text{Br}}(1 - \alpha^2) + 2\alpha^2 + \alpha)}{n_{\text{CsBr}}(\chi_{\text{Cs}}(1 - \alpha^2) + \alpha^2) + n_{\text{PbBr}_2}\alpha} \quad (\text{B.13})$$